

**Fluidized Nanoparticle Agglomerates  
Formation, Characterization, and Dynamics**

Fabre, Andrea

**DOI**

[10.4233/uuid:e7340a8e-1815-469c-9e46-ddea1ef17b04](https://doi.org/10.4233/uuid:e7340a8e-1815-469c-9e46-ddea1ef17b04)

**Publication date**

2016

**Document Version**

Final published version

**Citation (APA)**

Fabre, A. (2016). *Fluidized Nanoparticle Agglomerates: Formation, Characterization, and Dynamics*. [Dissertation (TU Delft), Delft University of Technology]. <https://doi.org/10.4233/uuid:e7340a8e-1815-469c-9e46-ddea1ef17b04>

**Important note**

To cite this publication, please use the final published version (if applicable).  
Please check the document version above.

**Copyright**

Other than for strictly personal use, it is not permitted to download, forward or distribute the text or part of it, without the consent of the author(s) and/or copyright holder(s), unless the work is under an open content license such as Creative Commons.

**Takedown policy**

Please contact us and provide details if you believe this document breaches copyrights.  
We will remove access to the work immediately and investigate your claim.

The background of the cover is a scanning electron micrograph (SEM) showing a dense field of dark, irregular, and porous-looking agglomerates of nanoparticles. These agglomerates vary in size and shape, some appearing as small clusters while others are larger and more complex. The overall texture is rough and granular. The text is overlaid on this image in a white, serif font.

# Fluidized Nanoparticle Agglomerates

Formation, Characterization, and Dynamics

**Andrea Fabre**



# **FLUIDIZED NANOPARTICLE AGGLOMERATES**

## **FORMATION, CHARACTERIZATION, AND DYNAMICS**

### **Proefschrift**

ter verkrijging van de graad van doctor  
aan de Technische Universiteit Delft,  
op gezag van de Rector Magnificus prof. ir. K.Ch.A.M. Luyben,  
voorzitter van het College voor Promoties,  
in het openbaar te verdedigen op

woensdag 23 november 2016  
om 12:30 uur

door

**Andrea FABRE**

Chemical and Biological Engineer  
Massachusetts Institute of Technology, de Verenigde Staten van Amerika  
geboren te Aguascalientes, Mexico

This dissertation has been approved by the promotor:

Prof. dr. ir. J. R. van Ommen

Prof. dr. ir. M. T. Kreutzer

Composition of the doctoral committee:

Rector Magnificus	chairman
Prof. dr. ir. Michiel T. Kreutzer	Technische Universiteit Delft
Prof. dr. ir. J. Ruud van Ommen	Technische Universiteit Delft

*Independent members:*

Prof. dr. Andreas Schmidt-Ott	Technische Universiteit Delft
Prof. dr. ir. Niels G. Deen	Technische Universiteit Eindhoven
Prof. dr. Frank Kleine Jäger	BASF Particle Formulation and Handling
Prof. dr. Miguel A. S. Quintanilla	University of Sevilla
Dr. Wouter K. den Otter	University of Twente
Prof. dr. ir. Chris R. Kleijn	Technische Universiteit Delft, reservelid

The research presented in this thesis received funding from the European Research Council under the European Union's Seventh Framework Programme (FP/2007-2013)/ERC Grant, agreement no. 279632, and was conducted in the Product and Process Engineering section of the Chemical Engineering department from the faculty of Applied Sciences (TNW) of the Delft University of Technology.

Copyright © 2016 by Andrea Fabre

ISBN 978-94-6186-721-6

Printed in The Netherlands by XXX

All rights reserved. Parts of this thesis are published in scientific journals and copyright is subjected to different terms and conditions.

*To my family*



# CONTENTS

<b>Summary</b>	<b>ix</b>
<b>Samenvatting</b>	<b>xi</b>
<b>1 Introduction</b>	<b>1</b>
1.1 Nanoparticles . . . . .	2
1.2 Agglomeration . . . . .	2
1.3 Fluidization . . . . .	4
1.4 Modeling . . . . .	4
1.5 Thesis Objective . . . . .	5
1.5.1 Outline. . . . .	5
References . . . . .	6
<b>2 The fractal scaling of fluidized nanoparticle agglomerates</b>	<b>11</b>
2.1 Introduction . . . . .	12
2.2 Experimental set up. . . . .	15
2.2.1 Reactor. . . . .	15
2.2.2 Powders . . . . .	16
2.2.3 Data acquisition system . . . . .	16
2.3 Results . . . . .	17
2.3.1 Fractal analysis. . . . .	17
2.4 Conclusions. . . . .	21
References . . . . .	21
<b>3 Contact mechanics of highly porous oxide nanoparticle agglomerates</b>	<b>27</b>
3.1 Introduction . . . . .	28
3.2 Experimental Section . . . . .	30
3.2.1 Powder characterization . . . . .	30
3.2.2 Sample Preparation . . . . .	30
3.2.3 Elasticity measurements . . . . .	31
3.3 Results & Discussion . . . . .	32
3.3.1 Sample characterization . . . . .	32
3.3.2 Force Curve Analysis . . . . .	33
3.3.3 Elasticity of Different Materials . . . . .	35
3.3.4 Theoretical Elasticity. . . . .	37
3.4 Conclusions. . . . .	39
References . . . . .	39



<b>4</b>	<b>Entrainment of nanosized Clusters from a nanopowder fluidized bed</b>	<b>51</b>
4.1	Introduction . . . . .	52
4.2	Experimental Section . . . . .	53
4.2.1	Powder characterization . . . . .	53
4.2.2	Experimental set up . . . . .	53
4.2.3	Microscopy analysis . . . . .	55
4.3	Results and discussion . . . . .	55
4.3.1	Powder characterization . . . . .	55
4.4	Conclusions. . . . .	61
	References . . . . .	61
<b>5</b>	<b>Characterization of the stratified morphology of nanoparticle agglomerates</b>	<b>67</b>
5.1	Introduction . . . . .	68
5.2	Methods . . . . .	69
5.2.1	Materials. . . . .	69
5.2.2	SESANS . . . . .	70
5.2.3	Settling Tube. . . . .	71
5.3	Data Analysis . . . . .	71
5.4	Results and Discussion . . . . .	74
5.4.1	SESANS . . . . .	74
5.4.2	Settling Tube. . . . .	75
5.4.3	Combining all three scales . . . . .	77
5.5	Conclusions. . . . .	79
	References . . . . .	79
<b>6</b>	<b>Modeling the size distribution in a fluidized bed of nanopowder</b>	<b>85</b>
6.1	Introduction . . . . .	86
6.2	Material and Methods. . . . .	87
6.3	Theory . . . . .	88
6.3.1	Van der Waals force . . . . .	90
6.3.2	Collision force . . . . .	91
6.3.3	Size Distribution Prediction . . . . .	92
6.4	Results and Discussion . . . . .	93
6.4.1	Size Distribution . . . . .	93
6.4.2	Model Predictions . . . . .	94
6.5	Conclusions. . . . .	95
	References . . . . .	96
<b>7</b>	<b>Conclusions and Outlook</b>	<b>103</b>
7.1	Conclusions. . . . .	103
7.2	Opportunities for future research . . . . .	104
7.2.1	Agglomerate plasticity . . . . .	104
7.2.2	Adjusted force balance model . . . . .	105
7.2.3	Collision dynamics. . . . .	106
7.2.4	Number of contacts between agglomerates . . . . .	107
7.2.5	Different production methods . . . . .	107
7.2.6	Processed nanoparticles . . . . .	108

---

References . . . . .	108
<b>Acknowledgements</b>	<b>111</b>
<b>List of Publications</b>	<b>113</b>
<b>Curriculum Vitae</b>	<b>115</b>



# SUMMARY

Nanoparticles have properties of interest in biology, physics, ecology, geology, chemistry, medicine, aerospace, food science, and engineering among many other fields, due to their intrinsic properties arising from their large surface area to volume ratio and small scale. Most nanoparticle applications require particle's surface adaptations, for which numerous methods have been developed. For this purpose, the characteristics of fluidization that make it an attractive processing technique are the large gas-solid contact area, no solvent, potential scalability, and suitability for continuous processing. Nanoparticles are not fluidized individually, but rather as clusters, which form due to the relatively large interparticle forces. As a result, fluidization dynamics is strongly linked to nanoparticle agglomeration.

Nanoparticle agglomeration is a hierarchical process, and the structures found at each level have unique properties. The first level develops during production, where in flame synthesis for example, primary nanoparticles sinter together creating chain like structures of a few hundred nanometers called aggregates. While stored, these chains connect by physical interparticle forces forming highly-porous simple agglomerates of a few microns. Finally, when fluidized, the simple agglomerates coalesce into even larger clusters called complex agglomerates, which can be hundreds of microns in size. Given that nanoparticles fluidize as complex agglomerates, these structures are the key elements in nanopowder fluidization. Hence, nanoparticle agglomeration and fluidization are the main focus of this thesis.

The work in this thesis presents a quantitative analysis of basic agglomerate properties and the techniques used to obtain them. It is known that complex agglomerates are extremely fragile structures with a solid fraction below 0.05, making them challenging to study since manipulation might introduce morphological modifications. Additionally, agglomerate properties and dynamic behavior during fluidization are hard to predict. Nonetheless, this thesis presents experimental and theoretical characterization of static and fluidized nanoparticle clusters. *In situ* techniques allowed us to study the morphology of aggregates and agglomerates during fluidization, while *ex situ* methods were employed to measure mechanical properties of the large agglomerates. To strengthen the results, simple models were used to predict the experimental data.

The morphology at each structural level was studied using two techniques to cover the whole range of relevant length scales. The two techniques are the Spin-Echo Small-Angle Neutron Scattering (SESANS) for structures smaller than  $20\ \mu\text{m}$ , and the settling tube for those between  $20\ \mu\text{m}$  and  $1\ \text{mm}$  in size. The morphology was described by the mass fractal dimension, which also provides information about the formation process. The fractal dimension obtained for aggregates, simple agglomerates, and complex agglomerates was found to differ among all three scales. Also, static and fluidized samples were compared, showing that simple agglomerates are affected by fluidization dynamics since they are extremely porous and relatively weak compared to the sintered aggregates.

As fragile, highly-porous structures, nanoparticles agglomerates are expected to be extremely susceptible to morphological changes. As an assessment of such softness, the elasticity of these structures, quantified in terms of the Young's modulus, was measured by Atomic Force Microscopy (AFM). The AFM experiments were performed on nanopowder samples prepared by spreading some material on flat sticky substrates. The sample is placed under a  $3.5\ \mu\text{m}$  glass colloid which approaches, presses, and retracts from the sample. The obtained plot of the force exerted during the pressing versus the colloid penetration distance is used to calculate the Young's modulus, found to be equivalent to that of a hard cell or soft gel, in the order of 10-200 kPa for all nanopowders tested. This property defines the size distribution inside the fluidized bed since it determines the outcome of collisions, and thus, the fluidization dynamics.

The agglomerate size distribution inside the fluidized bed was predicted by a simple force balance model, which relies on agglomerate and powder properties, and fluidization conditions. Two size values were estimated from a comparison between the adhesion and separation forces acting on a fluidized agglomerate. These values are the agglomerate size at maximum and zero force difference, corresponding to the size at the inflection point and the mode of the distribution, respectively. The model was validated with experimental data obtained from literature and our own experiments. Nonetheless, the current version of the model is limited to the complex agglomerate scale.

The full size distribution in the freeboard above the bed was measured experimentally. Structures with size in the nano to micron range were counted by a Nano-Particle Spectrometer, an Optical Particle Counter, and the settling tube techniques. The results showed a per-count dominance of nanostructures and a mass dominance of micron-size clusters. The powder was homogeneously distributed along the freeboard with consistent size distribution and powder concentration at each height. However, the overall powder concentration was decreasing significantly during the first 30 minutes of fluidization, while still keeping a stable size distribution. These findings are of great relevance for the nano-toxicity and powder-processing fields.

The above mentioned insights in nanoparticle fluidization, besides providing key information on the topic, open opportunities for future research, some of which are discussed in the Outlook section of the thesis.

# SAMENVATTING

Nanodeeltjes beschikken over interessante intrinsieke eigenschappen voor toepassingen in onder andere biologie, natuurkunde, ecologie, geologie, scheikunde, medicijnen, ruimtevaart, voedseltechnologie en techniek. De kleine deeltjesgrootte en de hoge oppervlakte-volumeverhouding zijn hiervan de belangrijkste onderliggende eigenschappen. Voor de meeste toepassingen van nanodeeltjes is modificatie van het oppervlak vereist, waarvoor verscheidene methoden zijn ontwikkeld. Fluïdisatie is in dit verband een aantrekkelijke technologie vanwege het grote contactoppervlak tussen gas en vaste stof, het niet gebruiken van oplosmiddelen, de mogelijkheid tot opschalen en de geschiktheid voor inpassing in continue processen. Nanodeeltjes fluïdiseren niet individueel maar in clusters, die gevormd worden door de grote onderlinge krachten tussen de deeltjes. Het gevolg hiervan is dat het dynamisch gedrag van fluïdisatie sterk afhangt van het agglomeratiegedrag.

Agglomeratie van nanodeeltjes is een hiërarchisch proces, en de op elk niveau gevormde structuren beschikken over unieke eigenschappen. Het eerste niveau ontwikkelt zich tijdens de productie; bijvoorbeeld bij vlamsynthese sinteren de nanodeeltjes aan elkaar tot kettingvormige structuren van enkele honderden nanometers, die aggregaten worden genoemd. Tijdens opslag ontstaan er verbindingen tussen deze aggregaten onder invloed van de onderlinge fysische krachten tussen de deeltjes, waarbij eenvoudige poreuze agglomeraten worden gevormd van enkele micrometers. Tijdens de eigenlijke fluïdisatie groeien deze agglomeraten aan elkaar tot grotere clusters, die complexe agglomeraten worden genoemd en waarvan sommige met het blote oog kunnen worden waargenomen, omdat deze tot honderden micrometers groot kunnen worden. Onderzoek naar fluïdisatie van nanopoeiers richt zich dan ook op het bestuderen van deze complexe agglomeraten. Daarom ligt de nadruk in dit proefschrift ook op agglomeratie en fluïdisatie van nanodeeltjes.

In dit proefschrift worden technieken beschreven om agglomeraten te karakteriseren, alsmede een kwantitatieve analyse van de eigenschappen van deze agglomeraten. Het is bekend dat complexe agglomeraten zeer fragiele structuren zijn met een fractie vaste stof kleiner dan 0,05. Dit maakt bestudering ervan tot een ware uitdaging, omdat elke manipulatie van deze agglomeraten tot morfologische aanpassingen zou kunnen leiden. Daarnaast zijn eigenschappen en dynamisch gedrag van agglomeraten tijdens fluïdisatie moeilijk te voorspellen. Niettemin bevat dit proefschrift experimentele en theoretische karakterisering van statische en gefluïdiseerde clusters van nanodeeltjes. *In situ* technieken geven ons de mogelijkheid de morfologie van aggregaten en agglomeraten te bestuderen tijdens de fluïdisatie, terwijl *ex situ* methodes de mogelijkheid bieden de mechanische eigenschappen van grote agglomeraten te bepalen. Om de resultaten te onderbouwen zijn eenvoudige modellen gebruikt waarmee experimentele data kunnen worden voorspeld.

De morfologie is op elk structureel niveau bestudeerd door gebruik te maken van

twee technieken waarmee het gehele gebied van relevante lengteschalen kan worden gedekt. Deze twee technieken zijn de *Spin-Echo Small Angle Neutron Scattering* (SESANS) voor structuren kleiner dan  $20\ \mu\text{m}$ , en de *settling tube* voor structuren tussen  $20\ \mu\text{m}$  en  $1\ \text{mm}$ . De morfologie wordt beschreven met behulp van de fractale dimensie op basis van massa, die tevens informatie verschaft over het vormingsproces. Er is vastgesteld dat de resulterende fractale dimensies van aggregaten, eenvoudige agglomeraten en complexe agglomeraten verschillen. Vergelijking van statische en gefluïdiseerde agglomeraten laat zien dat eenvoudige agglomeraten worden beïnvloed door fluïdisatie omdat zij extreem poreus en zwak zijn vergeleken met gesinterde aggregaten.

Het is te verwachten dat agglomeraten van nanodeeltjes, die fragiele en zeer poreuze structuren vormen, extreem gevoelig zullen zijn voor morfologische veranderingen. Ter kwantificering van deze eigenschap is de elasticiteit van de structuren gemeten, uitgedrukt als de Young's Modulus, gemeten met Atomic Force Spectroscopy (AFM). De AFM experimenten zijn uitgevoerd op monsters van nanopoeiers, bereid door het materiaal uit te strooien op een vlak, adhesief substraat. Het monster wordt onder een  $3,5\ \mu\text{m}$  glazen deeltje geplaatst, dat vervolgens naar het monster toe beweegt, het indrukt, en zich daarna weer terugtrekt. De grafiek, die verkregen werd door de uitgeoefende kracht gedurende het indrukken uit te zetten tegen de penetratiediepte, werd gebruikt om de Young's Modulus te berekenen. Dit resulteerde in waarden tussen  $10$  en  $200\ \text{kPa}$  voor alle geteste nanopoeiers, wat overeenkomt met die van een zachte gel of een harde cel. Deze eigenschap bepaalt de deeltjesgrootteverdeling in het gefluïdiseerde bed aangezien het de effecten van botsingen weergeeft en dus een maat is voor de dynamiek van de fluïdisatie. De grootteverdeling van agglomeraten in het gefluïdiseerde bed werd voorspeld door middel van een eenvoudig model op basis van een krachtenbalans, die afhangt van de eigenschappen van het agglomeraat en het poeder en de fluïdisatiecondities. Door de krachten van adhesie en separatie die inwerken op een gefluïdiseerd agglomeraat met elkaar te vergelijken konden twee waarden voor de deeltjesgrootte worden geschat. Dit zijn de grootte bij het maximale verschil in krachten en die bij geen verschil in krachten, die overeenkomen met de waarde op het buigpunt en die van de distributiemodus. Het model werd gevalideerd met experimentele data uit de literatuur en uit eigen experimenten. Echter, de huidige versie van het model is alleen geldig voor het niveau van de complexe agglomeraten.

De deeltjesgrootteverdeling in de ruimte boven het bed is experimenteel gemeten. Structuren in de orde van grootte van nanometer tot micrometer werden waargenomen en geteld met de *Nano-Particle Spectrometer*, een *Optical Particle Counter* en de *settling tube* technieken. Nanostructuren komen in de grootste aantallen voor, terwijl microstructuren het grootste deel van de massa uitmaken. Het poeder was homogeen verdeeld over de ruimte en vertoonde een consistente deeltjesgrootteverdeling en concentratie op elke hoogte. Echter, de totale poederconcentratie nam significant af gedurende de eerste  $30$  minuten van de fluïdisatie, terwijl de deeltjesgrootteverdeling stabiel bleef. Deze bevindingen zijn van groot belang voor nanotoxiciteit en poederverwerking.

Naast het verschaffen van belangrijke informatie over het onderwerp, leveren de bovengenoemde inzichten in de fluïdisatie van nanodeeltjes ook mogelijkheden voor toekomstig onderzoek, waarvan enkele besproken worden in de Outlook sectie van dit proefschrift.

# 1

## INTRODUCTION

WITH the current development of nanotechnology, nanoparticles (NPs) have acquired more attention given their potential application in a wide variety of fields which include catalysis, solar energy, consumer products, and medicine [1–4]. For many applications, single-material nanoparticles are not sufficient; thus requiring modifications to attain a certain functionality. A promising method to process these particles is fluidization, the suspension of powder in an upward gas flow, which provides a large gas-solid contact for particle surface modifications. Nanoparticles create clusters in the gas phase due to large adhesion forces, thus the structures present during fluidization are large nanoparticle agglomerates [2, 5–8]. The understanding of fluidized agglomerate formation, behavior, and morphology is crucial in order to improve the efficiency of nanopowder processing (e.g. fluidization) and applications.



## 1.1. NANOPARTICLES

Nanoparticles are defined as having at least one dimension under 100 nm (Fig.1.1). The scale of these particles provides key advantages to fields involving catalysis, biomedicine, solar energy, and electronics among many others, due to their unique characteristics such as high surface area to volume ratio, ability to enter cells, and tunable optical properties. To get an idea of their size, a chain of 1000 nanoparticles will cover the diameter of a strand of hair, a small nanoparticle (2.5 nm) has the diameter of a strand of human DNA, and 2 seconds of fingernail growth will result in a nail growth to fit a 60 nm size particle [9].

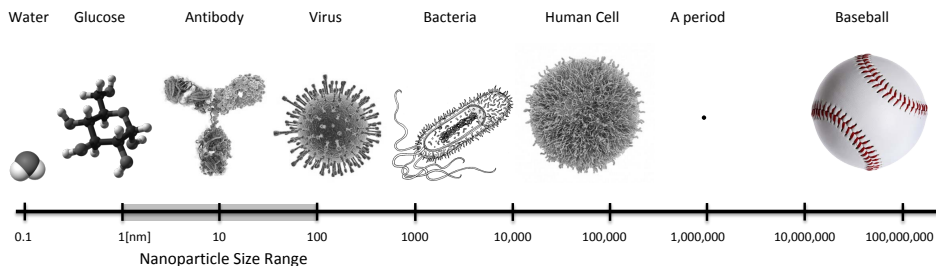


Figure 1.1: Comparison of the relative size of a nanoparticle (1-100nm).

Nanoparticles can be produced in many different ways: in liquid or gas-phase, at high or low temperatures, by combining precursors or breaking materials, etc. The production method determines the final shape (spherical, cylindrical, irregular, etc.), structure (aggregated or segregated), dispersion (mono- or polydispersed), and surface properties (hydrophobic, hydrophilic, etc.). Such features affect the interaction among nanoparticles, thus giving the production method a significant weight on nanoparticle research and applications.

A crucial feature of nanoparticles is their relatively strong attractive interactions. These particles have the intrinsic tendency to cluster when surrounded by gas, which concerns many production and processing methods. Hence, thorough understanding of the nanoparticle cluster properties in the gas-phase is necessary to optimize the use of nanopowders.

## 1.2. AGGLOMERATION

The main challenge with nanopowders in the gas-phase is their agglomeration due to strong particle interactions, which include capillary, electrostatic, solvation, and van der Waals forces [3, 10–15]. This agglomeration behavior enables the handling of large amounts of particles; however, it limits the dynamics and properties of the individual nanoparticles such as the effective surface area to volume ratio.

Nanoparticles agglomerate in a hierarchical fashion (Fig.1.2) [12]. After production, the primary particles are found linked by solid necks forming chain-like structures called aggregates, reaching no more than a few hundred nanometers in size [16]. During storage, these aggregates cluster into simple agglomerates of a few micrometers in size with

a close-to-spherical shape and high porosity. When suspended in an upward flow of gas (fluidization), simple agglomerates form complex agglomerates, which are hundreds of micrometers in size and extremely fluffy, resembling the structure of a snowflake.

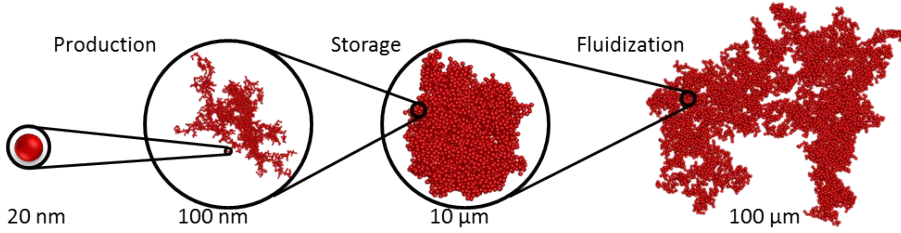


Figure 1.2: Hierarchical nanoparticle agglomeration process. From left to right are the primary particle, agglomerate, simple agglomerate, and complex agglomerate.

The morphology of the structures at each agglomeration step can be characterized by their fractal dimension [6, 11, 17–21]. This fractal dimension describes the distribution of nanoparticles as the agglomerate grows, and the mechanism of agglomerate formation. Decreasing the fractal dimension lowers the solid fraction of the agglomerate. Additionally, the agglomeration process can be particle-cluster or cluster-cluster, each of which have three subclasses with their corresponding fractal dimension [18]. One subclass is the reaction-limited, where particles with random walk have a sticking probability less than 1 in case of collision. Another subclass is the ballistic, where the mean free path of the colliding bodies is much larger than their size, and their trajectories are linear. The final subclass is the diffusion-limited, where collisions arising from random motion always lead to sticking. A value of 2.5 for the fractal dimension has been widely accepted to describe complex agglomerates, corresponding to the diffusion-limited model of the particle-cluster mechanism of formation, which describes a fractal directly formed by individual nanoparticles [3, 6, 8, 11, 14, 21–29]. However, it is known that the agglomeration process is hierarchical, thus agglomerates are formed by a cluster-cluster mechanism for which a fractal dimension of 2.5 does not apply. The expression correlating the properties of the nanoparticles to those of the large fractal structures is:

$$N_p = k_n \left( \frac{d_a}{d_p} \right)^{D_f} \quad (1.1)$$

which in terms of density becomes:

$$\rho_a = \rho_p k_n \left( \frac{d_a}{d_p} \right)^{D_f - 3} \quad (1.2)$$

where  $N_p$  is the total number of particles with size  $d_p$  and density  $\rho_p$  forming a cluster of size  $d_a$  and density  $\rho_a$ .  $k_n$  is a prefactor used to meet the limits of a single nanoparticle and an extremely large cluster, and  $D_f$  is the mass fractal dimension used to describe the cluster [30]. For multi-scale analysis of nanoparticle agglomeration, the structures at each agglomeration step should be considered independently.

Nanoparticle clusters are known to be highly-porous with void fraction above 0.95. Additionally, agglomerates are extremely fragile and dynamic during gas-phase processing. As such, *in situ* experiments to study these structures are scarce and challenging. Systems consisting of high-speed cameras or electron microscopes have been widely used in nanoparticle research. Nonetheless, methods requiring sampling or any form of powder manipulation are of questionable reliability.

### 1.3. FLUIDIZATION

Nanoparticles often require functionalization for targeted applications where characteristics of interest can be enhanced, protected, or inhibited. A method used for particle functionalization in the gas-phase is fluidization, which converts the powder behavior from solid-like to fluid-like. Fluidization is promising for nanoparticle processing due to excellent gas-solid contact area, lack of solvent, and potential scalability [4, 7, 12, 31–33]. Powder fluidizability has been categorized by Geldart, based on particle size and particle-fluid density difference [34]. Even though nanopowders belong to Geldart's group C (see Fig.1.3), characterized as almost impossible to fluidize, they fluidize as highly-porous agglomerates mainly located outside Geldart's original diagram.

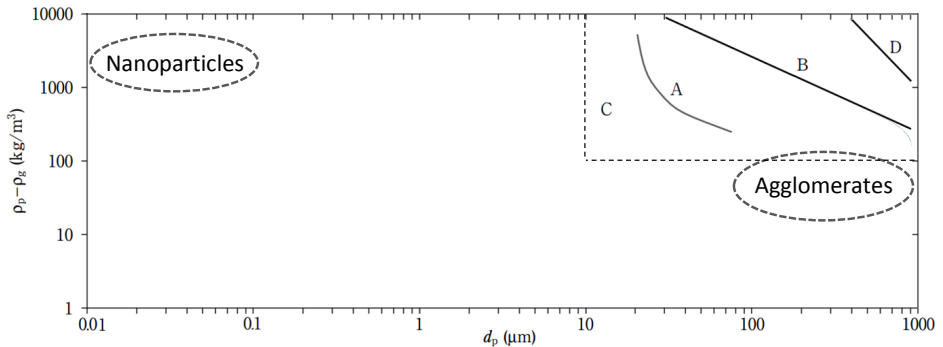


Figure 1.3: Geldart's classification of powders according to their fluidizability based on particle size and particle-gas density difference. The dotted line shows the limit of the original Geldart's diagram.

Nanopowders show two types of fluidization behavior, homogeneous or with bubbles. The uniform fluidization characterized by large bed expansion and homogeneous distribution of the powder is called agglomerate particulate fluidization (APF). On the other hand, the agglomerate bubbling fluidization (ABF) has dynamics influenced by bubble-bursting. The contrasting fluidization behaviors affect the formation, properties, and dynamics of the complex agglomerates inside the bed. Thus, nanopowders belonging to different groups should be evaluated independently.

### 1.4. MODELING

Since nanoparticle processing can be troublesome due to agglomeration and unknown hazards arising from such small size, modeling is particularly valuable. Multiple models

have been developed to predict the average agglomerate size inside the fluidized bed. These models are often based on the Richardson-Zaki equation relying on the superficial gas velocity, bed voidage, single agglomerate terminal velocity and Stoke's law; or on a force or energy balance of the fluidized agglomerate. These models are designed to estimate only the average size, leaving the details on the whole size distribution unknown [19, 35–40]. Furthermore, the experimental validation of the models has not been trivial.

Many assumptions have to be made in order to estimate complex or unknown properties of the primary particles and nanoparticles clusters. In this work, model development is simplified by skipping the disputed fractal morphology of the cluster, assuming the agglomerates to be highly-porous spheres with an homogeneous distribution of nanoparticles. For the study of specific properties, the agglomerate surface is taken as perfectly smooth, dry, and susceptible to deformation, assumed to be elastic. It has to be noted that the increased ease outweighs the induced error of these assumptions.

## 1.5. THESIS OBJECTIVE

The work presented in this thesis is one piece of a larger project focused on elucidating the physics of nanoparticle agglomeration and fluidization, simulation of fluidization dynamics, and efficient nanoparticle coating by Atomic Layer Deposition (ALD).

The topic of this thesis is the formation mechanism, structural characterization, and fluidization dynamics of nanoparticle agglomerates. The main objective is to understand the effect of fluidization on the agglomerate's morphology and the properties of the different structures formed during the step-wise agglomeration process. Some essential questions on nanoparticle fluidization concerning this work are:

- What are the properties of the fluidized complex agglomerates?
- What is the size of the structures present in a fluidized bed of nanopowders?
- Can the size distribution inside the bed be predicted via a simple analytical model?
- To what extent does fluidization affect the hierarchy of the agglomeration process?

These questions are addressed in the coming chapters, providing insight on nanoparticle agglomerate properties and dynamics during fluidization, and potential opportunities for future research.

### 1.5.1. OUTLINE

This thesis contains seven chapters. This first chapter is the introduction to the topics of this work, and the seventh (last), the conclusion of the discussed research and opportunities for future studies as continuation of this work. The five chapters constituting the main body of the thesis are explained below.

In Chapter two, the fractal dimension of fluidized complex agglomerates is analyzed experimentally using an *in situ* technique to verify the expected cluster-cluster mechanism. The results differ from the widely accepted 2.5 as the fractal dimension of the fluidized complex agglomerates. This value suggests that the agglomerates are formed by a particle-cluster mechanism, which does not agree with the known hierarchical nature of the process.

Given that collisions are a main component in fluidization dynamics, the elastic property of the colliding complex agglomerates is crucial information. Chapter three provides the Young's modulus of three ceramic oxide nanoparticle agglomerates measured by Atomic Force Microscopy (AFM). The sample preparation, measuring, and data analysis methods for elasticity measurements of highly-porous fragile structures are explained.

Nanoparticles are assumed to always agglomerate in the gas-phase, and thus significantly decreasing their toxicity. Nonetheless, fluidization dynamics can break agglomerates, creating nanofragments of which the presence, concentration, and behavior were unknown. Chapter four presents experimental measurements of the size distribution above the fluidized bed, covering the whole nano to micron size range. Despite the intrinsic property of nanoparticles to form agglomerates in the gas-phase, the detection of nanostructures brings concerns on health risks in case of exposure.

Nanoparticles agglomerate in a step-wise fashion forming weak highly-porous clusters, which are constantly breaking-up, coalescing, and rearranging during fluidization. The morphological properties of the structures at each agglomeration step are expected to be different, as well as their sensitivity to external factors such as those arising from fluidization. Chapter five describes the morphological distinctions among all three structural levels of agglomeration, and the effect of fluidization on them.

The average agglomerate size inside the fluidized bed has been predicted several times using the force balance approach, without any description of the size distribution. As a straightforward method, a force balance model is developed in chapter six to predict the size distribution of fluidized nanoparticle agglomerates. The model is validated with experimental data, and found to be in good agreement.

## REFERENCES

- [1] M. Heggen, M. Oezaslan, L. Houben, and P. Strasser, *Formation and analysis of core-shell fine structures in Pt bimetallic nanoparticle fuel cell electrocatalysts*, The Journal of Physical Chemistry C **116**, 19073 (2012).
- [2] J. R. van Ommen, *Manufacturing core-shell nanoparticles by atomic layer deposition in a fluidized bed*, in *International Symposium on Chemical Reaction Engineering* (2012).
- [3] J. M. Valverde, M. A. S. Quintanilla, A. Castellanos, D. Lepek, J. Quevedo, R. N. Dave, and R. Pfeffer, *Fluidization of fine and ultrafine particles using nitrogen and neon as fluidizing gases*, AIChE Journal **54**, 86 (2008).
- [4] C. Zhu, Q. Yu, R. N. Dave, and R. Pfeffer, *Gas fluidization characteristics of nanoparticle agglomerates*, AIChE Journal **51**, 426 (2005).
- [5] J. Israelachvili, *Intermolecular and surface forces* (Academic Press, 1991).
- [6] J. Shabanian, R. Jafari, and J. Chaouki, *Fluidization of ultrafine powders*, Int Rev Chem Eng **4**, 16 (2012).

- [7] L. F. Hakim, J. L. Portman, M. D. Casper, and A. W. Weimer, *Aggregation behavior of nanoparticles in fluidized beds*, Powder Technology **160**, 149 (2005).
- [8] M. J. Espin, J. M. Valverde, M. A. S. Quintanilla, and A. Castellanos, *Electromechanics of fluidized beds of nanoparticles*, Physical Review E **79** (2009).
- [9] S. Yaemsiri, N. Hou, M. Slining, and K. He, *Growth rate of human fingernails and toenails in healthy american young adults*, Journal of the European Academy of Dermatology and Venereology **24**, 420 (2010).
- [10] A. Rao, J. S. Curtis, B. C. Hancock, and C. Wassgren, *The effect of column diameter and bed height on minimum fluidization velocity*, AIChE Journal **56**, 2304 (2010).
- [11] C. H. Nam, R. Pfeffer, R. N. Dave, and S. Sundaresan, *Aerated vibrofluidization of silica nanoparticles*, AIChE Journal **50**, 1776 (2004).
- [12] W. Yao, G. Guangsheng, W. Fei, and W. Jun, *Fluidization and agglomerate structure of SiO<sub>2</sub> nanoparticles*, Powder Technology **124**, 152 (2002).
- [13] S. Salameh, J. Schneider, and J. Laube, *Adhesion mechanisms of the contact interface of TiO<sub>2</sub> nanoparticles in films and aggregates*, Langmuir **28**, 11457 (2012).
- [14] J. R. van Ommen, J. M. Valverde, and R. Pfeffer, *Fluidization of nanopowders: a review*, Journal of Nanoparticle Research **14**, 737 (2012).
- [15] S. Salameh, R. Scholz, J. W. Seo, and L. Madler, *Contact behavior of size fractionated TiO<sub>2</sub> nanoparticle agglomerates and aggregates*, Powder Technology **256**, 345 (2014).
- [16] M. Seipenbusch, S. Rothenbacher, M. Kirchhoff, H. J. Schmid, G. Kasper, and A. P. Weber, *Interparticle forces in silica nanoparticle agglomerates*, Journal of Nanoparticle Research **12**, 2037 (2010).
- [17] T. Vicsek, *Fractal Growth Phenomena*, edited by T. Vicsek (World Scientific Pub Co Inc, 1992).
- [18] S. K. Friedlander, *Smoke, Dust, and Haze: Fundamentals of Aerosol Dynamics* (Oxford University Press, 2000).
- [19] L. de Martin, W. G. Bouwman, and J. R. van Ommen, *Multidimensional nature of fluidized nanoparticle agglomerates*, Langmuir **30**, 12696 (2014).
- [20] D. Hu, J. Zhuang, and M. Ding, *A review of studies on the granular agglomeration mechanisms and anti-agglomeration methods*, Key Engineering Materials **501**, 515 (2012).
- [21] J. M. Valverde and A. Castellanos, *Fluidization, bubbling and jamming of nanoparticle agglomerates*, Chemical Engineering Science **62**, 6947 (2007).
- [22] J. Quevedo, R. Pfeffer, Y. Shen, R. Dave, H. Nakamura, and S. Watano, *Fluidization of nanoagglomerates in a rotating fluidized bed*, AIChE J **52**, 2401 (2006).

- [23] J. M. Valverde and A. Castellanos, *Fluidization of nanoparticles: A modified Richardson-Zaki Law*, *AIChE J* **52**, 838 (2006).
- [24] X. S. Wang, V. Palero, J. Soria, and M. J. Rhodes, *Laser-based planar imaging of nano-particle fluidization: Part ii - mechanistic analysis of nanoparticle aggregation*, *Chemical Engineering Science* **61**, 8040 (2006).
- [25] J. M. Valverde, M. A. S. Quintanilla, M. J. Espin, and A. Castellanos, *Nanofluidization electrostatics*, *Physical Review E* **77**, 031301 (2008).
- [26] H. Nakamura and S. Watano, *Fundamental particle fluidization behavior and handling of nano-particles in a rotating fluidized bed*, *Powder Technol* **183**, 324 (2008).
- [27] M. A. S. Quintanilla, J. M. Valverde, A. Castellanos, D. Lepek, R. Pfeffer, and R. N. Dave, *Nanofluidization as affected by vibration and electrostatic fields*, *Chem Eng Sci* **63**, 5559 (2008).
- [28] D. To, R. Dave, X. Yin, and S. Sundaresan, *Deagglomeration of nanoparticle aggregates via rapid expansion of supercritical or high-pressure suspensions*, *AIChE J* **55**, 2807 (2009).
- [29] P. Ammendola, R. Chirone, and F. Raganati, *Fluidization of binary mixtures of nanoparticles under the effect of acoustic fields*, *Mater Sci Forum* **22**, 174 (2011).
- [30] L. de Martin, A. Fabre, and J. R. van Ommen, *The fractal scaling of fluidized nanoparticle agglomerates*, *Chemical Engineering Science* **112**, 79 (2014).
- [31] J. Jung and D. Gidaspow, *Fluidization of nano-size particles*, *Journal of Nanoparticle Research* **4**, 483 (2002).
- [32] M. Dadkhah, M. Peglow, and E. Tsotsas, *Characterization of the internal morphology of agglomerates produced in a spray fluidized bed by x-ray tomography*, *Powder Technology* **228**, 349 (2012).
- [33] J. A. Quevedo, A. Omosebi, and R. Pfeffer, *Fluidization enhancement of agglomerates of metal oxide nanopowders by microjets*, *AIChE Journal* **56**, 1456 (2010).
- [34] D. Geldart, *Types of gas fluidization*, *Powder Technology* **7**, 285 (1973).
- [35] M. H. Yuki Iwadate, *Prediction of agglomerate sizes in bubbling fluidized beds of group c powders*, *Powder Technology* **100**, 223 (1998).
- [36] T. Zhou and H. Z. Li, *Force balance modelling for agglomerating fluidization of cohesive particles*, *Powder Technology* **111**, 60 (2000).
- [37] D. Turki and N. Fatah, *Behavior and fluidization of the cohesive powders: Agglomerates sizes approach*, *Brazilian Journal of Chemical Engineering* **25**, 697 (2008).
- [38] H. L. Tao Zhou, *Estimation of agglomerate size for cohesive particles during fluidization*, *Powder Technology* **101**, 57 (1999).

- 
- [39] S. Matsuda, H. Hatano, T. Muramoto, and A. Tsutsumi, *Modeling for size reduction of agglomerates in nanoparticle fluidization*, *Aiche Journal* **50**, 2763 (2004).
- [40] J. Chaouki, C. Chavarie, and D. Klvana, *Effect of interparticle forces on the hydrodynamic behavior of fluidized aerogels*, *Powder Technology* **43**, 117 (1985).





# 2

## THE FRACTAL SCALING OF FLUIDIZED NANOPARTICLE AGGLOMERATES

It is widely reported in literature that fluidized nanoparticle agglomerates have a mass fractal dimension about 2.5, representing a dominant particle–cluster diffusion limited agglomeration (DLA) mechanism. In this paper, we show that a fractal dimension 2.5 –which is calculated assuming a prefactor one in the fractal scaling law– approximates the density of the agglomerates in a limited range of sizes but does not describe the scaling of the agglomerate density (or agglomerate mass) with the agglomerate size, which is the ultimate meaning of a mass fractal dimension. By studying the settling of fluidized agglomerates, we have found that the mass fractal dimension describing the power-law scaling of the agglomerate mass with the size for complex agglomerates is about 2, whereas the prefactor can be up to two orders of magnitude larger than one. The fractal dimension can be explained considering that simple agglomerates link to form complex agglomerates with cluster–cluster ballistic aggregation. The large prefactor represents the multidimensional nature of nanoparticle agglomerates. These results replace the general idea of a dominant particle–cluster DLA mechanism in the fluidized bed.

---

Published as: L. de Martin, A. Fabre, and J. R. van Ommen. The fractal scaling of fluidized nanoparticle agglomerates. *Chemical Engineering Science*, 112:79 – 86, 2014 [1].

## 2.1. INTRODUCTION

Fluidization is an attractive method to process nanoparticles, for instance, to produce coated nanoparticles [2, 3]. Nanoparticles, peculiarly, do not fluidize individually but forming agglomerates as a result of van der Waals forces [4, 5], capillary bridges [6] or hydrogen bond formation [7]. Although nanoparticle fluidization has been extensively studied in the last decade, the interplay between nanoparticle and agglomerate properties, and fluidization dynamics is still not fully resolved. A reason is the lack of knowledge about the agglomerate structure.

The agglomerate structure is commonly described by means of fractal geometry [4, 5, 8, 9]. In a mass fractal cluster formed by monodisperse particles of size  $d_p$ , the number of particles  $N_p$  or agglomerate density  $\rho_a$  scales to the power of the ratio  $d_a/d_p$  according to

$$N_p = k_n \left( \frac{d_a}{d_p} \right)^{D_f} \quad \text{or} \quad \rho_a = \rho_p k_n \left( \frac{d_a}{d_p} \right)^{D_f-3} \quad (2.1)$$

where  $d_a$  is the agglomerate diameter,  $\rho_p$  is the particle density,  $k_n$  is a prefactor and  $D_f$  is the mass fractal dimension, from now on denoted as "fractal dimension".

The popularity of the fractal dimension arises from the large amount of information deduced from it. It describes the agglomerate structure, necessary to model diffusion processes inside the agglomerates and agglomerate breakage, and it also gives information about the growth mechanism of the agglomerates [8, 9]. The cluster-cluster diffusion limited aggregation (DLA) mechanism forms open clusters with fractal dimension  $D_f = 1.80$ , whereas  $D_f = 2.50$  would indicate dominant particle-cluster diffusion limited aggregation. A fractal dimension 3.0 is found in clusters formed by a particle-cluster ballistic aggregation and reaction limited aggregation with low sticking coefficient (Fig. 2.1).


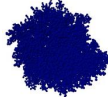

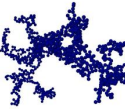

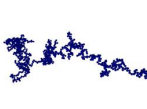
	Reaction-limited	Ballistic	Diffusion-limited
Particle-cluster	 $D_f=3.00$	 $D_f=3.00$	 $D_f=2.50$
Cluster-cluster	 $D_f=2.09$	 $D_f=1.95$	 $D_f=1.80$

Figure 2.1: Kinetic growth models in a 3D embedding space and fractal dimensions associated (based on [9]).

It is extensively reported in literature that fluidized nanoparticle agglomerates have a fractal dimension about 2.5, suggesting a dominant particle-cluster DLA mechanism in the bed [4, 5, 10–21]. This seems counter-intuitive because in the particle-cluster DLA mechanism individual particles link to existing clusters, therefore requiring a medium containing free moving nanoparticles. This contradicts the well known fact that nanoparticles fluidize as agglomerates, not individually [4, 5]. Moreover, nanoparticles produced

in flame reactors –such as commercial nanoparticles typically used in fluidization studies– already form sintered aggregates with cluster–cluster mechanism during their synthesis [22, 23]. Thus, to claim that large fluidized nanoparticle agglomerates are formed by a particle–cluster mechanism is, at least, questionable. If there is a dominant mechanism in the formation of large fluidized agglomerates, it seems more logical to expect a cluster–cluster mechanism.

Papers claiming a fractal dimension about 2.5 assume that the number of particles in the agglomerate,  $N_p$ , relates to the ratio  $d_a/d_p$  like in Eq. (5.1), with  $k_n = 1$ . Papers that use image analysis to estimate  $D_f$  analyze fluidized nanoparticle agglomerates larger than  $\sim 100 \mu\text{m}$  [10, 24, 25]. In bed expansion studies [12, 18, 19], the expansion is determined from the average properties of the agglomerates, such as average density and average agglomerate size. Thus, the fractal dimension and prefactor used to characterize the expansion are those values that predict the average agglomerate density, associated to the average agglomerate size  $\sim 100\text{--}300 \mu\text{m}$  [16, 26]. So far, no one has studied the scaling of the number of nanoparticles in a fluidized agglomerate with the agglomerate size. In all cases,  $D_f$  is calculated from the agglomerate density and  $d_a$  in the interval  $\sim 100 - 300 \mu\text{m}$  and applying Eq. (5.1) with  $k_n = 1$ , without further discussion. The exponent 2.5 obtained in this way, is the value that explains the observed agglomerate density or bed expansion for  $k_n = 1$ . The question is, if the value 2.5 also explains the power–law scaling of the agglomerate density with the agglomerate size, which is the ultimate meaning of a fractal dimension [27].

Let us discuss the assumption  $k_n = 1$  in detail. According to Sorensen *et al.* [28], the prefactor of fractal clusters has a value so that Eq. (5.1) has the correct  $N_p = 3$  limit, and that limit is a linear arrangement of three monomers. According to Jiang and Logan [29], for an Euclidean object,  $k_n$  is a function of the packing factor and the ratio of the shape factors of the aggregate and the primary particles. The prefactor of the agglomerates generated by the six mechanisms displayed in Fig. 2.2 is well known. Although the prefactor can be affected by the overlap of particles due to sintering [30] or polydispersity [31], most of real agglomerates have a prefactor between 0.5 and 3 [28, 32]. Ehrl *et al.* [33] studied the geometry of simulated clusters formed by rigid monodisperse primary particles with a fractal dimension in the range from 2.2 to 3. They propose a correlation for the prefactor with the form  $k_n = 4.46D_f^{-2.08}$ , which gives a prefactor  $k_n \sim 1$  for  $D_f = 2.0$  when using particle radius and agglomerate gyration radius in Eq. (5.1).

Therefore, without further information, the assumption  $k_n = 1$  seems a reasonable starting point. However, all previous studies report prefactors for mono-dimensional clusters; that is, clusters in which the building unit is the particle and all the scales are described by a unique fractal dimension. This might be the case of agglomerates formed by micron–sized particles, but does not hold for nanoparticle agglomerates. Yao *et al.* [34] were the pioneers in describing fluidized nanoparticle agglomerates as three level hierarchical structures, a picture broadly accepted in literature [4, 10, 35]. According to these authors, nanoparticles first form strong aggregates –probably during the flame synthesis of the nanoparticles– with a very open structure and a size of a few hundreds nm. Later, these aggregates link to form simple agglomerates with an average size of a few dozens of microns. In a fluidized bed, simple agglomerates combine to form larger complex agglomerates. A remaining question was whether the fractal dimension is dif-

ferent for each hierarchical level, as already suspected [16]. So far, this question has been unanswered due to the lack of proper *in-situ* analysis techniques. However, in a recent work by de Martín *et al.* [36] using *in-situ* neutron scattering, two different fractal dimensions were found in the range 20 nm – 20  $\mu\text{m}$ , corresponding to aggregates and simple agglomerates. The technique cannot reach the large scales of complex agglomerates, however, based on the work of Yao *et al.* [34], we expect a third fractal dimension representing the agglomeration mechanism of simple agglomerates in the fluidized bed.

If complex agglomerates have three fractal dimensions, Eq. (5.1) needs to be re-interpreted to understand what kind of information is deduced from the relation between agglomerate density and size. In a mono-dimensional agglomerate, the building block is the particle. In a three level fractal formed sequentially, the building block of the tertiary fractal (complex agglomerates) is the secondary fractal. The secondary fractals (simple agglomerates) are built by primary fractals (aggregates), which in turn are built by particles. Let us illustrate this with an example. A tertiary cluster of size  $d_3$  is built by  $N_{3,2}$  blocks of size  $d_2$  which link with a mechanism characterized by a fractal dimension  $D_{f,3}$  and a prefactor  $k_3$ . A secondary fractal of size  $d_2$  is built by  $N_{2,1}$  blocks of size  $d_1$  which link with a mechanism characterized by a fractal dimension  $D_{f,2}$  and a prefactor  $k_2$  and so on (Eq. 5.2).

$$\begin{aligned} N_{1,p} &= k_1 \left( \frac{d_1}{d_p} \right)^{D_{f,1}} \\ N_{2,1} &= k_2 \left( \frac{d_2}{d_1} \right)^{D_{f,2}} \\ N_{3,2} &= k_3 \left( \frac{d_3}{d_2} \right)^{D_{f,3}} \end{aligned} \quad (2.2)$$

Assuming that all the building blocks are monodisperse and all the blocks of the level  $i$  belong to the level  $i - 1$ , the total number of particles in the tertiary fractal (complex agglomerate) is  $N_p = N_{3,2}N_{2,1}N_{1,p}$ , which combined with Eq. (5.2) gives

$$N_p = \hat{k}_n \left( \frac{d_3}{d_p} \right)^{D_{f,3}} \quad (2.3)$$

where

$$\hat{k}_n = k_1 k_2 k_3 d_p^{D_{f,3}-D_{f,1}} d_1^{D_{f,1}-D_{f,2}} d_2^{D_{f,2}-D_{f,3}}. \quad (2.4)$$

So the prefactor  $\hat{k}_n$ , which relates the number of particles in a complex agglomerate  $N_p$  to the ratio  $(d_3/d_p)^{D_{f,3}}$ , so often considered one, is actually a function of the size of the aggregates and primary agglomerates, and the fractal dimensions  $D_{f,1}$ ,  $D_{f,2}$  and  $D_{f,3}$ . For a mono-dimensional fractal,  $D_{f,1} = D_{f,2} = D_{f,3}$ , and indeed  $\hat{k}_n \sim 1$  assuming  $k_i \sim 1$ . Nonetheless, for multidimensional nanoparticle agglomerates,  $\hat{k}_n$  can be up to two orders of magnitude larger than one, as we will show.

To circumvent the need of guessing a prefactor,  $D_{f,3}$  can be obtained from the slope  $\log(N_p)$  vs.  $\log(d_a/d_p)$  in the range of sizes corresponding to complex agglomerates. Although simple in concept, this method is quite challenging because in order to have a

good estimation of the fractal dimension, the power-law scaling (Eq. 5.1) must be observed in at least one decade of scales [37].

The goal of this work is therefore to estimate the mass fractal dimension of fluidized and complex nanoparticle agglomerates. That is, the exponent of Eq. (5.1) that describes the power-law scaling of the agglomerate mass with the agglomerate size in the range of sizes corresponding to the complex agglomerates, 40–400  $\mu\text{m}$ . Opposite to previous studies, we calculate the fractal dimension from the slope  $\log(N_p)$  vs.  $\log(d_a/d_p)$ , instead of from Eq. (5.1) assuming  $k_n = 1$ .

## 2.2. EXPERIMENTAL SET UP

### 2.2.1. REACTOR

The experiments were carried out in a  $4.5 \times 4.5$  cm square cross-section column made of PMMA (Fig. 2.2a). Nanopowders were fluidized with pure nitrogen at a superficial velocity  $u_0 = 13.0$  cm/s, supplied to the bed through a porous plate gas distributor. The nitrogen leaving the system passes through a water bubbler and a HEPA filter to remove the entrained powder.

A black tube made of polyoxymethylene is placed in the middle of the bed to collect fluidized agglomerates and visualize their settling with a borescope (Fig. 2.2b). The tube has a rectangular inlet of  $1 \times 4$  mm, an internal cross-section of  $4 \times 8$  mm and a height of 33 mm. The thin inlet placed in the middle of the cross-section makes the agglomerates fall at a similar distance from the borescope, minimizing errors in the agglomerate size due to different amplification. The large cross-section of the tube ensures that the settling of agglomerates smaller than  $\sim 400$   $\mu\text{m}$  is not affected by the walls [38]. The tube has a secondary gas inlet to empty it before recording the falling agglomerates. During the agglomerate settling, there is no gas circulating through the tube. Details about this technique can be found elsewhere [39].

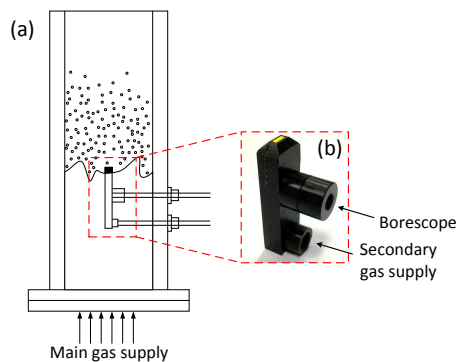


Figure 2.2: Sketch of the experimental set-up. (a) Fluidized bed with a settling tube to collect agglomerates, (b) Detail of the settling tube. The inlet has been highlighted for a better visualization.

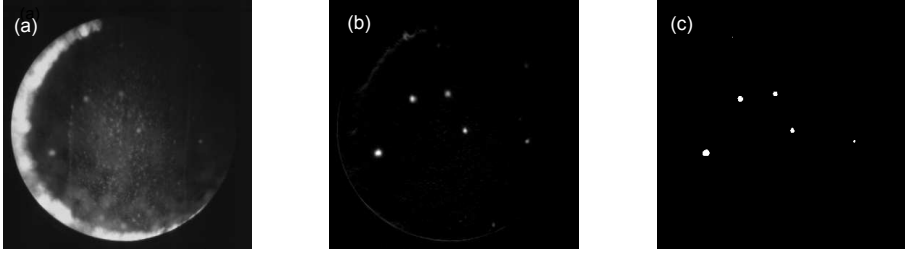


Figure 2.3: Example of image treatment. (a) Original , (b) processed and (c) thresholded.

### 2.2.2. POWDERS

Three commercial nanopowders manufactured by Evonik were fluidized (Table 6.1).  $\text{TiO}_2$  T805 is the hydrophobic version of  $\text{TiO}_2$  P25, where the hydroxyl groups on the surface of P25 have been substituted by trimethoxy octyl silane groups  $\text{CH}_3(\text{CH}_2)_7\text{Si}(\text{OCH}_3)_3$  [7, 40].

The bed height at the beginning of the experiments was 3 cm for  $\text{TiO}_2$  T805 and  $\text{TiO}_2$  P25, and 2 cm for  $\text{Al}_2\text{O}_3$ . Experiments have been repeated three times for each powder to ensure the reproducibility of the results.

Table 2.1: Properties of the fluidized nanopowders. The particle density and size are provided by the manufacturer.

Powder	Surface	$\rho_p$ ( $\text{kg}/\text{m}^3$ )	$d_p$ (nm)
$\text{TiO}_2$ T805	hydrophobic	4000	21
$\text{TiO}_2$ P25	hydrophilic	4000	21
$\text{Al}_2\text{O}_3$ Alu C	hydrophilic	3800	13

### 2.2.3. DATA ACQUISITION SYSTEM

A Phantom Vision Research Phantom v9.1 high-speed camera was attached to an Olympus R040-021-000-60 S5 industrial rigid borescope to record the settling agglomerates. The borescope tip has a diameter of 4 mm and its own light source to illuminate the tube from inside. The distance between the borescope tip and the settling plane is the same for all the experiments and equal to 4 mm. The amplification at this distance corresponds to a pixel size of  $\sim 17 \mu\text{m}$ , obtained by calibration of the borescope.

The accuracy of the length is 0.5 pixel, which leads to a maximum error of  $\sim 28\%$  for  $30 \mu\text{m}$  agglomerates. Errors due to pixel locking are not taken into account [41].

All movies have been recorded at 800 fps during 20 seconds and processed identically. An example is shown in Fig. 2.3. The agglomerates have been tracked with the algorithm detailed in [39].

## 2.3. RESULTS

### 2.3.1. FRACTAL ANALYSIS

From the movies recorded in the settling tube, we obtain the terminal velocity  $U_t$  and the projected area  $A_a$  of the agglomerates. The agglomerate density  $\rho_a$  is estimated from the terminal velocity using Eq. (6.5),

$$U_t^2 = \frac{V_a}{A_a C_D} \frac{2(\rho_a - \rho_f)g}{\rho_f} \quad (2.5)$$

where  $V_a$  and  $d_h$  are the volume and equivalent diameter of the agglomerates ( $d_h = \sqrt{4A_a/\pi}$ ) [32],  $\rho_f$  is the gas density and  $C_D$  is the drag coefficient, which is a function of the Reynolds, sphericity and permeability of the agglomerates. We assume that the agglomerates are impermeable, this assumption is justified in the Appendix. For rigid and impermeable particles, Haider and Levenspiel [42] proposed the following correlation, valid for  $\text{Re} < 2.6 \cdot 10^5$ .

$$C_D = \frac{24}{\text{Re}}(1 + A\text{Re}^B) + \frac{C}{\left(1 + \frac{D}{\text{Re}}\right)} \quad (2.6)$$

where  $A$ ,  $B$ ,  $C$  and  $D$  are function of the agglomerate sphericity  $\phi$ .

The sphericity ( $\phi$ ) of the agglomerates can be approximated from their circularity ( $\Theta$ ) if the averaged agglomerates show all possible structures and orientations [24, 43]. There are multiple ways to define the circularity of a 2D silhouette (for a review see [43]). In this work, we use the definition given by Riley [44], where the circularity is the square root of the ratio of the diameter of the largest inscribed circle ( $d_i$ ) to the diameter of the smallest circumscribing circle ( $d_c$ ),  $\Theta = \sqrt{\frac{d_i}{d_c}}$ . This definition has been widely used in sedimentological studies and is recommended in [43].

The histogram of the agglomerate circularity is illustrated in Fig. 2.4, showing that most agglomerates have a circularity between 0.8 and 0.95. The sphericity is assumed to be in the similar range given the high number of tracked agglomerates. It will be shown in the results that the impact of the sphericity on the estimated fractal dimension  $D_f$  and prefactor  $k$  for the agglomerates in this range of sphericities is negligible as compared to the uncertainties of  $D_f$  and  $k$ . For this reason, we will choose an sphericity equal to 0.87 for all the agglomerates.

The estimation of the fractal dimension of a cluster from its 2D projection involves some assumptions. One method consists on relating the area and perimeter of the projected cluster to its 3D properties, such as the gyration radius [33]. However, this method requires images with well resolved clusters to get reasonable results; a resolution commonly obtained with microscopy. Unfortunately, this resolution is impossible to get with current commercial borescopes, for which a pixel represents several microns. Brasil *et al.* [30] and Bushell *et al.* [32] have described methods to estimate the fractal dimension of clusters from their 2D silhouette based on agglomerate length, instead of perimeter. These methods are less affected by the image resolution and have been used throughout this work.

To estimate the fractal dimension and prefactor, the agglomerate mass –or number of particles in an agglomerate– must be represented as a function of some characteristic



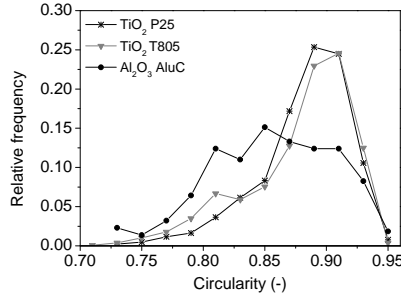


Figure 2.4: Relative frequency of agglomerate circularity. 1286 agglomerates sampled for TiO<sub>2</sub> P25, 1576 agglomerates sampled TiO<sub>2</sub> T805, 218 agglomerates sampled for Al<sub>2</sub>O<sub>3</sub> AluC.

agglomerate length, such as gyration, maximum or hydrodynamic diameter. Different lengths will give different prefactors, whereas the fractal dimension is not affected as long as the agglomerate mass scales the same way with the different lengths [30, 32].

When the agglomerate structure is analyzed with scattering techniques, the characteristic length of Eq. (5.1) is the gyration diameter. To allow a comparison between techniques, we will choose  $d_{\text{gyr}}$  as the characteristic length. As discussed in [30, 32], it is accepted that the maximum projected diameter  $d_c$  and the gyration diameter  $d_{\text{gyr}}$  of an agglomerate are directly proportional, especially in the Stoke's regime [32]. Brasil *et al.* [30] propose that

$$\frac{d_c}{d_{\text{gyr}}} = 1.5 \pm 0.05 \quad (2.7)$$

A more elaborated correlation is given by [32], giving a comparable result.

$$\frac{d_c}{d_{\text{gyr}}} = \left( \frac{D_f + 2}{D_f} \right)^{0.5} \quad (2.8)$$

Once  $\rho_a$  is obtained from Eq. (6.5), and  $d_{\text{gyr}}$  is obtained from Eq. (2.7), the number of particles per agglomerate  $N_p$  as a function of  $d_{\text{gyr}}/d_p$  can be represented, where

$$N_p = \frac{\rho_a}{\rho_p} \left( \frac{d_{\text{gyr}}}{d_p} \right)^3. \quad (2.9)$$

The plots  $\log(N_p)$  vs.  $\log(d_{\text{gyr}}/d_p)$  for all runs are shown in the Supplementary Material. An example is illustrated in Fig. 2.5 for TiO<sub>2</sub> P25. It is worth noticing that the difference between equivalent and gyration diameters is less than 20 %, so Fig. 2.5 would look nearly the same if using equivalent diameters. Yet, we prefer to use gyration diameter to be consistent with our analysis method.

The logarithm of the density and number of particles shows a linear relationship with the logarithm of the agglomerate gyration diameter in the range 40–400  $\mu\text{m}$ , confirming the fractal structure in this interval. The prefactors  $\hat{k}_n$  and fractal dimensions  $D_{f,3}$  calculated from the fittings  $\log(N_p)$  vs.  $\log(d_{\text{gyr}}/d_p)$  are shown in Table 6.2. For a detailed description of the regression analysis and error estimation see Supplementary Material.

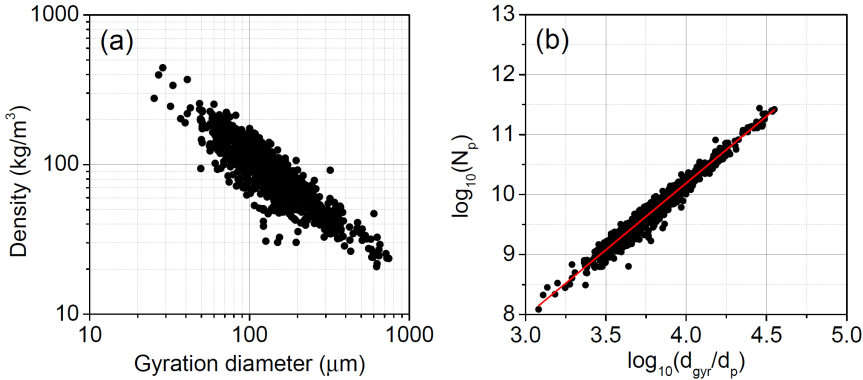


Figure 2.5: Results for TiO<sub>2</sub> P25 nanoparticle agglomerates. Variation of (a) agglomerate density and (b) number of particles as a function of gyration diameter. Red line represents the best fitting. For more information see Supplementary Material.

Table 2.2: Prefactor and fractal dimension of complex nanoparticle agglomerates. Confidence intervals are  $2\sigma$ .

Powder	$\hat{k}_n$ (-)	$D_{f,3}$ (-)
TiO <sub>2</sub> T805	$74 \pm 9$	$2.07 \pm 0.01$
TiO <sub>2</sub> P25	$17 \pm 2$	$2.24 \pm 0.02$
Al <sub>2</sub> O <sub>3</sub> AluC	$140 \pm 50$	$2.05 \pm 0.04$

The fractal dimensions found are about 2, significantly different from the value 2.5 commonly reported in literature. A dimension of 2 is more similar to the dimensions found in clusters formed by cluster–cluster mechanisms than by particle–cluster mechanisms (Fig. 2.2), and could be explained considering that simple agglomerates link with a cluster–cluster mechanism to form complex agglomerates. If simple agglomerates have a size 20–30 μm [10, 16], their Peclet number would be higher than 10<sup>9</sup> [9, 45], indicating a ballistic motion and a ballistic cluster–cluster mechanism for the complex agglomerates. However, the formation of complex agglomerates cannot be ascribed to only one mechanism. Complex agglomerates form, break, combine, and might even compress. Actually, we find slightly different fractal dimensions for the different nanopowders, which means that the formation of complex agglomerates depend on the properties of the nanoparticles and the fluidization conditions. All nanopowders have a prefactor considerably larger than one as a result of the multidimensional nature of complex agglomerates (Eq. 2.4).

As previously mentioned, the agglomerate sphericity plays a minor role in the results. For a sphericity of 0.8, the estimated fractal dimension and prefactor of TiO<sub>2</sub> P25 agglomerates are  $2.25 \pm 0.02$  and  $16 \pm 2$ , respectively. For an sphericity of 0.95, they are  $2.23 \pm 0.02$  and  $18 \pm 3$ , respectively.

The agglomerate density as a function of the gyration diameter is shown in Fig. 2.6. Curiously, there is no significant difference between the density of TiO<sub>2</sub> P25 and T805 nanoparticle agglomerates in the studied size range, although their bulk density is  $\sim 130$

$\text{kg/m}^3$  and  $\sim 300 \text{ kg/m}^3$ , respectively [7]. The difference in the bulk densities is larger than the confidence interval of the calculated densities, revealing that authors should be cautious when approximating the density of nanoparticle agglomerates as the bulk density of the powder [4, 34].  $\text{Al}_2\text{O}_3$  agglomerates have a density larger than  $\text{TiO}_2$  agglomerates, although the particle density is lower and the bulk density is only  $60 \text{ kg/m}^3$  [7]. The larger density comes from the larger prefactor of  $\text{Al}_2\text{O}_3$  agglomerates, which might be the result of a smaller particle size, among other factors (Eq. 2.4).

The reason of the ubiquity of the *fractal dimension* 2.5 in literature (values between 2.5–2.6 are typically reported) is illustrated in Fig. 2.6. The exponent 2.5–2.6, combined with a prefactor one in Eq. (5.1), approximates the density for fluidized agglomerates basically in the whole range of sizes studied from image analysis and bed expansion, due to the huge sensitivity of the agglomerate density to this exponent. For instance, Nam *et al.* [10] calculated from bed settling experiments the average size and fractal dimension of Aerosil R974 nanoparticle agglomerates, obtaining  $160 \mu\text{m}$  and 2.57, respectively. Wang *et al.* [24] obtained an average fractal dimension of 2.5 working with the same powder and similar agglomerate sizes. One could argue that a fractal dimension of 2.5 is in agreement with a fractal dimension of 2.57 because the difference is less than 3 %; however, the densities estimated from these two fractal dimensions differ 100 %. The low sensitivity of the exponent in Eq. (5.1) to large variations in the agglomerate density explains the apparent agreement in literature on a fractal dimension 2.5 for fluidized nanoparticle agglomerates. The exponent 2.5 should not even be interpreted as an *average* or *global* fractal dimension because its value is not the average of  $D_{f,1}$ ,  $D_{f,2}$  and  $D_{f,3}$  but a non-linear combination of them. Eq. (5.1) with  $k_n = 1$  must be interpreted as a mere correlation to (roughly) approximate the density of complex agglomerates.

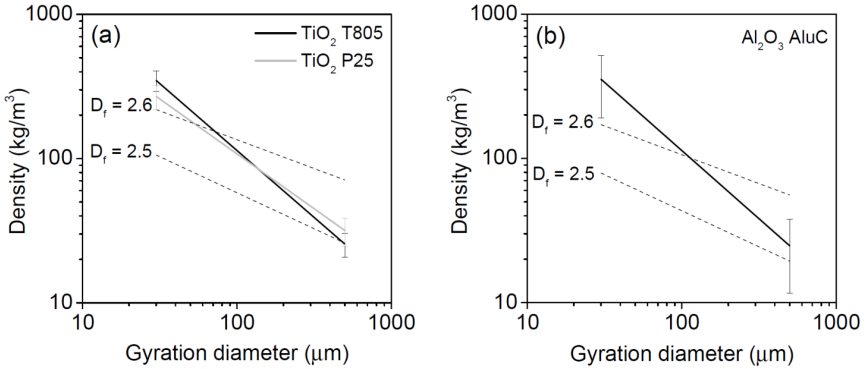


Figure 2.6: Agglomerate density as a function of the agglomerate gyration diameter for (a)  $\text{TiO}_2$  (b)  $\text{Al}_2\text{O}_3$ . Dashed lines represent  $\rho_a = \rho_p (d_{\text{gyr}}/d_p)^{D_f-3}$  for  $D_f = 2.5$  and  $D_f = 2.6$ . Error bars are  $2\sigma$ .

To conclude, we would like to give an outlook on the practical application of our approach. The prefactor of the complex agglomerates, so far inaccessible and ignored in the fluidization field in favor of the fractal dimension, contains key information to understand different aspects of the nanoparticles fluidization. A direct application is the

evaluation of assistance methods used to improve the fluidization quality of nanopowders by breaking the agglomerates [4]. Although they are successfully implemented, the mechanism with which the assistance method breaks the agglomerates is far from being understood. The prefactor can help to this purpose. For instance, if an assistance method changes the average agglomerate size but maintains constant  $D_{f,3}$  and  $\hat{k}_n$ , it means that the assistance method is not affecting  $d_2$  and  $D_{f,2}$ . Probably it is not breaking the simple agglomerates but only reorganizing them to form smaller complex agglomerates. If the assistance method does not change  $D_{f,3}$  but strongly affects  $\hat{k}_n$ , it means that  $d_2$  and/or  $D_{f,2}$  are being affected by the method (assuming  $d_1$  and  $D_{f,1}$  constant because they represent the sintered aggregates). Independently of the average agglomerate size, an assistance method that strongly affects  $\hat{k}_n$  would be more efficient than a method that does not, because the former method is able to break and reorganize the smaller and stronger agglomerate scales.

## 2.4. CONCLUSIONS

The fractal dimension of fluidized nanoparticle agglomerates obtained from settling experiments and the slope  $\log(N_p)$  vs.  $\log(d_{\text{gyr}}/d_p)$  (Eq. 5.1) in the range  $\sim 40\text{--}400\ \mu\text{m}$  reveals that complex agglomerates have a fractal dimension about 2, and a prefactor between 17 and 140, as a result of the multifractal nature of the powder.

The *fractal dimension* between 2.5 and 2.6 commonly reported in literature, is an artifact from using a prefactor unity in the fractal scaling law (Eq. 5.1). A prefactor close to one might be found for mono-dimensional clusters, where the building block is the particle, but does not hold for nanoparticle agglomerates. An exponent 2.5–2.6 combined with a prefactor one roughly approximates the agglomerate density in the range of sizes studied from image analysis and bed expansion. However, this exponent does not describe the scaling of the density with the agglomerate size, which is the real meaning of a fractal dimension, and it does not represent any agglomeration mechanism.

## REFERENCES

- [1] L. de Martin, A. Fabre, and J. R. van Ommen, *The fractal scaling of fluidized nanoparticle agglomerates*, Chemical Engineering Science **112**, 79 (2014).
- [2] L. F. Hakim, J. L. Portman, M. D. Casper, and A. W. Weimer, *Aggregation behavior of nanoparticles in fluidized beds*, Powder Technology **160**, 149 (2005).
- [3] A. Goulas and J. Ruud van Ommen, *Atomic layer deposition of platinum clusters on titania nanoparticles at atmospheric pressure*, J. Mater. Chem. A **1**, 4647 (2013).
- [4] J. R. van Ommen, J. M. Valverde, and R. Pfeffer, *Fluidization of nanopowders: a review*, J Nanopart Res **14**, 737 (2012).
- [5] J. Shabaniyan, R. Jafari, and J. Chaouki, *Fluidization of ultrafine powders*, Int Rev Chem Eng **4**, 16 (2012).
- [6] J. N. Israelachvili, *Intermolecular and Surface Forces*, 3rd ed. (Academic Press, 2011).

- [7] M. Tahmasebpour, L. de Martín, M. Talebi, N. Mostoufi, and J. R. van Ommen, *The role of the hydrogen bond in dense nanoparticle-gas suspensions*, *Phys Chem Chem Phys* **15**, 5788 (2013).
- [8] T. Vicsek, *Fractal Growth Phenomena*, edited by T. Vicsek (World Scientific Pub Co Inc, 1992).
- [9] S. K. Friedlander, *Smoke, Dust, and Haze: Fundamentals of Aerosol Dynamics* (Oxford University Press, 2000).
- [10] C. H. Nam, R. Pfeffer, R. N. Dave, and S. Sundaresan, *Aerated vibrofluidization of silica nanoparticles*, *AIChE Journal* **50**, 1776 (2004).
- [11] J. Quevedo, R. Pfeffer, Y. Shen, R. Dave, H. Nakamura, and S. Watano, *Fluidization of nanoagglomerates in a rotating fluidized bed*, *AIChE J* **52**, 2401 (2006).
- [12] J. M. Valverde and A. Castellanos, *Fluidization of nanoparticles: A modified Richardson-Zaki Law*, *AIChE J* **52**, 838 (2006).
- [13] X. S. Wang, V. Palero, J. Soria, and M. J. Rhodes, *Laser-based planar imaging of nano-particle fluidization: Part ii - mechanistic analysis of nanoparticle aggregation*, *Chemical Engineering Science* **61**, 8040 (2006).
- [14] J. M. Valverde and A. Castellanos, *Fluidization, bubbling and jamming of nanoparticle agglomerates*, *Chem Eng Sci* **62**, 6947 (2007).
- [15] J. M. Valverde, M. A. S. Quintanilla, A. Castellanos, D. Lepek, J. Quevedo, R. N. Dave, and R. Pfeffer, *Fluidization of fine and ultrafine particles using nitrogen and neon as fluidizing gases*, *AIChE J* **54**, 86 (2008).
- [16] J. M. Valverde, M. A. S. Quintanilla, M. J. Espin, and A. Castellanos, *Nanofluidization electrostatics*, *Physical Review E* **77**, 031301 (2008).
- [17] H. Nakamura and S. Watano, *Fundamental particle fluidization behavior and handling of nano-particles in a rotating fluidized bed*, *Powder Technol* **183**, 324 (2008).
- [18] M. A. S. Quintanilla, J. M. Valverde, A. Castellanos, D. Lepek, R. Pfeffer, and R. N. Dave, *Nanofluidization as affected by vibration and electrostatic fields*, *Chem Eng Sci* **63**, 5559 (2008).
- [19] M. J. Espin, J. M. Valverde, M. A. S. Quintanilla, and A. Castellanos, *Electromechanics of fluidized beds of nanoparticles*, *Physical Review E* **79** (2009).
- [20] D. To, R. Dave, X. Yin, and S. Sundaresan, *Deagglomeration of nanoparticle aggregates via rapid expansion of supercritical or high-pressure suspensions*, *AIChE J* **55**, 2807 (2009).
- [21] P. Ammendola, R. Chirone, and F. Raganati, *Fluidization of binary mixtures of nanoparticles under the effect of acoustic fields*, *Mater Sci Forum* **22**, 174 (2011).

- [22] J. Hyeon-Lee, G. Beaucage, S. E. Pratsinis, and S. Vemury, *Fractal analysis of flame-synthesized nanostructured silica and titania powders using small-angle x-ray scattering*, *Langmuir* **14**, 5751 (1998).
- [23] H. K. Kammler, G. Beaucage, R. Mueller, and S. E. Pratsinis, *Structure of flame-made silica nanoparticles by ultra-small-angle x-ray scattering*, *Langmuir* **20**, 1915 (2004).
- [24] X. S. Wang, V. Palero, J. Soria, and M. J. Rhodes, *Laser-based planar imaging of nanoparticle fluidization: Part i: determination of aggregate size and shape*, *Chem Eng Sci* **61**, 5476 (2006).
- [25] M. A. S. Quintanilla, J. M. Valverde, M. J. Espin, and A. Castellanos, *Electrofluidization of silica nanoparticle agglomerates*, *Ind Eng Chem Res* **51**, 531 (2012).
- [26] L. de Martín and J. R. van Ommen, *A model to estimate the size of nanoparticle agglomerates in gas-solid fluidized beds*, *J Nanopart Res* **15**, 2055 (2013).
- [27] B. B. Mandelbrot, *The Fractal Geometry of Nature* (W. H. Freeman and Company, 1982).
- [28] C. M. Sorensen and G. C. Roberts, *The prefactor of fractal aggregates*, *J Colloid Interf Sci* **186**, 447 (1997).
- [29] Q. Jiang and B. E. Logan, *Fractal dimensions of aggregates determined from steady-state size distributions*, *Environ Sci Technol* **25**, 2031 (1991).
- [30] A. M. Brasil, T. L. Farias, and M. G. Carvalho, *A recipe for image characterization of fractal-like aggregates*, *J Aerosol Sci* **30**, 1379 (1999).
- [31] M. L. Eggersdorfer and S. E. Pratsinis, *The structure of agglomerates consisting of polydisperse particles*, *Aerosol Sci Technol* **46**, 347 (2012).
- [32] G. Bushell, Y. Yan, D. Woodfield, J. Raper, and R. Amal, *On techniques for the measurement of the mass fractal dimension of aggregates*, *Adv Colloid Interface Sci* **95**, 1 (2002).
- [33] L. Ehrl, M. Soos, and M. Lattuada, *Generation and geometrical analysis of dense clusters with variable fractal dimension*, *J Phys Chem B* **113**, 10587 (2009).
- [34] W. Yao, G. Guangsheng, W. Fei, and W. Jun, *Fluidization and agglomerate structure of SiO<sub>2</sub> nanoparticles*, *Powder Technol* **124**, 152 (2002).
- [35] G. P. Sanganwar, R. B. Gupta, A. Ermoline, J. V. Scicolone, and R. Dave, *Environmentally benign nanomixing by sonication in high-pressure carbon dioxide*, *J Nanopart Res* **11**, 405 (2009).
- [36] L. de Martín, W. G. Bouwman, and J. R. van Ommen, *Two-level hierarchical structure in nano-powder agglomerates in gas media*, in *Bulletin of the American Physical Society. 65th Annual Meeting of the APS Division of Fluid Dynamics*, Vol. 57 (2012).

- [37] M.-O. Coppens, *Characterization of fractal surface roughness and its influence on diffusion and reaction*, Colloid Surface A **187–188**, 257 (2001).
- [38] V. Fidleris and R. L. Whitmore, *Experimental determination of the wall effect for spheres falling axially in cylindrical vessels*, Brit J Appl Phys **12**, 490 (1961).
- [39] L. de Martín, J. Sánchez-Prieto, F. Hernández-Jiménez, and J. R. van Ommen, *A settling tube to determine the terminal velocity and size distribution of fluidized nanoparticle agglomerates*, (2013).
- [40] B. Erdem, R. A. Hunsicker, G. W. Simmons, E. D. Sudol, V. L. Dimonie, and M. S. El-Aasser, *XPS and FTIR surface characterization of TiO<sub>2</sub> particles used in polymer encapsulation*, Langmuir **17**, 2664 (2001).
- [41] Y. Feng, J. Goree, and B. Liu, *Accurate particle position measurement from images*, Rev Sci Instrum **78**, 053704 (2007).
- [42] A. Haider and O. Levenspiel, *Drag coefficient and terminal velocity of spherical and nonspherical particles*, Powder Technol **58**, 63 (1989).
- [43] S. J. Blott and K. Pye, *Particle shape: a review and new methods of characterization and classification*, Sedimentology **55**, 31 (2008).
- [44] N. A. Riley, *Projection sphericity*, J Sediment Res **11**, 94 (1941).
- [45] L. Mädler, A. A. Lall, and S. K. Friedlander, *One-step aerosol synthesis of nanoparticle agglomerate films: simulation of film porosity and thickness*, Nanotechnology **17**, 4783 (2006).
- [46] H. C. Brinkman, *A calculation of the viscous force exerted by a a flowing fluid on a dense swarm of particles*, Appl Sci Res **A1**, 27 (1947).
- [47] H. C. Brinkman, *On the permeability of media consisting of closely packed porous particles*, Appl Sci Res **A1**, 81 (1949).
- [48] S. Veerapaneni and M. R. Wiesner, *Hydrodynamics of fractal aggregates with radially varying permeability*, J Colloid Interf Sci **177**, 45 (1996).

## APPENDIX 2.A

### PERMEABILITY OF THE AGGLOMERATES

According to Brinkman [46, 47], the drag coefficient of a permeable sphere  $C_D$  relates to the drag coefficient of the same impermeable sphere  $C_D^*$  as  $C_D = \Omega C_D^*$ , where  $\Omega$  is a parameter that depends on the size and structure of the porous sphere. For flow in the Stoke's regime and agglomerates with  $D_f > 2$ ,  $\Omega$  can be determined with Darcy's Law (Eq. 2.10).

$$\Omega = \frac{2\xi^2}{2\xi^2 + 3} \quad (2.10)$$

For the same flow and agglomerates with  $D_f < 2$ ,  $\Omega$  can be determined with Brinkman's Law (Eq. 2.11) [32].

$$\Omega = \frac{2\xi^2(1 - \tanh \xi/\xi)}{2\xi^2 + 3(1 - \tanh \xi/\xi)} \quad (2.11)$$

where

$$\xi = \frac{d_h}{2\sqrt{\kappa}} \quad (2.12)$$

and [32, 48]

$$\kappa = \frac{d_p^2}{18\gamma^3} \frac{3 - 4.5\gamma + 4.5\gamma^5 - 3\gamma^6}{3 + 2\gamma^5} \quad (2.13)$$

where  $\gamma = (1 - \epsilon)^{1/3}$ ,  $d_p$  is the diameter of the primary particles and  $d_h$  is the hydrodynamic diameter of the agglomerates.

To establish whether it is necessary to account for permeability in the agglomerates we will focus on two hypothetical agglomerates: one with a size of  $d_1 = 30 \mu\text{m}$  and  $\rho_{a1} = 200 \text{ kg/m}^3$  and one with of  $d_2 = 400 \mu\text{m}$  and  $\rho_{a2} = 10 \text{ kg/m}^3$ . These agglomerates represent the smallest and largest agglomerates measured in this work. Real agglomerates are denser than these two cases; thus, if the permeability can be neglected for these hypothetical agglomerates, it can certainly be neglected for the real agglomerates.

For a particle density of  $3900 \text{ kg/m}^3$ , similar to the particle density of  $\text{TiO}_2$  and  $\text{Al}_2\text{O}_3$ , the porosity of the agglomerates is  $\epsilon_1 = 0.949$  and  $\epsilon_2 = 0.998$ . For a particle size of  $17 \text{ nm}$ ,  $\xi_1 = 1262$  and  $\xi_2 = 2678$ , leading to  $\Omega_1 \sim \Omega_2 \sim 1$  for Darcy's and Brinkman's Laws. The agglomerates can therefore be considered impermeable.





# 3

## CONTACT MECHANICS OF HIGHLY POROUS OXIDE NANOPARTICLE AGGLOMERATES

Efficient nanopowder processing requires knowledge of the powder's mechanical properties. Due to the large surface area to volume ratio, nanoparticles experience relatively strong attractive interactions, leading to the formation of micron-size porous structures called agglomerates. Significant effort has been directed towards the development of models and experimental procedures to estimate the elasticity of porous objects such as nanoparticle agglomerates; however, none of the existing models has been validated for solid fractions below 0.1. Here, we measure the elasticity of titania ( $\text{TiO}_2$ ), alumina ( $\text{Al}_2\text{O}_3$ ), and silica ( $\text{SiO}_2$ ) nanopowder agglomerates by Atomic Force Microscopy, using a  $3.75\ \mu\text{m}$  glass colloid for the stress-strain experiments. Three sample preparations with varying degree of powder manipulation are assessed. The measured Young's moduli are in the same order of magnitude as those predicted by the model of Kendall et al., thus, validating it for the estimation of the Young's modulus of structures with porosity above 90%.

---

Published as: A. Fabre, S. Salameh, L. Colombi Ciacchi, M. T. Kreutzer, J. R. van Ommen. Contact mechanics of highly porous oxide nanoparticle agglomerates. *Journal of Nanoparticle Research*, 18:1-13, 2016 [1].

### 3.1. INTRODUCTION

The mechanical properties of nanopowders are critical for the optimization of their processing [2–4]. These properties are crucial in gas phase processes involving agglomerate collision such as in flame aerosol reactors [5, 6], lung nanoparticle uptake studies [7], and nanopowder fluidization [8]. The processing method of fluidization, where the powder is suspended in a gas stream moving upwards, is known to enhance fluid to solid contact by powder dispersion [9–13], which is beneficial for heat and mass transfer, and widely used in gas-solid reaction, granulation, and particle coating, drying, and mixing, among many other applications. Nonetheless, nanoparticles (NP) fluidize as clusters called agglomerates [14–17], making the dynamics within the fluidized bed complex and challenging to study, mainly due to the lack of accurate characterization of the agglomerates [18].

Nanopowders agglomerate in a stepwise fashion [19]. During synthesis at high temperatures, primary particles form chemical bonds creating chain-like structures called aggregates, reaching sizes of 100s of nm. These aggregates then cluster together by physical interactions forming simple agglomerates with sizes of a few 10s of  $\mu\text{m}$ , mainly during powder storage. Finally, the simple agglomerates assemble into complex agglomerates, which can reach sizes of 100s of  $\mu\text{m}$ . As a hierarchical process, each level has structures with particular features such as fractal dimension [20, 21]. This research focuses on the agglomerate properties since these are the structures readily available from stored nanopowder and found during nanopowder processing in the gas phase.

Agglomeration arises from the relatively strong attractive interactions among NPs, which include capillary, solvation, van der Waals, and electrostatic forces [10, 22–28]. Electrostatic forces diminish in the presence of humidity, but can occur in very dry environments. In earlier studies, it was shown that physisorbed water molecules situate between the nanoparticles creating an attractive interaction described by a combination of capillary and solvation forces, which can surpass the van der Waals contribution [18, 22]. During nanopowder processing, attractive forces are challenged by external separation forces such as collision [8]. In order to estimate the magnitude of the forces acting on the agglomerates, and thus, their morphological stability at the given conditions, their Young's modulus must be known. The high porosity ( $>90\%$ ) and rather large size of these structures ( $\approx 100 \mu\text{m}$ ) make them extremely fragile. Therefore, stress measurements to study their mechanical properties are particularly challenging.

Because of their large void fraction, nanoparticle agglomerates are expected to have a relatively low Young's modulus. Due to their fragile nature, any type of manipulation can easily compromise the morphological integrity of the agglomerates and reproducibility of the results. Thus, all techniques considered for the study of agglomerates have to be evaluated for the degree of morphological modification and data reproducibility. Additionally, the number of available techniques to study structures in the micron-size scale with nano scale resolution is very limited. A quite challenging property to measure is elasticity, mainly due to the structural and technical limitations just mentioned. There have been novel techniques to measure elasticity of soft microscopic objects such as microcapillaries, relying on pressure-induced deformation of microscopic deformable particles in a dilute suspension [29], the ultrasonic pulse-echo method by measuring the velocity of ultrasonic waves in materials along a known crystal direction for isotropic,

millimeter thick samples [30, 31], or the compression and indentation techniques such as Atomic Force Microscopy (AFM). Methods that require the samples to be in the liquid phase, specifically oriented, or placed at a set location will considerably affect the original structure of the nanoparticle cluster and hinder result reproducibility.

Agglomerate elasticity has been measured before; however, those agglomerates had a significantly higher solid fraction, well defined geometry, and/or customized formation process than those of interest in this research. In 1987, Kendall et al. [32] measured the elasticity of ceramic NP clusters to study the effect of solid fraction, developing a model to estimate the effective Young's modulus in terms of the volume packing, and particle interface energy, size, and modulus. Nonetheless, the experiments were limited to structures with porosity below 70% [32]. Later on, in 1992, Kendall focused on the elasticity of spray-dried spherical agglomerates of uniformly packed 210 nm zirconia particles [33], modeling the steps towards agglomerate fracture, and describing the use of a nanoindenter to study agglomerate deformation; again, facing the porosity limitation. In 2001, Bika et al. [3] presented a summary of studies done on the mechanical properties of wet and dry agglomerates, highlighting their morphological frailty, and the lack of proper measuring techniques and realistic theoretical models to obtain accurate values of the agglomerate mechanical properties. Nonetheless, all the data gathered from literature and reviewed by Bika et al. is for agglomerates with porosity below 75%.

The elasticity, represented as the Young's modulus, of porous materials can be predicted from theoretical models found in literature [30]. These models consider the agglomerate volume fraction and primary particle Young's modulus as critical variables to determine the agglomerate Young's modulus. However, the models of Hasselman [34], Wang [35], Martin-Haynes [36], and Phani-Niyogy [37] have fitting parameters that rely on elasticity experimental data; thus, not really predicting the value. The models of Hashin [30] and Hashin-Rosen [30] require previous knowledge of the shear and bulk modulus of the porous structure, and Poisson's ratio of the NP, which leads to a straightforward calculation of the elasticity. Nonetheless, these values are unknown for nanoparticle agglomerates. Kendall et al. [32] developed a model with a simple expression that uses the agglomerate solid fraction and NP Young's modulus, work of adhesion, and diameter to estimate the effective elasticity of the porous agglomerate, which can be obtained from commercial suppliers or literature. However, to the best of our knowledge, none of these models has been experimentally validated for structures with porosity above 90% such as those seen in nanopowders.

A well-established technique to study the elasticity of soft matter is the AFM, which works by forcing an interaction between a probe and the sample. The versatility of the technique allows for the visualization of topographic characteristics to an atomic level, the quantification of interacting forces between nano-sized objects, metal deposition on electroconductive substrates, and the measurement of mechanical properties of soft materials [4, 18, 38–47]. This includes fragile micron/nano-sized systems such as muscle cells [48] and thin gels [48] among many other applications [4, 18, 49–56]. In earlier studies, the AFM equipped with a glass colloid attached to the cantilever was used to measure the Young's modulus of highly porous NP films [57, 58]. To neglect extra phenomena such as adhesion forces and plasticity, only the approach part of the force curve was fitted to the Hertz model for elasticity estimations. However, these films differ from

the fluidized agglomerates on the mechanism of formation, homogeneity, and stability, with porosity still bellow that of the complex nanoparticle agglomerates. This method is widely accepted for materials in the kPa-MPa range such as biological samples [59–61].

The objective of this work is to present an experimental method to measure the elasticity of nanopowder agglomerates, which typically have a porosity above 90%. The results are used to validate the applicability of elasticity models for highly porous structures. Three sample preparation approaches are compared to verify the conservation of the structure, and measurement accuracy and reproducibility. To preserve the original morphology of the agglomerate, the technique requiring the least manipulation during sample preparation is used to investigate hydrophilic titania ( $\text{TiO}_2$  - P25), alumina ( $\text{Al}_2\text{O}_3$  - Alu C), and silica ( $\text{SiO}_2$  - A130) nanopowders. The experimental results are compared to theoretical models from literature, and the Kendall et al. [32] method was found to give a descent estimation.

## 3.2. EXPERIMENTAL SECTION

### 3.2.1. POWDER CHARACTERIZATION

The nanopowders used in this study are Aerioxide P25 ( $\text{TiO}_2$ ), Aerioxide Alu C ( $\text{Al}_2\text{O}_3$ ), and Aerosil A130 ( $\text{SiO}_2$ ), obtained from Evonik with the specifications given in Table 4.2. To verify the powder characteristics, the primary particle size was determined from TEM images by manually counting 250, 678, and 706 particles for  $\text{TiO}_2$ ,  $\text{Al}_2\text{O}_3$ , and  $\text{SiO}_2$ , respectively, using the open source image processing software ImageJ. The mean values obtained are  $22 \pm 8$  nm,  $16 \pm 6$  nm, and  $8 \pm 2$  nm for  $\text{TiO}_2$ ,  $\text{SiO}_2$ , and  $\text{Al}_2\text{O}_3$ , respectively (Fig.3.1), where the  $\pm$  values are the standard deviation of each dataset. These values agree with those specified by the supplier (Table 4.2), with the exception of  $\text{Al}_2\text{O}_3$ , which showed a significantly lower mean size. The discrepancy could arise from the subjective particle selection during image analysis by measuring only those shades that clearly seem to be individual particles, as most of them are sintered (connected by solid necks) (Fig.3.1 inset). Also, the inconsistency could come from the use of different measuring techniques since the average size given from production is determined by the gas adsorption-desorption method, which could deviate from that obtained from the TEM image analysis.

Table 3.1: Properties of the nanopowders as provided by the manufacturer and obtained from TEM image analysis.

powder	surface	$\rho_p$ ( $\text{kg}/\text{m}^3$ )	$d_p$ (nm)	$d_{p(TEM)}$ (nm)
$\text{TiO}_2$ P25	hydrophilic	4000	21	$22 \pm 8$
$\text{Al}_2\text{O}_3$ AluC	hydrophilic	3800	13	$16 \pm 6$
$\text{SiO}_2$ A130	hydrophilic	2200	16	$8 \pm 2$

### 3.2.2. SAMPLE PREPARATION

Three sample preparation methods were tested, referred to as: pressed on glass, double sided tape, and rough substrate. For the powder pressed on glass, a small amount of the nanopowder is placed on a glass microscope slide over an area of about  $1\text{cm}^2$ ,

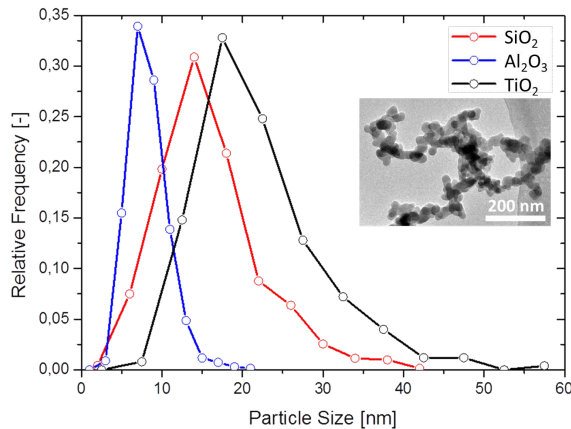


Figure 3.1: Size distribution of nanoparticles measured from TEM images using ImageJ. 250, 678, and 706 particles were counted for TiO<sub>2</sub>, Al<sub>2</sub>O<sub>3</sub>, and SiO<sub>2</sub>, respectively. The inset is a TEM image of Al<sub>2</sub>O<sub>3</sub> showing sintered nanoparticles.

and pressed using a thick piece of flat glass until leaving a homogeneous layer of powder looking uniform to the naked eye. The double sided tape method involves the spreading of powder over a transparent double sided tape (Scotch) attached to a glass slide. Then, the sample is gently shaken to remove any loose powder without blowing or touching, to prevent morphological changes. Similarly, the rough surface preparation starts with the spreading of powder on the rough side of a microscope slide, with a final gentle shake to remove the excess powder. These spreading and shaking steps are repeated a few times to ensure a thick enough powder layer for AFM measurements. Due to the extent of manipulation, the pressed on glass method deliberately modifies the structure of the powder; while the sample on the rough substrate is expected to have an almost unchanged morphology. Comparably, the double sided tape technique is believed to preserve the original structure of the agglomerates. However, the effect of the glue on the mechanical properties was questionable, and thus, evaluated.

All three samples were characterized by SEM imaging. A SEM (Jeol JSM-6010 LA) was used to evaluate the general morphology of the nanopowder film on the smooth glass, rough surface, and double sided tape. To assess the glue-powder integration, images of the tilted double sided tape sample were taken and analyzed. Before SEM imaging, the samples were slightly blown to prevent nanopowder contamination of the sample chamber.

### 3.2.3. ELASTICITY MEASUREMENTS

The stress-strain measurements were done in a Nanowizard 3 AFM from JPK. The experiments were performed using a probe with a glass colloid of 3.5  $\mu\text{m}$  in diameter bought from sQube (CP-FM-SiO-B)(see Appendix). This colloid size is large enough to prevent local indentation through the primary particles, and apply pressure on an area encompassing nanoparticles agglomerates. The spring constants of 2.6  $\text{N}/\text{m}$ , 3.5  $\text{N}/\text{m}$ , and 3.9

$N/m$  for  $\text{Al}_2\text{O}_3$ ,  $\text{SiO}_2$ , and  $\text{TiO}_2$  on double sided tape, respectively; and  $3.8 N/m$  and  $4.4 N/m$  for  $\text{TiO}_2$  on a rough substrate and pressed on glass, respectively, were determined using the thermal noise method [62, 63]. Single force curves were recorded on  $8 \times 8$  grids in an area of  $10 \times 10 \mu\text{m}$  to average local differences. The applied force was  $150 nN$  with a cantilever approach/retraction speed of  $2 \mu\text{m}/\text{s}$ . To avoid glue-colloid contact, the agglomerates were located before each stress-strain experiment by a microscope positioned right below the sample (Fig.3.2).

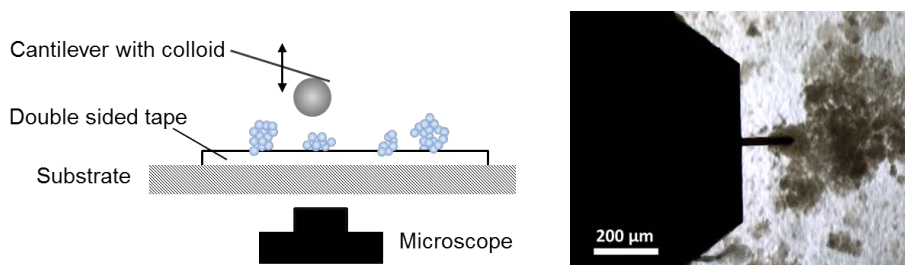


Figure 3.2: Schematic representation of the experimental set up for the double sided tape sample preparation method. The nanopowder is attached to a glass microscope slide (substrate) using transparent double sided tape. The  $3.5 \mu\text{m}$  colloid attached to the cantilever is aligned to the desired position on the sample with the help of a microscope located directly below the sample before each elasticity measurement. The image on the right is of  $\text{Al}_2\text{O}_3$  on double sided tape, taken by the AFM microscope.

The Young's modulus was calculated using the JPKSPM Data Processing software by fitting the Hertz model [64] to the approach curves. First, the baseline was subtracted from the curves to set the point of cantilever-sample contact at zero and have displacement equal to indentation. Then, the x offset (contact point) was adjusted and the height for cantilever bending, corrected previous to the Young's modulus estimation using the embedded "determine elasticity from indentation" software function. Retraction curves were not considered for elasticity measurements of the agglomerates; hence, only the approach curves are presented and used for the estimation of the Young's modulus. Other contact mechanics models such as Johnson-Kendall-Roberts (JKR)[65], Derjaguin-Muller-Toporov (DMT) [66], and Maugis-Dugdale (MD)[67], which account for adhesion forces [51, 53], were also considered.

### 3.3. RESULTS & DISCUSSION

#### 3.3.1. SAMPLE CHARACTERIZATION

From the TEM pictures, it is evident that nanoparticles are found in clusters. These structures are very porous and expected to be susceptible to changes by external disturbances. Therefore, any powder manipulation and processing will dramatically modify their original morphology. Insufficient analysis and understanding of the handling effect can lead to erroneous conclusions regarding the nature of the nanoparticle clusters.

Sample preparation was thoroughly evaluated to prevent false conclusions due to the fragility of the agglomerates. The soft spreading and gentle shake for the rough surface and double sided tape sample preparation methods show fluffy structures, as expected from unprocessed nanopowder (Fig.3.3, (a-b)). On the other hand, the powder

pressed on glass shows a flat and dense surface arising from the pressing step (Fig.3.3, (c)). Nonetheless, the pressed film seems to keep a highly porous morphology underneath the flat surface (Fig.3.3, (d)). The SEM images showed a morphology similar to naturally formed complex agglomerates for the rough surface and double sided tape samples, while there was considerable modification on the pressed on glass nanopowder film.

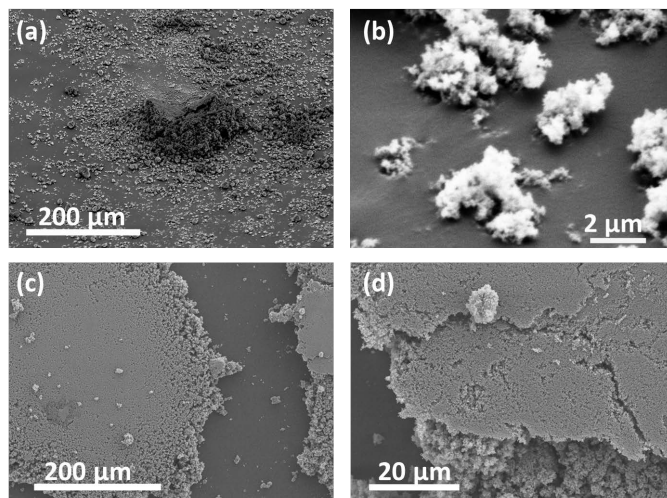


Figure 3.3: SEM pictures of  $\text{TiO}_2$  nanopowder samples. (a) and (b): spread on double sided tape. (c) and (d): pressed on glass. The porosity, distribution, and morphology of the powder clusters are noticeably different between the double sided tape and pressed on glass samples. Images (a-b) show the agglomerates attached to the double sided tape. The pressed powder cluster shows a very uniform flat surface with a few loose agglomerates on top (c), and an edge that resembles the structure of the spread powder (d).

Besides the preparation method, the sample substrate could also affect the AFM measurements. From SEM images, it was seen that the powder film thickness is considerably larger than the colloid indentation depth (Fig.3.3), and since the elasticity of the solid substrates is known to be orders of magnitude higher than that of the porous film, the substrates should not have an effect on the measurements. However, the possibility of glue penetration by capillary into the highly porous structures led to extra evaluation of samples placed on the double sided tape. These samples were assessed by tilted SEM imaging, where the glue was found to immerse less than  $0.5 \mu\text{m}$  of the attached agglomerates (Fig.3.3, (b)). Thus, the glue, as well as the solid substrates, is expected to have negligible to no influence on the AFM measurements, leaving any measurement discrepancy to the preparation method itself.

### 3.3.2. FORCE CURVE ANALYSIS

For an ideal elastic sample, the slope of approach and retraction part does not differ. However, in the case of the highly porous agglomerates, there is a large hysteresis between approach and retraction (Fig.3.4 (a)). To investigate the elasticity of porous samples by AFM, the approach part of the force curve should be analyzed [58]. This is due to



the complexity of the retraction curve, which includes other phenomena such as strong short range adhesion forces between the colloid and the agglomerate that lead to deformation of the agglomerate while the cantilever retracts. Moreover, a certain amount of approach curves (< 33%) show plastic deformations and an inaccurate fit of the Hertz model (Fig.3.4 (b)); hence, were eliminated from data analysis (see Appendix).

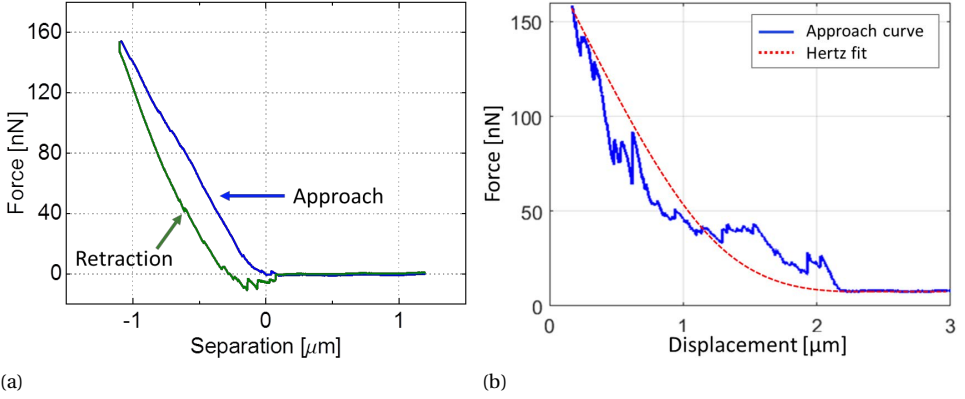


Figure 3.4: (a) Full force curve of an alumina ( $\text{Al}_2\text{O}_3$ ) sample measured by AFM. The approach part of the curve is shown in blue and the retraction part, in green. The horizontal axis is the separation between the colloid and the sample. The hysteresis between the approach and retraction curves, in addition to the multiple peaks on the retraction curve suggest elastic deformation of the sample. (b) Force versus displacement curve showing multiple peaks on the retraction curve, suggesting elastic deformation of the sample. Example of a plot not included in the analysis.

The approach part of the force curves obtained from the AFM measurements were fitted using the Hertz model [64] to calculate the Young's modulus of each sample (Fig.3.12(a)). A total of five samples were analyzed, consisting of  $\text{Al}_2\text{O}_3$ ,  $\text{SiO}_2$ , and  $\text{TiO}_2$  on double sided tape,  $\text{TiO}_2$  on a rough surface, and  $\text{TiO}_2$  pressed on glass. None of the samples showed measurable long distance adhesion forces towards the colloid; therefore, models such as DMT, JKR, and MD, which require adhesion for proper fitting, were excluded (Fig.3.12(c)).

The Hertz model is described by the following equation:

$$F_{Hertz} = \frac{4}{3} \frac{E^*}{1 - \nu^{*2}} R_{Tip}^{\frac{1}{2}} (s_0 - s)^{\frac{3}{2}} \quad (3.1)$$

where  $E^*$  and  $\nu^*$  are the Young's modulus and Poisson's ratio of the powder sample, respectively;  $R_{Tip}$  is the radius of the glass colloid,  $s_0$  is the colloid-sample contact distance, and  $s$  is the penetration depth. The Hertz model assumes an isotropic and linear elastic solid sample, non-deformable indenter, no additional interactions between the indenter and sample, negligible indentation compared to the sample thickness, absolute elastic behavior, and a homogeneous sample [68]. Relative to the soft powder films, the indenter is considered non-deformable. Furthermore, the approach curves used for elasticity analysis did not show additional interactions between the colloid and the film.

The calculated Young's modulus agrees with the hypothesis developed based on the level of powder manipulation during sample preparation. The moduli of the double

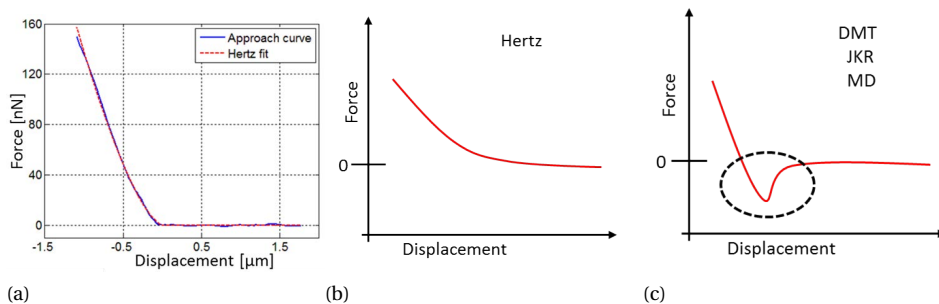


Figure 3.5: Hertz fit to the approach part of an experimental force versus displacement curve (a). Hertz contact model curve in a force versus displacement plot (b). General force versus displacement curve for the DMT, JKR and MD models, which account for the effect of adhesion (c).

sided tape and rough substrate are in the same order of magnitude, with a slightly wider distribution for the rough substrate, and a maximum and minimum values similar to those of the double sided tape. Nonetheless, the pressed on glass sample has a Young's modulus more than one order of magnitude higher (Fig.3.6) as a consequence of the denser film made by pressing. The pressed on glass sample also shows a wider distribution, which could arise from the loose agglomerates present on the surface (Fig.3.3, B), or any film defect caused by uneven compression or irregular release behavior. Therefore, we have selected the double sided tape technique as the most reliable sample preparation method.

### 3.3.3. ELASTICITY OF DIFFERENT MATERIALS

The elasticity of the nanopowder depends on the particle packing, size distribution, shape, surrounding conditions, powder processing, and contact forces. Three common oxide nanopowders of different material and primary particle size were studied, namely  $\text{Al}_2\text{O}_3$ ,  $\text{SiO}_2$ , and  $\text{TiO}_2$ . The packing density depends on the size distribution, powder processing, and particle shape, affecting the space available for particle rearrangement. Additionally, the interparticle forces are affected by material properties such as the Hamaker coefficient and surface hydrophobicity. Thus, each of the three powders has an elasticity which depends on the unique material properties and particle morphology.

The Young's modulus of the powders was calculated by fitting the Hertz model to 219, 305, and 142 curves for  $\text{SiO}_2$ ,  $\text{Al}_2\text{O}_3$ , and  $\text{TiO}_2$ , respectively. Two of the materials,  $\text{Al}_2\text{O}_3$  and  $\text{TiO}_2$ , showed a Young's modulus within the same range in the order of 100 kPa, while  $\text{SiO}_2$  was an order of magnitude lower (Fig.3.7), and with a noticeably narrower distribution. The low Young's modulus means that the  $\text{SiO}_2$  agglomerate layer is easier to compress. During the measurements, the force applied on the sample by the colloid is specified; this force is directly proportional to the Hamaker coefficient and elastic deformation of the sample [69]. Since the Hamaker coefficient of silica ( $\text{SiO}_2$ ) is about an order of magnitude smaller than that of  $\text{Al}_2\text{O}_3$  and  $\text{TiO}_2$  [70], a more prominent deformation was expected and indeed obtained, describing a soft, highly elastic material. Further-

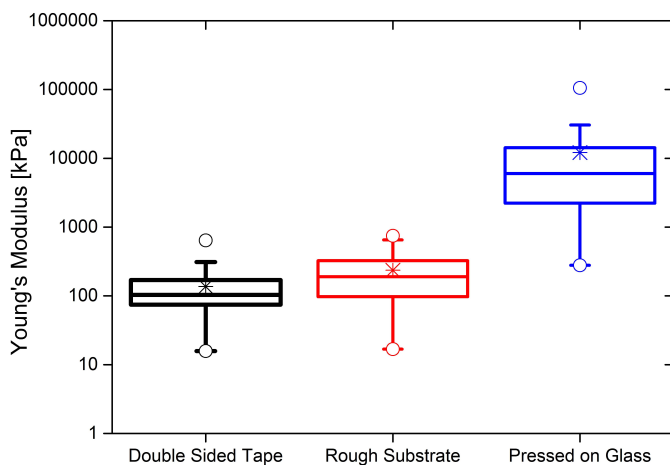


Figure 3.6: Young's modulus of TiO<sub>2</sub> measured using different sample preparation methods. The double sided tape and rough substrate preparation methods consist of powder spreading on substrate, and gentle shaking to remove excess powder. The pressed on glass method squeezes the powder between two flat pieces of glass. The asterisks are the mean values and the empty circles are the maximum and minimum values. The box encompasses the second and third quartiles, divided by a line corresponding to the median. The top and bottom whiskers are the outliers with coefficient 1.5.

more, other factors such as the degree of particle surface roughness and porosity could contribute to the low Young's modulus of SiO<sub>2</sub>, and should be further investigated.

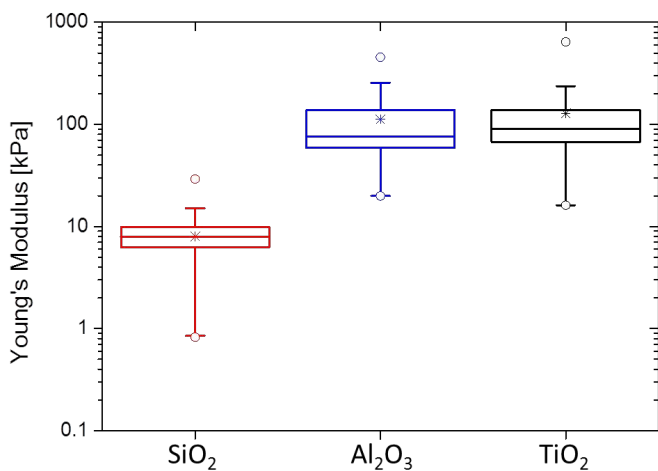


Figure 3.7: Young's modulus measured for TiO<sub>2</sub>, SiO<sub>2</sub>, Al<sub>2</sub>O<sub>3</sub> on double sided tape

As seen from Figure 3.7, the values show a wide distribution. This distribution is typical for AFM measurements. Even in the case of perfectly flat substrates such as mica or silicon, AFM values always show wide distribution based on a different number of

molecules coming into contact at each measurement [44, 58]. However, in the case of porous agglomerates, the contact scenario shows even more variation between measurements since the sample surface is rather heterogeneous, leading to a wider range of measured values.

### 3.3.4. THEORETICAL ELASTICITY

The elasticity of each powder was calculated theoretically using the model of Kendall et al. (1987). According to Kendall's model, the effective elasticity of the powder sample can be estimated from:

$$E^* = 17.1\phi^4 \left[ \frac{E^2\Gamma}{d_p} \right]^{1/3} \quad (3.2)$$

where  $\phi$  is the solid volume fraction, and  $E$ ,  $\Gamma$ , and  $d_p$ , the Young's modulus, work of adhesion, and diameter of the nanoparticles, respectively. This model was developed for anisotropic packing of spherical particles into complex structures with different shapes. All shapes fell into one curve represented by equation (5.1) where the coefficient 17.1 is found from the fit. The dependence of the effective Young's modulus on the solid fraction to the fourth power arises from a square dependence on the shear modulus ( $G$ ), and a second one on the coordination number ( $N_{Co}$ ).

The applicability of the model to highly porous nanoparticle agglomerates was evaluated. The coordination number of porous structures with solid fraction between 0 and 0.1 still has a square dependence as estimated from literature [71]. The original expression to calculate the coordination number is an exponential sum that leads to the Taylor series  $N_{Co} = 1.99 + 0.59\phi + 11.02\phi^2 - 0.02\phi^3 + 10.27\phi^4 + O(\phi^5)$ , which results in a parabola for small  $\phi$ . Additionally, the square influence of the density packing on the modulus described for the material with a random distribution of isolated spherical holes [72] could still apply to highly porous structures with randomly distributed particle chains such as nanoparticle agglomerates. A Taylor expansion of the original formula reads as:

$$G = \sum_{n=1}^{\infty} \frac{4 \cdot 3^{n-1} k_0^n \mu_0 \phi^n}{(3k_0 + 4\mu_0)^n} \quad (3.3)$$

where  $k_0$  is the bulk modulus and  $\mu_0$  the shear modulus, which can be taken as a quadratic polynomial for solid fractions in the nanoparticle agglomerate range since terms with higher degrees lead to values more than two orders of magnitude smaller. Therefore, we believe that Kendall's model can be used to estimate the elasticity of structures with solid fractions lower than 0.1 such as the highly porous nanopowder layers presented in this work.

For hydrophilic TiO<sub>2</sub> (P25), with a solid fraction of 0.03 [73], work of adhesion of 0.8 J/m<sup>2</sup> [32, 74], particle diameter of 22 nm (Fig.3.1), and particle elasticity of 234 GPa [75] we obtain a Young's modulus of 174 kPa, which is in close agreement with the results from the AFM. The values used for SiO<sub>2</sub> (A130) and Al<sub>2</sub>O<sub>3</sub> (AluC) are shown in Table 6.2, resulting in Young's moduli of 10 kPa and 129 kPa, respectively. The work of adhesion is calculated as twice the surface energy of the material, which is taken from Navrotsky's paper [74]. Since the estimation of surface energy depends on the experimental method

and conditions showing strong variations in literature, the paper of Navrotsky et al. was chosen as it includes all three powders used in this study. The theoretical and experimental values are compared in Figure 3.8, where the empty circles correspond to the theoretical values with bars representing the spread arising from the nanoparticle size distribution; and the solid circles representing the experimental mode with error bars as the standard deviation for log-normal distribution of the data.

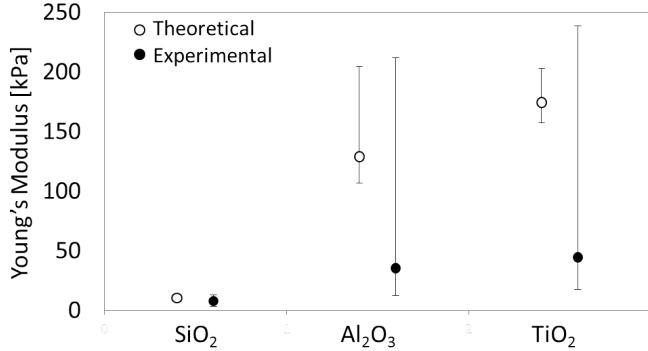


Figure 3.8: Experimental and theoretical values of the Young's moduli for SiO<sub>2</sub>, Al<sub>2</sub>O<sub>3</sub>, and TiO<sub>2</sub> on double sided tape. Experimental values obtained from AFM measurement (solid circles), and theoretical from equation(5.1) (empty circles) are shown. Error bars are the standard deviation of the curves used to calculate the log-normal experimental elasticity, and the standard deviation from the nanoparticle size distribution as estimated from TEM images.

Table 3.2: Values used for the estimation of the effective Young's modulus

material	$\phi^a$	$\Gamma [J/m^2]^b$	$E [GPa]^c$	$d_p [nm]$
TiO <sub>2</sub> - P25	0.03	0.8	234	22 ± 8
Al <sub>2</sub> O <sub>3</sub> - AluC	0.02	5.2	400	8 ± 2
SiO <sub>2</sub> - A130	0.02	0.18	70	16 ± 6

a Solid volume fraction [73]

b Nanoparticle work of adhesion [74]

c Nanoparticle Young's modulus [32, 75]

Kendall's model can estimate the elasticity of the highly porous sample to the right order of magnitude, which is known to be extremely challenging. The slight discrepancy between the theoretical and experimental Young's modulus values can be attributed to the partial plasticity of the agglomerates. In all three cases, the experimental value is lower than the theoretical one since plastic deformation based on aggregate rearrangements during agglomerate compression by the colloid is not accounted for in Kendall's model. This plasticity of the system must be too small (compared to the spring constant of the cantilever) for the experimental equipment and data analysis software to find the elastic Hertz model unsuited.

The parameters needed to calculate the elasticity for the different sample prepara-

tion methods are presumably known for the rough substrate and double sided tape, and assumed to be the same; however, the porosity of the pressed on glass sample is unknown. A porosity of  $91 \pm 5\%$  was back-calculated from the Kendall model for the  $\text{TiO}_2$  pressed on glass sample using the AFM measurements as the effective Young's modulus (Fig 3.6). This, means that even after the squeezing step, the pressed powder shows a highly porous morphology, which from the SEM images (Fig 3.3, C) seems appropriately described by the estimated value.

Other theoretical models to compute the Young's modulus were considered [30, 76–80]. Nevertheless, some of them include fitting parameters that require experimental data [34–37, 80], which defeats the purpose of the analytical calculation for this study; and those from Hashin and Hashin-Rosen [30] use as parameters properties of the porous material that are still unknown due to technical limitations similar to those encountered for the Young's modulus [81]. Alternative models listed in Choren et al.'s review [80] that only depend on agglomerate porosity and Young's modulus of the nonporous material, estimate moduli in the gigapascal (GPa) range (see Appendix), more than four orders of magnitude higher than the experimental values obtained from the AFM.

### 3.4. CONCLUSIONS

The research presented in this paper describes a method to experimentally determine the Young's modulus of structures with porosity higher than 90%. The focus of the study is on nanoparticle agglomerates, which are a few hundred micrometers in size and very fragile, formed due to strong attractive interactions among the primary particles. The experiments are done by AFM on five different samples including three materials ( $\text{Al}_2\text{O}_3$ ,  $\text{SiO}_2$ ,  $\text{TiO}_2$ ) using the double sided tape sample preparation method, and three sample preparation methods (pressed on glass, rough surface, double sided tape) for one of the nanopowders ( $\text{TiO}_2$ ). The results validate the applicability of Kendall et al. model to predict the elasticity of non-spherical highly porous structures. A more detailed analysis on the extrapolation of Kendall's model to low solid fractions and/or irregularly shaped particles will lead to a better understanding of the solid fraction's effect on the effective elasticity of porous structures. The proposed experimental technique can be used for validation of current or future models.

### REFERENCES

- [1] A. Fabre, S. Salameh, L. C. Ciacchi, M. T. Kreutzer, and J. R. van Ommen, *Contact mechanics of highly porous oxide nanoparticle agglomerates*, Journal of Nanoparticle Research **18**, 1 (2016).
- [2] M. H. Yuki Iwadate, *Prediction of agglomerate sizes in bubbling fluidized beds of group c powders*, Powder Technology **100**, 223 (1998).
- [3] D. G. Bika, M. Gentzler, and J. N. Michaels, *Mechanical properties of agglomerates*, Powder Technology **117**, 98 (2001).
- [4] W. Rong, A. E. Pelling, A. Ryan, J. K. Gimzewski, and S. K. Friedlander, *Complemen-*

- tary TEM and AFM force spectroscopy to characterize the nanomechanical properties of nanoparticle chain aggregates*, Nano Letters **4**, 2287 (2004).
- [5] F. Krus, H. Fissan, and A. Peled, *Synthesis of nanoparticles in the gas phase for electronic, optical and magnetic applications: a review*, Journal of Aerosol Science **29**, 511 (1998).
- [6] L. Madler, A. A. Lall, and S. K. Friedlander, *One-step aerosol synthesis of nanoparticle agglomerate films: simulation of film porosity and thickness*, Nanotechnology **17**, 4783 (2006).
- [7] L. K. Limbach, Y. C. Li, R. N. Grass, T. J. Brunner, M. A. Hintermann, M. Muller, D. Gunther, and W. J. Stark, *Oxide nanoparticle uptake in human lung fibroblasts: Effects of particle size, agglomeration, and diffusion at low concentrations*, Environmental Science & Technology **39**, 9370 (2005).
- [8] S. Matsuda, H. Hatano, T. Muramoto, and A. Tsutsumi, *Modeling for size reduction of agglomerates in nanoparticle fluidization*, Aiche Journal **50**, 2763 (2004).
- [9] J. Jung and D. Gidaspow, *Fluidization of nano-size particles*, Journal of Nanoparticle Research **4**, 483 (2002).
- [10] J. R. van Ommen, J. M. Valverde, and R. Pfeffer, *Fluidization of nanopowders: a review*, J Nanopart Res **14**, 737 (2012).
- [11] M. Dadkhah, M. Peglow, and E. Tsotsas, *Characterization of the internal morphology of agglomerates produced in a spray fluidized bed by x-ray tomography*, Powder Technology **228**, 349 (2012).
- [12] J. A. Quevedo, A. Omosebi, and R. Pfeffer, *Fluidization enhancement of agglomerates of metal oxide nanopowders by microjets*, AIChE Journal **56**, 1456 (2010).
- [13] J. Shabanian, R. Jafari, and J. Chaouki, *Fluidization of ultrafine powders*, Int Rev Chem Eng **4**, 16 (2012).
- [14] F. Parveen, F. Berruti, C. Briens, and J. McMillan, *Effect of fluidized bed particle properties and agglomerate shape on the stability of agglomerates in a fluidized bed*, Powder Technology **237**, 46 (2013).
- [15] H. L. Tao Zhou, *Estimation of agglomerate size for cohesive particles during fluidization*, Powder Technology **101**, 57 (1999).
- [16] A. Khadilkar, P. L. Rozelle, and S. V. Pisupati, *Models of agglomerate growth in fluidized bed reactors: Critical review, status and applications*, Powder Technology **264**, 216 (2014).
- [17] Y. Liang, M. Ozawa, and A. Krueger, *A general procedure to functionalize agglomerating nanoparticles demonstrated on nanodiamond*, ACS Nano **3**, 2288 (2009).
- [18] S. Salameh, J. Schneider, and J. e. a. Laube, *Adhesion mechanisms of the contact interface of tio2 nanoparticles in films and aggregates*, Langmuir **28**, 11457 (2012).

- [19] W. Yao, G. Guangsheng, W. Fei, and W. Jun, *Fluidization and agglomerate structure of SiO<sub>2</sub> nanoparticles*, Powder Technol **124**, 152 (2002).
- [20] L. de Martin, W. G. Bouwman, and J. R. van Ommen, *Multidimensional nature of fluidized nanoparticle agglomerates*, Langmuir **30**, 12696 (2014).
- [21] D. Hu, J. Zhuang, and M. Ding, *A review of studies on the granular agglomeration mechanisms and anti-agglomeration methods*, Key Engineering Materials **501**, 515 (2012).
- [22] J. Laube, S. Salameh, M. Kappl, L. Madler, and L. C. Ciacchi, *Contact forces between TiO<sub>2</sub> nanoparticles governed by an interplay of adsorbed water layers and roughness*, Langmuir **31**, 11288 (2015).
- [23] A. Castellanos, *The relationship between attractive interparticle forces and bulk behaviour in dry and uncharged fine powders*, Advances in Physics **54**, 263 (2005).
- [24] L. F. Hakim, J. L. Portman, M. D. Casper, and A. W. Weimer, *Aggregation behavior of nanoparticles in fluidized beds*, Powder Technology **160**, 149 (2005).
- [25] J. P. K. Seville, C. D. Willett, and P. C. Knight, *Interparticle forces in fluidisation: a review*, Powder Technology **113**, 261 (2000).
- [26] J. R. van Ommen, *Manufacturing core-shell nanoparticles by atomic layer deposition in a fluidized bed*, in *International Symposium on Chemical Reaction Engineering* (2012).
- [27] J. A. Quevedo and R. Pfeffer, *In situ measurements of gas fluidized nanoagglomerates*, Industrial and Engineering Chemistry Research **49**, 5263 (2010).
- [28] W. Yan, S. Li, Y. Zhang, Q. Yao, and S. D. Tse, *Effects of dipole moment and temperature on the interaction dynamics of titania nanoparticles during agglomeration*, The Journal of Physical Chemistry C **114**, 10755 (2010).
- [29] H. M. Wyss, T. Franke, E. Mele, and D. A. Weitz, *Capillary micromechanics: Measuring the elasticity of microscopic soft objects*, Soft Matter **6**, 4550 (2010).
- [30] H. N. Yoshimura, A. L. Molisani, N. E. Narita, P. F. Cesar, and H. Goldenstein, *Porosity dependence of elastic constants in aluminum nitride ceramics*, Materials Research **10**, 127 (2007).
- [31] R. B. Schwarz, K. Khachatryan, and E. R. Weber, *Elastic moduli of gallium nitride*, Applied Physics Letters **70**, 1122 (1997).
- [32] K. Kendall, N. M. Alford, and J. D. Birchall, *Elasticity of particle assemblies as a measure of the surface energy of solids*, Proceedings of the Royal Society of London A: Mathematical, Physical and Engineering Sciences **412**, 269 (1987).
- [33] K. Kendall and T. P. Weihs, *Adhesion of nanoparticles within spray dried agglomerates*, Journal of Physics D: Applied Physics **25**, A3 (1992).



- [34] D. P. H. Hasselman, *On the porosity dependence of the elastic moduli of polycrystalline refractory materials*, Journal of the American Ceramic Society **45**, 452 (1962).
- [35] J. Wang, *Young's modulus of porous materials*, Journal of Materials Science **19**, 809 (1984).
- [36] R. B. Martin and R. R. Haynes, *Confirmation of theoretical relation between stiffness and porosity in ceramics*, Journal of the American Ceramic Society **54**, 410 (1971).
- [37] K. Phani and S. Niyogi, *Elastic modulus-porosity relationship for  $Si_3N_4$* , Journal of Materials Science Letters **6**, 511 (1987).
- [38] P. Pimpang, A. S. Zoolfakar, D. Wongratanaphisan, A. Gardchareon, E. P. Nguyen, S. Zhuiykov, S. Choopun, and K. Kalantar-zadeh, *Atomic force microscopy adhesion mapping: Revealing assembly process in inorganic systems*, The Journal of Physical Chemistry C **117**, 19984 (2013).
- [39] I. U. Vakarelski and K. Higashitani, *Single-nanoparticle-terminated tips for scanning probe microscopy*, Langmuir **22**, 2931 (2006).
- [40] V. Barcons, A. Verdaguer, J. Font, M. Chiesa, and S. Santos, *Nanoscale capillary interactions in dynamic atomic force microscopy*, The Journal of Physical Chemistry C **116**, 7757 (2012).
- [41] K. P. Sigdel, J. S. Grayer, and G. M. King, *Three-dimensional atomic force microscopy: Interaction force vector by direct observation of tip trajectory*, Nano Letters **13**, 5106 (2013).
- [42] S. Salameh, R. Scholz, J. W. Seo, and L. Madler, *Contact behavior of size fractionated  $TiO_2$  nanoparticle agglomerates and aggregates*, Powder Technology **256**, 345 (2014).
- [43] R. L. Stiles, K. A. Willets, L. J. Sherry, J. M. Roden, and R. P. Van Duyne, *Investigating tip-nanoparticle interactions in spatially correlated total internal reflection plasmon spectroscopy and atomic force microscopy*, Journal of Physical Chemistry C **112**, 11696 (2008).
- [44] M. Farshchi-Tabrizi, M. Kappel, Y. J. Cheng, J. Gutmann, and H. J. Butt, *On the adhesion between fine particles and nanocontacts: An atomic force microscope study*, Langmuir **22**, 2171 (2006).
- [45] K. Li and Y. Chen, *Examination of nanoparticle-DNA binding characteristics using single-molecule imaging atomic force microscopy*, The Journal of Physical Chemistry C **118**, 13876 (2014).
- [46] G. B. Webber, R. Manica, S. A. Edwards, S. L. Carnie, G. W. Stevens, F. Grieser, R. Dagastine, , and D. Y. Chan, *Dynamic forces between a moving particle and a deformable drop*, The Journal of Physical Chemistry C **112**, 567 (2008).

- [47] I. Tanabe and T. Tatsuma, *Size- and shape-controlled electrochemical deposition of metal nanoparticles by tapping mode atomic force microscopy*, The Journal of Physical Chemistry C **116**, 3995 (2012).
- [48] A. Engler, L. Richert, J. Wong, C. Picart, and D. D. E., *Surface probe measurements of the elasticity of sectioned tissue: thin gels and polyelectrolyte multilayer films: correlations between substrate stiffness and cell adhesion*, Surface Science **570**, 142 (2004).
- [49] L. Picas, P.-E. Milhiet, and J. Hernandez-Borrell, *Atomic force microscopy: A versatile tool to probe the physical and chemical properties of supported membranes at the nanoscale*, Chemistry and physics of lipids **165**, 845 (2012).
- [50] D. Xu, K. M. Liechti, and K. Ravi-Chandar, *On the modified Tabor parameter for the JKR-DMT transition in the presence of a liquid meniscus*, Colloid and Interface Science **315**, 772 (2007).
- [51] D. C. Lin, E. K. Dimitriadis, and F. Horkay, *Robust strategies for automated AFM force curve analysis-II: Adhesion-influenced indentation of soft, elastic materials*, Journal of Biomechanical Engineering **129**, 904 (2007).
- [52] W. Zheng and Z. Ya-Pu, *Experimental investigation of the velocity effect on adhesion forces with an atomic force microscope*, Chinese Physics Letters **21**, 616 (2004).
- [53] F. Landolsi, F. H. Ghorbel, and J. B. Dabney, *Adhesion and friction coupling in atomic force microscope-based nanopushing*, Journal of Dynamic Systems Measurement and Control-Transactions of the Asme **135** (2013).
- [54] D. Fotiadis, S. Scheuring, S. A. Müller, A. Engel, and D. J. Müller, *Imaging and manipulation of biological structures with the AFM*, Micron **33**, 385 (2002).
- [55] F. Rico, P. Roca-Cusachs, N. Gavara, R. Farré, M. Rotger, and D. Navajas, *Probing mechanical properties of living cells by atomic force microscopy with blunted pyramidal cantilever tips*, Phys. Rev. E **72**, 021914 (2005).
- [56] J. M. B. K. Emiliós K Dimitriadis, Ferenc Horkay and R. S. Chadwick, *Determination of elastic moduli of thin layers of soft material using the atomic force microscope*. Biophysical Journal **82**, 2798 (2002).
- [57] S. O. Schopf, S. Salameh, and L. Madler, *Transfer of highly porous nanoparticle layers to various substrates through mechanical compression*, Nanoscale **5**, 3764 (2013).
- [58] H. J. Butt, B. Cappella, and M. Kappl, *Force measurements with the atomic force microscope: Technique, interpretation and applications*, Surface Science Reports **59**, 1 (2005).
- [59] A. Vinckier and G. Semenza, *Measuring elasticity of biological materials by atomic force microscopy*, FEBS Letters **430**, 12 (1998).

- [60] C. Roduit, S. Sekatski, G. Dietler, S. Catsicas, F. Lafont, and S. Kasas, *Stiffness tomography by atomic force microscopy*, *Biophysical Journal* **97**, 674 (2009).
- [61] M. Radmacher, M. Fritz, C. Kacher, J. Cleveland, and P. Hansma, *Measuring the viscoelastic properties of human platelets with the atomic force microscope*, *Biophysical Journal* **70**, 556 (1996).
- [62] J. Hutter and J. Bechhoefer, *Calibration of atomic-force microscope tips*, *Review of Scientific Instruments* **64**, 1868 (1993).
- [63] N. A. Burnham, X. Chen, C. S. Hodges, G. A. Matei, E. J. Thoreson, C. J. Roberts, M. C. Davies, and S. J. B. Tendler, *Comparison of calibration methods for atomic-force microscopy cantilevers*, *Nanotechnology* **14**, 1 (2003).
- [64] H. Hertz, *Ueber die berührung fester elastischer körper*, *Journal für die reine und angewandte Mathematik* **92**, 156 (1881).
- [65] A. D. R. K. L. Johnson, K. Kendall, *Surface energy and the contact of elastic solids*, *Proceedings of the Royal Society of London Series A* **324**, 301 (1971).
- [66] B. Derjaguin, V. Muller, and Y. Toporov, *Effect of contact deformations on the adhesion of particles*, *Journal of Colloid and Interface Science* **53**, 314 (1975).
- [67] D. Maugis, *Adhesion of spheres: The jkr-dmt transition using a dugdale model*, *Journal of Colloid and Interface Science* **150**, 243 (1992).
- [68] *Determining the elastic modulus of biological samples using atomic force microscopy*, JPK Instruments, [www.jpk.com](http://www.jpk.com).
- [69] C.-J. Tsai, D. Y. H. Pui, and B. Y. H. Liu, *Elastic flattening and particle adhesion*, *Aerosol Science and Technology* **15**, 239 (1991).
- [70] L. Bergstrom, *Hamaker constants of inorganic materials*, *Advances in Colloid and Interface Science* **70**, 125 (1997).
- [71] L. D. Norman, *Computer simulation of particulate systems*, US Bureau of Mines **Bullerin 658** (1971).
- [72] J. K. Mackenzie, *The elastic constants of a solid containing spherical holes*, *Proceedings of the Physical Society. Section B* **63**, 2 (1950).
- [73] M. Tahmasebpour, L. de Martín, M. Talebi, N. Mostoufi, and J. R. van Ommen, *The role of the hydrogen bond in dense nanoparticle-gas suspensions*, *Phys Chem Chem Phys* **15**, 5788 (2013).
- [74] A. Navrotsky, *Energetics of nanoparticle oxides: interplay between surface energy and polymorphism*, *Geochemical Transactions* **4**, 34 (2003).
- [75] B. Chen, H. Zhang, K. A. Dunphy-Guzman, D. Spagnoli, M. B. Kruger, D. V. S. Muthu, M. Kunz, S. Fakra, J. Z. Hu, Q. Z. Guo, and J. F. Banfield, *Size-dependent elasticity of nanocrystalline titania*, *Phys. Rev. B* **79**, 125406 (2009).

- [76] M. U. S. Y. Jun Adachi, Ken Kurosaki, *Porosity influence on the mechanical properties of polycrystalline zirconium nitride ceramics*, Journal of Nuclear Materials **358**, 106 (2006).
- [77] J. P. S. A. S. Wagh, R. B. Poeppel, *Open pore description of mechanical properties of ceramics*, Journal of Materials Science **26**, 3862 (1991).
- [78] E. G. Willi Pabst and G. Ticha, *Elasticity of porous ceramics - a critical study of modulus-porosity relations*, Journal of the European Ceramic Society **26**, 1085 (2006).
- [79] M. Kupkova, *Porosity dependence of material elastic moduli*, Journal of Materials Science **28**, 5265 (1993).
- [80] J. Choren, S. Heinrich, and M. Silver-Thorn, *Young's modulus and volume porosity relationships for additive manufacturing applications*, Journal of Materials Science **48**, 5103 (2013).
- [81] J. Kovacik, *Correlation between shear modulus and porosity in porous materials*, Journal of Materials Science Letters **20**, 1953 (2001).

## APPENDIX 3.A

## CANTILEVER WITH COLLOID

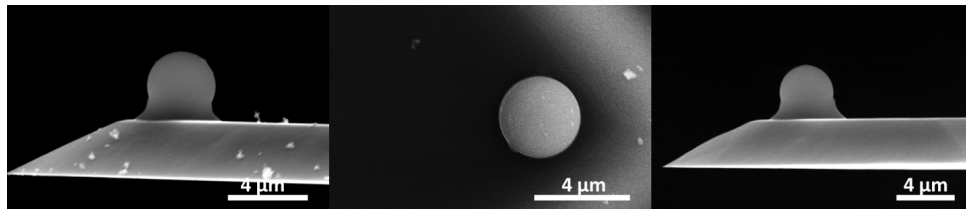


Figure 3.9: SEM images of used cantilevers. From left to right, on rough substrate, double sided tape, and pressed on glass, respectively. The cantilevers were bought from sQube (CP-FM-SiO-B) with a glass colloid of  $3.5 \mu\text{m}$  in diameter attached to it.

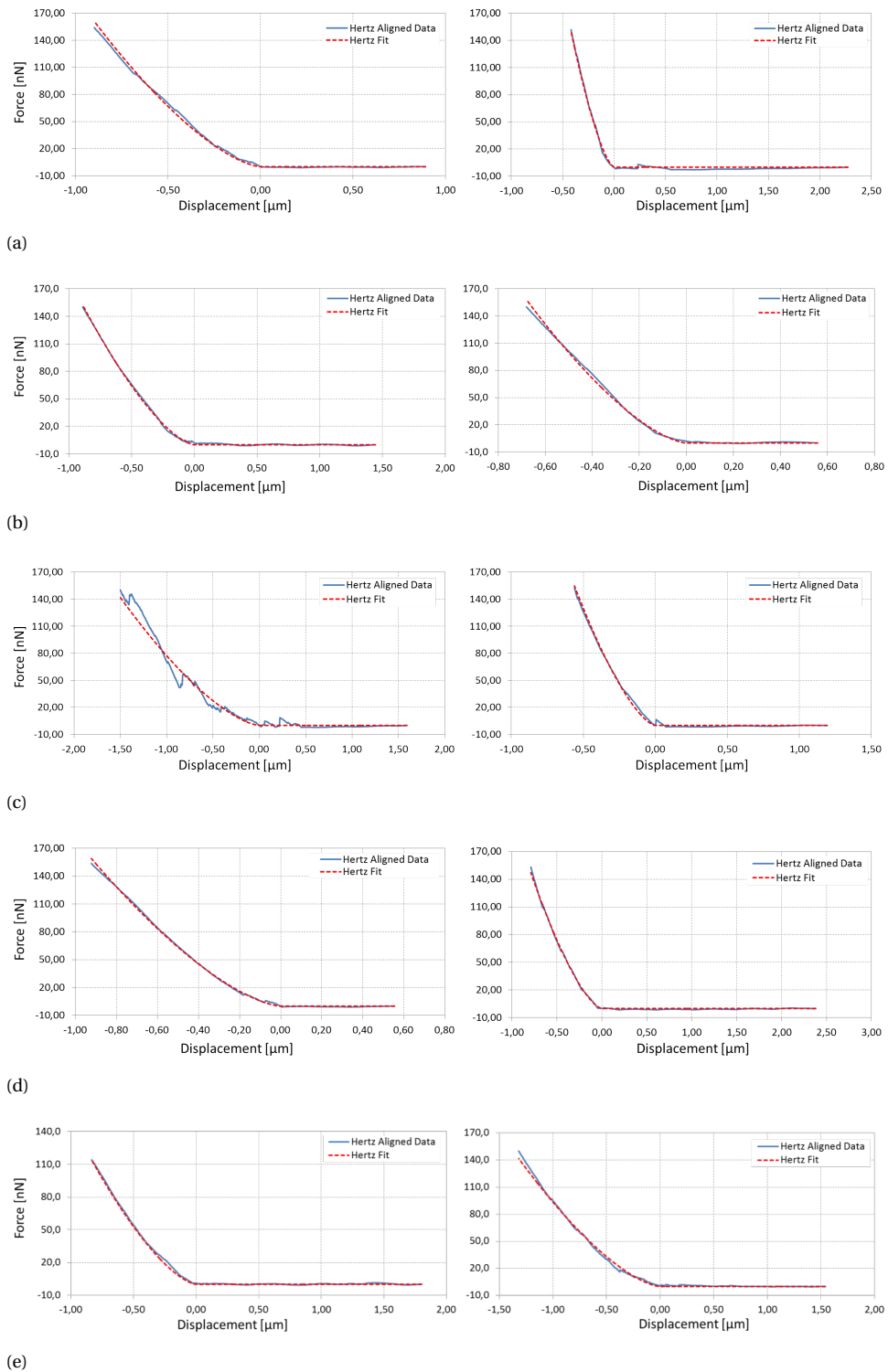


Figure 3.10: Hertz model fitting of multiple force curves obtained from AFM measurements of titania-TiO<sub>2</sub> (a-b), alumina-Al<sub>2</sub>O<sub>3</sub> (c-d), and silica-SiO<sub>2</sub> (e) samples on double-sided-tape.

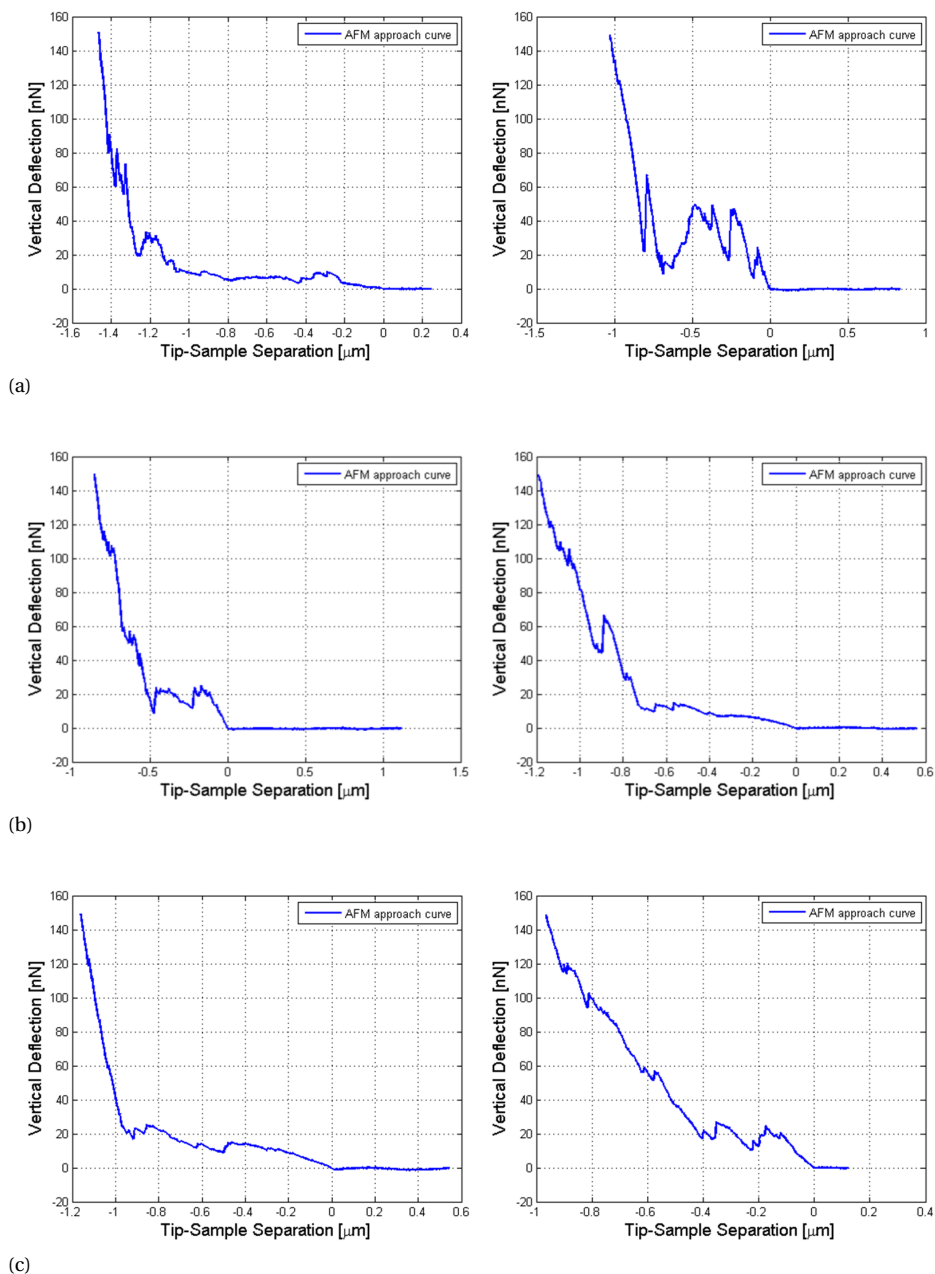


Figure 3.11: Example of curves not considered for measurement, but saved for further analysis of the nanopowder film morphology. Curves show particle rearrangement, not suitable for Hertz fitting.

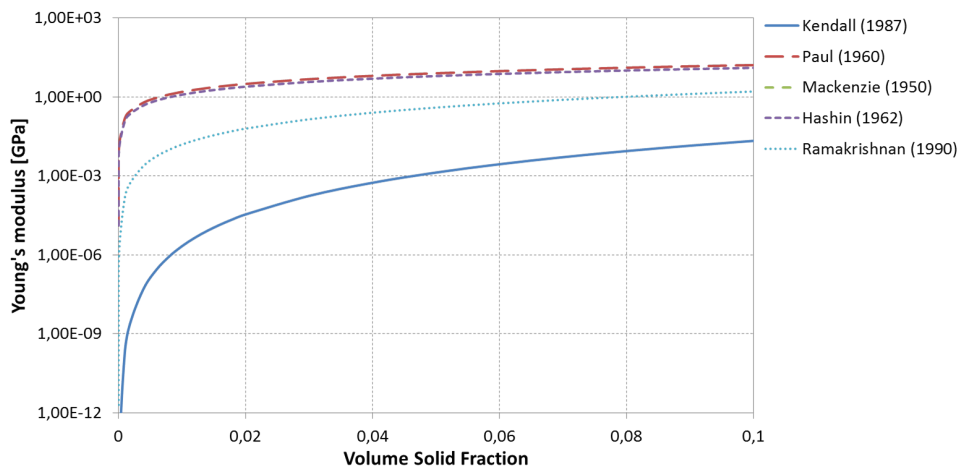


Figure 3.12: Comparison of models that estimate the elasticity of porous structures based on porosity, without fitting parameters. Properties of  $\text{TiO}_2$  (P25) were used for the calculations.





# 4

## ENTRAINMENT OF NANOSIZED CLUSTERS FROM A NANOPOWDER FLUIDIZED BED

The release of nanosized particles from fluidized beds of ceramic oxide nanopowders, namely  $\text{TiO}_2$  (P25),  $\text{Al}_2\text{O}_3$  (AluC) and  $\text{SiO}_2$  (A130) has been assessed for the first time. Previous models and experiments for processing engineered nanoparticles (ENP) using fluidized beds reported only the formation of micron-sized cluster agglomerates in the gas phase. In this work, aerosol spectrometry techniques such as scanning mobility particle sizing (SMPS) and optical particle counting (OPC) have been combined with powder technologies, such as the borescope high-speed camera system, to determine the particle size distribution from 5 nm to 1 mm above a fluidized bed. Furthermore, the morphology of nanoparticulate aerosol at different locations in the bed was determined by offline electron microscopy. The results demonstrate that free nano and micron-sized particles are released in significant quantities from fluidized beds. The structures found above the bed are also expected to be present within fluidized beds. These findings urge a revision of existing nanoparticle fluidization models, and ask for improved safety and control measures in reactors for gas-phase ENP processing to avoid or reduce nanoparticle release.

---

Parts of this chapter have been published in 000, 000 (2016) [].

## 4.1. INTRODUCTION

Nanoscale products continue to grow in number and variety, covering a wide array of applications in the latter years [2–10], including polymer composites, energy harvesting, catalysis, textiles, medicine, and sensors, to name a few. Worldwide revenue from nano-enabled products increased from \$339 billion in 2012 to \$731 billion in 2015, and is estimated to exceed the \$1 trillion mark in 2018 [11].

In terms of nanomaterial processing, engineered nanoparticles (ENPs) have been produced in both liquid and gas phase usually at small scale, and in principle with a reduced impact in human health or the environment [12–14]. However, since the demand for nanomaterials continues to increase at an outstanding pace driven by the number of applications, advanced scaled up processes for the production of these ENP become essential [15, 16]. In this scenario, gas phase processing is a promising tool, capable of large throughput that take advantage of fast kinetics at high temperatures [17–19]. Gas phase processes are able to generate ENP-loaded gas streams at high concentrations, often over  $10^6$  p/cm<sup>3</sup>, which are eventually collected using filters or wet scrubbers [20, 21]. Yet, together with large yield capabilities, gas-phase methods have shown to be liable to produce by-side ENP aerosols during handling, reactor loading, or maintenance operations [22–24]. This has caused concern given the potentially hazardous characteristics of ENP aerosols for human health [25, 26] and the natural environment [27, 28].

Fluidized bed processing of nanoscale materials is an emerging alternative of huge potential for gas phase processing, in view of advantages such as no solvent waste, clean particle surface, potential scalability, large gas-solid contact area, and suitability for continuous processing [29–31]. However, regarding nanoparticle emission, it has been generally assumed that nanoparticles fluidize as micron-sized clusters called agglomerates, due to strong van der Waals forces, capillary bridges, electrostatic interactions [32] and hydrogen bond formation [33, 34]; thus, with little or no free nanostructure content. Different gas-solid interactions have been identified during fluidization of nano-sized solid powders beyond the conventional Geldart's classification [35]. Initially, uniform non-bubbling low-density agglomerate particle fluidization (APF) was observed upon increasing fluidization velocity to produce an enhanced high solid-fluid contact, leading to particles with homogeneous size distributions [36, 37]. Non-uniform agglomerate bubbling fluidization (ABF) has been identified when increasing the fluidization velocity even more, which is described by plugs, channeling, and a bubble-bursting splash zone in the fluidized bed [37, 38]. The dynamics of each type of fluidization vary, affecting the morphology and size of the fluidized nanoparticle agglomerates. It has been shown that agglomerate size can be determined from interparticle forces, which depend on the properties of the nanopowders, bed geometry, and fluidization gas, along with the processing time. The mean fluidized agglomerate size is commonly predicted by force and energy balances [39, 40], or from the pressure drop and bed expansion using the Richardson-Zaki equation [40] giving values only in the micrometer range.

As explained previously, the presence of nano-sized particulate matter in the gas-phase has been generally ignored. Certain experiments visualizing complex fluidized agglomerates using a high-speed camera have been performed [40–42]; however, the camera resolution, which goes down to a couple micrometers per pixel, did not allow the detection of smaller structures. To the best of our knowledge, *in situ* measurements

of the size distribution in or above fluidized beds going through the whole nano to micron size range have not been done before. For the first time, the present work quantitatively analyzes the particle size distribution within and above the fluidized bed in the so-called freeboard region. To this end, three different nanoparticulate beds were designed using  $\text{SiO}_2$ , which shows an APF behavior, and  $\text{TiO}_2$  and  $\text{Al}_2\text{O}_3$ , which exhibit ABF behavior [43]. The particle size distribution was determined using aerosol spectroscopy techniques, namely scanning mobility particle sizing (SMPS) and optical particle counting (OPC) for online monitoring of airborne matter in the range from 5 nm to 20  $\mu\text{m}$ . For sizes above 20  $\mu\text{m}$ , an *in situ* visualization technique involving a borescope and high-speed camera was employed [44, 45]. Finally, the morphology and agglomeration state of the nanopowders during fluidization was analyzed using electron microscopy techniques on samples captured both within and over the fluidized bed. Results have been expressed in terms of the variation of the size distributions of nano and micron-sized particles in the freeboard at different vertical positions, as well as a function of the fluidization time for the three oxide nanopowders. The results are crucial to understand fluidization at the nanoscale, and to raise consciousness on the generation of nanoparticulate aerosols during fluidized bed processing of nanoscale matter.

## 4.2. EXPERIMENTAL SECTION

### 4.2.1. POWDER CHARACTERIZATION

Hydrophilic  $\text{Al}_2\text{O}_3$  (AluC),  $\text{SiO}_2$  (A130) and  $\text{TiO}_2$  (P25) were supplied by Evonik (see Appendix 4.A for details on material specifications). Nanoparticle sizes were determined using TEM, counting over 250 particles per sample with the open-source software ImageJ. Due to the production method, most nanoparticles were found to be sintered forming open-chain aggregates of a few hundreds nanometers. While in storage, aggregates form larger clusters called agglomerates that can restrain powder fluidization [46]. To avoid this, all powders were sieved to remove particles over 450  $\mu\text{m}$  before every experiment.

### 4.2.2. EXPERIMENTAL SET UP

A glass column with a 45 x 45 mm square cross-sectional area and height of 150 mm (see Figure 4.1) was designed for nanoparticle fluidization. One of the sidewalls had seven evenly distributed 6-mm measuring ports. Nanopowders were fluidized with pure dry  $\text{N}_2$  at 0.074 m/s entering from the bottom through a porous distributor plate. In order to keep a constant bed expansion and overall particle concentration at the measuring ports for every experiment, 1.2 g of  $\text{SiO}_2$ , 0.5 g of  $\text{Al}_2\text{O}_3$ , and 2 g of  $\text{TiO}_2$  were alternatively placed in the column providing initial bed heights of 30 mm, 10 mm, and 20 mm, respectively. Finally, the gas leaving the fluidization column was passed through a water bubbler and HEPA filter to retain any entrained powder.

The concentration and particle size distribution in the range from 5 to 500 nm of the powder suspended in the freeboard was measured with a NanoParticle Spectrometer (NPS, Nano-IDTM NPS500, Particle Measuring Systems, Boulder CO) at a sample flow rate of 0.2 l/min. Particle concentration and size distribution in the freeboard within the range 300 nm - 20  $\mu\text{m}$  were quantified by an optical particle counter (OPC, model #1.108

Grimm Aerosol Technik, Ainring, Germany) at a flow rate of 1.2 l/min. Aerosol sampling from the freeboard using NPS and OPC was performed through the top four openings (H7-H4) with a 400-mm flexible conducting pipe with inner diameter of 6.35 mm (1/4"), kept as straight as possible to prevent morphological alteration of the structures during sampling (Figure 4.1). The equipment and pipes were frequently cleaned to prevent clogging.

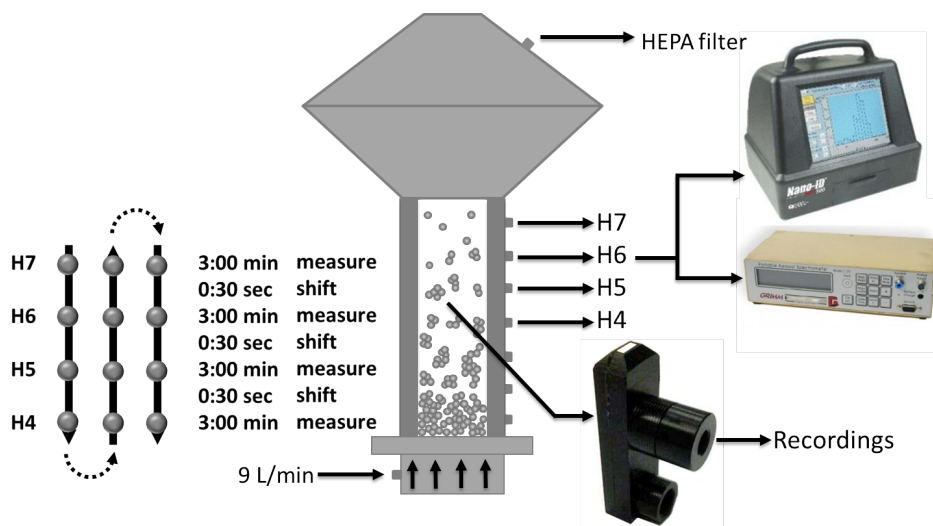


Figure 4.1: Schematic representation of the experimental set up. Sieved nanopowder is placed in the column. Gas is introduced through the bottom of the column suspending the powder, which is sampled through the wall openings and measured by aerosol spectrometers (NPS and OPC), or recorded using the settling tube technique with the borescope and high speed camera system. The measurement order and timing used for the OPC are shown on the left side of the figure.

Agglomerates and particles with sizes above  $20\ \mu\text{m}$  were analyzed using the settling tube technique [44]. This *in situ* method consists of a small rectangular black box placed within the fluidized bed at a set position. The settling tube has a  $1 \times 2\text{-mm}$  rectangular inlet at the top to catch falling fluidized powder, and two circular openings on the side, one on top for the borescope-camera recording system and one at the bottom for a secondary gas flow to empty the tube before the recordings (Figure 4.1). Videos were taken at 800 fps through a 4-mm circular window. The videos were analyzed using an in-home Matlab code that recognizes, tracks, and filters the recorded agglomerates.

To test particle size distributions at different heights and times with the NPS and OPC, the sampling pipe was periodically shifted upwards and downwards among the top four height positions (H4 to H7) (see Figure 4.1). Due to the homogeneous fluidization of  $\text{SiO}_2$ , the sampling ports were within the fluidized bed, whereas for  $\text{Al}_2\text{O}_3$  and  $\text{TiO}_2$  they were right above the bed; and therefore, the freeboard was sampled. Consecutive experiments of 120 and 45 min were done with each powder at every sampling port while extracting samples with the NPS and OPC during fluidization. The settling tube technique was only used for time studies and it was therefore placed at the same height

(H4). Videos were taken right at the start of fluidization and after every 10 min until reaching 1 h.

#### 4.2.3. MICROSCOPY ANALYSIS

Aerosol samples in the freeboard were collected for both SEM and TEM analysis of the micron and nanostructures produced upon fluidization. Two sampling techniques were alternatively used for obtaining SEM specimens. One of the procedures consisted in extracting the aerosol phase from the freeboard at 1.2 l/min for 15 s through a 50-nm mesh cellulose ester filter (model VMWP04700, Merck-Millipore, Billerica MA) placed inside a stainless steel in-line 47-mm filter holder (model 16254, Sartorius, Göttingen, Germany). The second procedure involved a double-sided carbon tape attached to a microscope glass slide that was directly exposed to the H5 sampling port for 5 s at 5 mm from the opening. Finally, TEM samples were taken on lacey copper grids located in a stainless steel aerosol mini-sampler designed at the University of Zaragoza [23, 47] at 1.2 l/min for 5 s (see Appendix).

### 4.3. RESULTS AND DISCUSSION

#### 4.3.1. POWDER CHARACTERIZATION

The fluidization of nanoparticles started with a powder splash as the gas flow rate increased to the desired value, expelling visible particles of about hundreds of micrometers that slowly fell back to the bed. The height effect on the powder concentration and size distribution in the freeboard was minimal. The size distribution trend in the aerosol phase was similar for all three powders and heights. Furthermore, the total amount of particles encountered throughout the multiple vertical levels was generally in the same order of magnitude (see Table 4.1). Since approximately the same size distribution and overall particle count for nano and micron-sized structures were found among H4, H5, H6 and H7, it could be concluded that there was close to uniform particle distribution within the studied volume. The geometric mean diameter (GMD) calculated by the NPS (5 to 500 nm) was also consistent among the four heights tested, with average values of  $55 \pm 2$  nm for  $\text{TiO}_2$ ,  $40 \pm 2$  nm for  $\text{Al}_2\text{O}_3$ , and  $125 \pm 2$  nm for  $\text{SiO}_2$ . The OPC measurements also showed consistent particle concentration among the different freeboard heights in the micro range (0.3 to 20  $\mu\text{m}$ ).

Table 4.1: Total aerosol concentration ( $\# \text{L}^{-1}$ )  $\times 10^6$  and geometric mean diameter of structures in the 5 to 500 nm size range present at the different freeboard heights for all powders as obtained directly from the NPS.

	Concentration ( $\# \text{L}^{-1}$ ) $\times 10^6$					GMD (nm)
	H7	H6	H5	H4		
P25	6.4	7.7	9.3	7.8		$54.7 \pm 1.9$
AluC	3.5	4.4	3.6	3.2		$40.4 \pm 1.7$
A130	4.7	3.6	3.1	3.3		$125.0 \pm 1.8$

For  $\text{TiO}_2$  and  $\text{Al}_2\text{O}_3$ , the particle concentration detected by the OPC was always in the order of millions, similar to that found by the NPS. However, the size range covered by the OPC is about 40 times wider than that of the NPS, meaning that freeboard aerosol

particles in the nano range significantly outnumbered those in the micro range. The case was more remarkable for  $\text{SiO}_2$  since aerosol concentration of micron-sized particles was even one order of magnitude smaller than that in the size range from 5 to 500 nm. Data from the OPC displayed peculiar, but consistent, particle size distribution profiles, showing that main particle contributions occurred for sizes smaller than  $2 \mu\text{m}$ . For larger particle sizes, all powders showed a peak at about  $6 \mu\text{m}$ , slightly more noticeable for  $\text{TiO}_2$  (Figure 4.2).

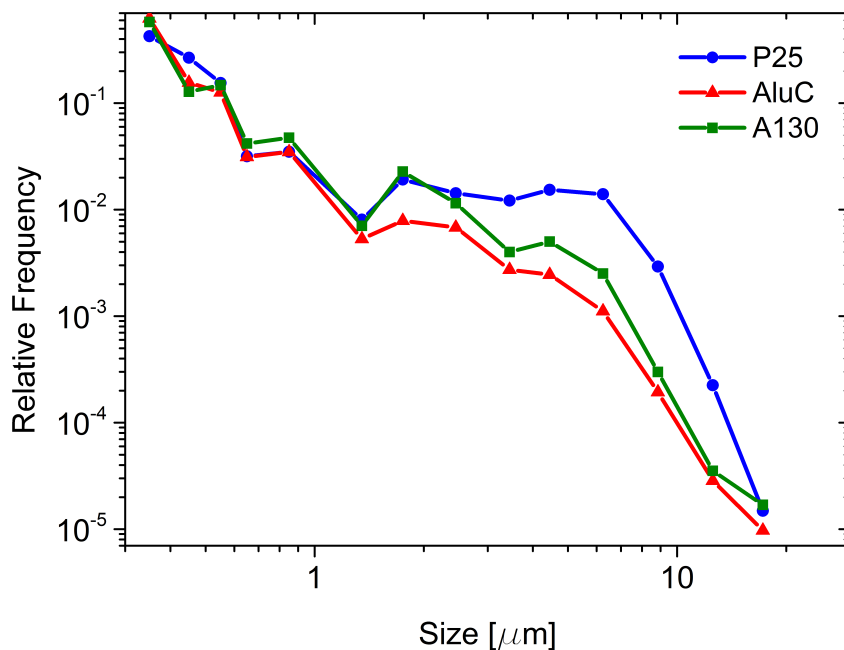


Figure 4.2: Aerosol particle size distributions of the fluidized nanopowder measured after reaching the steady state. Measurements were obtained from the OPC and normalized by the total number of particles per micron.

Regarding the fluidization time, every material showed different behaviors while attaining the steady state.  $\text{TiO}_2$  was the most consistent on particle concentration over time, dropping to  $1/4$  of the original amount after 120 min. The concentration of  $\text{Al}_2\text{O}_3$  and  $\text{SiO}_2$  particles rapidly dropped after 30 min to less than  $1/5$ , reaching an amount of less than  $1/10$  of the initial concentration after 120 min (Figure 4.3). During the experiments, the non-uniform agglomerate bubbling fluidization (ABF) behavior of  $\text{TiO}_2$  was obvious, with a few visible particles above the splash zone. Even though  $\text{Al}_2\text{O}_3$  also showed the ABF behavior, a more uniform fluidization with fewer bubbles than with  $\text{TiO}_2$  was detected. As the only APF powder studied,  $\text{SiO}_2$  showed an homogeneous fluidization with a barely perceptible density gradient along the bed. At the end of the experiments, a significant quantity of  $\text{Al}_2\text{O}_3$  and  $\text{SiO}_2$  was lost by elutriation upon fluidization, showing over 30% of mass loss, causing the dramatic drop of the particle count. Additionally, only the agglomerate size distribution of  $\text{TiO}_2$  changed as it approached the

steady state, losing the peak at  $6\ \mu\text{m}$  (Figure 4.3).

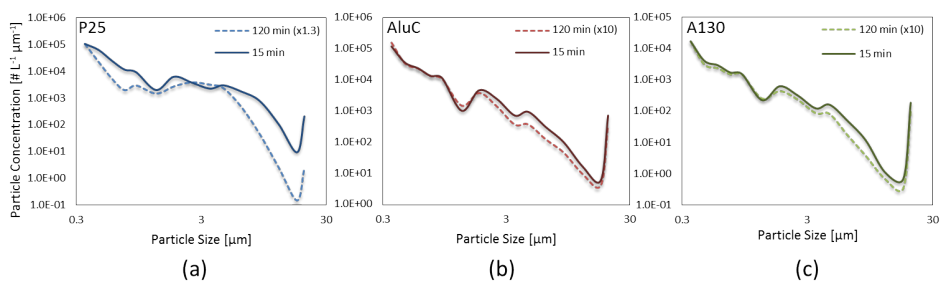


Figure 4.3: Particle size distributions in the freeboard of (a) TiO<sub>2</sub> and (b) Al<sub>2</sub>O<sub>3</sub>, and in the fluidized bed of (c) SiO<sub>2</sub> after 15 min and 120 min. The particle concentration of Al<sub>2</sub>O<sub>3</sub> and SiO<sub>2</sub> decreased to 1/10, while that of TiO<sub>2</sub> decreased to 10/13. Main aerosol solid concentrations were in the order of 10<sup>5</sup> part/l for TiO<sub>2</sub> and Al<sub>2</sub>O<sub>3</sub>, and of 10<sup>4</sup> part/l for SiO<sub>2</sub>

Electron microscopy analysis confirmed the particle size distributions found with NPS and OPC. Indeed, TEM images showed highly-porous nanoparticle clusters in the nano range for all the powders in agreement with the aerosol measuring data. The individual clusters were distinguishable from the images (Figure 4.4 (a-c)), though higher magnification showed chains of only a few nanoparticles connecting some of the clusters, raising questions about agglomerate recognition as one or two for such a scenario. SEM images of the filters showed the loose arrangement of the chain-like aggregates into larger structures. The filters had a predominant concentration of agglomerates smaller than  $10\ \mu\text{m}$ , with detached nanostructures spread on the surface, which could be fragments of the larger bodies or structures extracted directly from the bed (Figure 4.4 (d-f)). Carbon tape samples of TiO<sub>2</sub> showed a larger amount of complex agglomerates around  $100\ \mu\text{m}$  in size compared to the other powders, and these agglomerates were highly porous, formed by simple agglomerates of less than  $20\ \mu\text{m}$  (Figure 4.4 (g)).



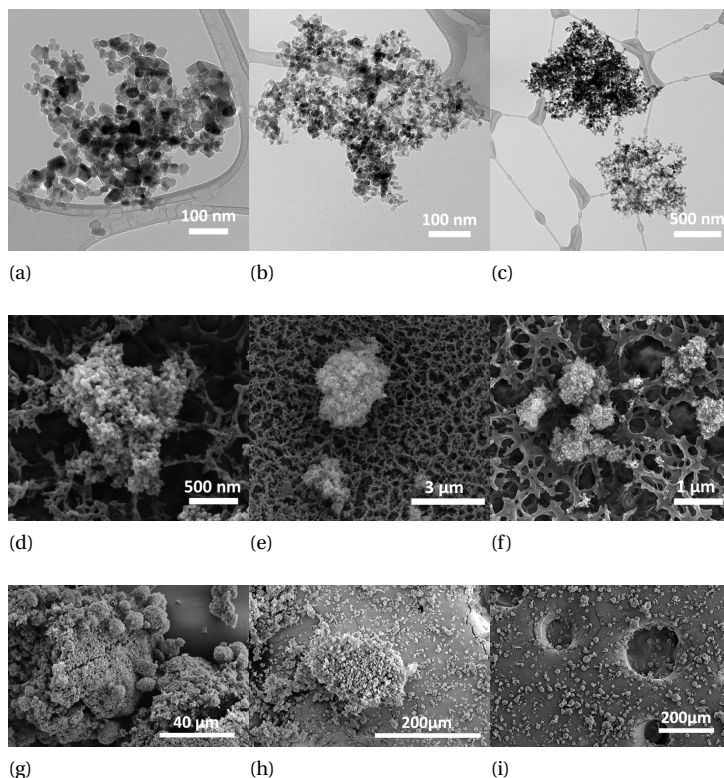


Figure 4.4: TEM (a-c) and SEM (d-i) pictures of fluidized agglomerates captured on (a-c) a copper grid, (d-f) filter, or (g-i) carbon tape. a) P25 sample with clusters smaller than  $1 \mu\text{m}$ . b) AluC cluster of 550 nm. c) A130 micron size agglomerates connected by a chain of primary particles. d-e) A130 fluffy agglomerates attached to the filter. f) AluC sample of  $<1 \mu\text{m}$  clusters grasped by the filter. g) P25 complex agglomerates formed and decorated by simple agglomerates. h) AluC fluidized powder sample showing a complex agglomerate surrounded by simple agglomerates. i) A130 sample with fluidized structures of no more than  $40 \mu\text{m}$  each.

Image analysis of the  $\text{TiO}_2$  filter samples revealed an agglomerate size distribution with peaks roughly at  $1 \mu\text{m}$ ,  $6 \mu\text{m}$  and  $8 \mu\text{m}$  (Figure 4.5). The images from the  $\text{Al}_2\text{O}_3$  carbon tape samples showed a relatively large number of small agglomerates and a few complex agglomerates built by clusters under  $10 \mu\text{m}$ . In the case of  $\text{Al}_2\text{O}_3$ , the size distribution showed peaks at  $2 \mu\text{m}$ ,  $6 \mu\text{m}$  and  $8 \mu\text{m}$ . Finally, image analysis of collected  $\text{SiO}_2$  particles showed agglomerates under  $50 \mu\text{m}$  with main peaks at  $2 \mu\text{m}$  and  $5 \mu\text{m}$ , which agree with the values from the OPC, and smaller contributions at  $8 \mu\text{m}$ ,  $12 \mu\text{m}$  and  $17 \mu\text{m}$ . Images of  $\text{TiO}_2$  and  $\text{Al}_2\text{O}_3$  showed most of the complex agglomerates fractured, broken or even disintegrated on the carbon tape and cellulose ester filter.

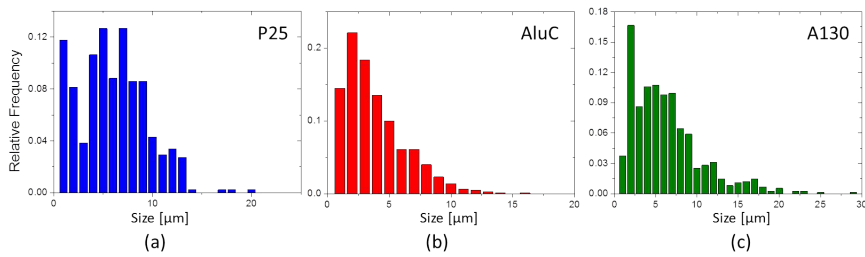


Figure 4.5: Agglomerate size distributions of  $\text{TiO}_2$  (a),  $\text{Al}_2\text{O}_3$  (b) and  $\text{SiO}_2$  (c) from the tape and filter samples analyzed by SEM imaging ( $N = 442, 1000$  and  $745$  for  $\text{TiO}_2, \text{Al}_2\text{O}_3$  and  $\text{SiO}_2$ , respectively).

Large agglomerates (above  $20 \mu\text{m}$ ) in the  $\text{TiO}_2$  bed were measured using the settling tube technique, showing that the average size remained within the same order of magnitude with time, while the size distribution narrowed down after 10 min of fluidization (Figure 4.6). The steady state was reached in about 15 min with an average agglomerate size of  $115 \pm 4 \mu\text{m}$  from a total of 886 agglomerates analyzed.

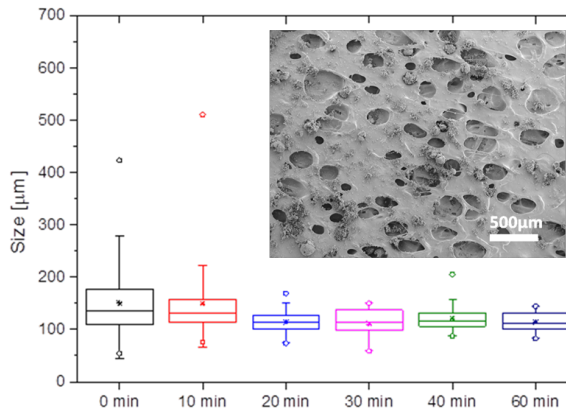


Figure 4.6: Time behavior of fluidized P25 nanopowder. Data gathered from in situ visualization of fluidized agglomerates in the size range of  $20\text{-}1000 \mu\text{m}$ . Inset of SEM image of a P25 fluidized nanopowder sample on carbon tape. The asterisks are the mean values and the empty circles are the maximum and minimum values. The box encompasses the second and third quartiles, divided by a line corresponding to the median. The top and bottom whiskers are the outliers within 1.5 interquartile range.

The combination of aerosol and powder technology methods served to show the whole particle size distributions within or above a fluidized bed of nanopowder. There was a noticeable per count dominance of clusters below  $10 \mu\text{m}$  (Figure 4.7, top), even though most of the primary particles were found in agglomerates larger than  $50 \mu\text{m}$  as seen in the mass contribution plot (Figure 4.7, bottom). It should be noted that mass contribution was calculated assuming spherical agglomerates with 98% porosity built by spherical nanoparticles with sizes obtained from TEM image analysis. The transient behavior of the powder showed an increase on the number of small structures with a remarkable decrease on the large agglomerates (above  $50 \mu\text{m}$ ). Agglomerates below  $20 \mu\text{m}$

were still found after an hour of fluidization, whereas the amount of complex agglomerates decreased significantly, leaving only those between 80  $\mu\text{m}$  and 150  $\mu\text{m}$ .

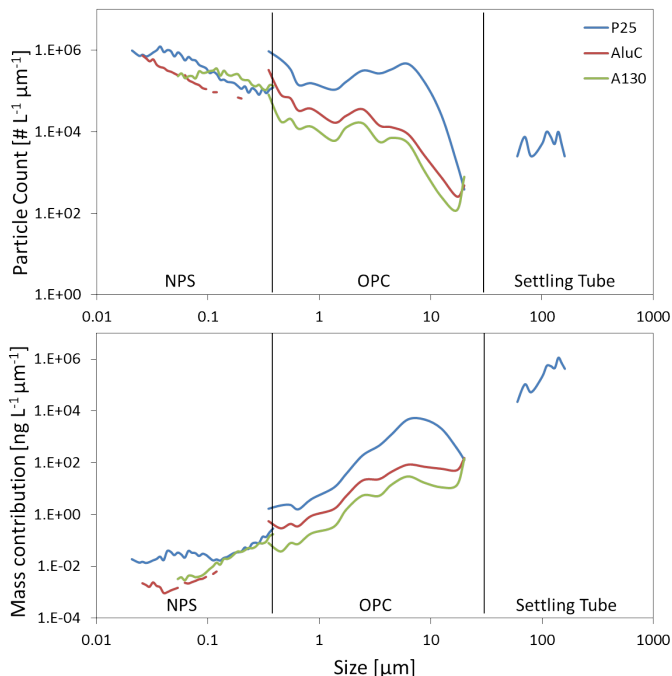


Figure 4.7: Full range size distributions in terms of particle counts (top graph) and mass concentration (bottom graph) of fluidized  $\text{TiO}_2$ ,  $\text{Al}_2\text{O}_3$  and  $\text{SiO}_2$  nanopowders obtained by the combination of NPS, OPC and settling tube methods. For the settling tube, a particle in-flow of 0.5 cm/s was assumed for calculating the particle concentration (in part/l) together with the inlet size and recording time.

Results showed that fluidization produces a high amount of nanoparticle clusters with sizes from nanometers to several microns, along with lower concentrations of larger agglomerates. Furthermore, it was also found that a significant amount of powder is lost during fluidization. The considerable decrease on particle number concentration with fluidization time could be connected to the low Stokes number<sup>1</sup> for soft clusters. Estimation of the Stokes number for nanoparticle clusters with sizes between 20 nm and 30  $\mu\text{m}$  came to  $4 \cdot 10^{-10}$  and  $9 \cdot 10^{-4}$ , respectively, low enough for particles to follow the gas trajectory out of the column. Nonetheless, the decrease in particle count did not affect the size distribution. All nanopowders showed a stable particle size distribution in the range from 5 nm to 20  $\mu\text{m}$ , which could be ascribed to a steady generation of nanosized structures in the bed. It should be noted that continuous generation of nanostructures in the freeboard with preset sizes might be attributed to the production method and powder storage conditions. Assuming the formation of soft agglomerates during fluidization,

<sup>1</sup>Stokes Number (Sk) is a dimensionless parameter that describes a particle's trajectory in a particular fluid flow, and is estimated from the ratio of the relaxation time of the particle ( $\tau$ ) to the characteristic time of the flow as  $d/u_0$ , where  $d$  is the dimension of the obstacle and  $u_0$ , the fluid velocity:  $\text{Sk} = \frac{\tau u_0}{d}$

their continuous collisions could lead to smaller fragments with the size distributions measured in this work.

Knowing that there is a continuous entrainment of nanosized structures out of the fluidized bed along with soft agglomerates have important consequences regarding the design of gas-phase fluidized bed reactors. The significant mass loss and size-scale of the lost matter require the implementation of adequate safeguards for gas-phase nanoparticle processing methods to trap the entrained material. Furthermore, the proposed experimental scheme to determine the particle size distribution and concentration of fluidized nanoparticulate beds could be applied to validate models, which in turn might improve the accuracy of predicting agglomerate population balances, formation mechanisms, and nanopowder processing efficiency by fluidization, which are of interest to industry and studies on the environmental impact of nanoparticle aerosols [48, 49].

#### 4.4. CONCLUSIONS

The fluidization of  $\text{TiO}_2$ ,  $\text{Al}_2\text{O}_3$  and  $\text{SiO}_2$  nanopowders showed the entrainment of nanostructures out of the freeboard, along with the expected micron sized agglomerates. All powders required a starting period of about 15 min to reach a pseudo-steady fluidization state. Particle number concentration and size distribution of the nanostructures showed to be constant along the freeboard height for all the tested nanopowders. The increase in fluidization time showed however a significant drop on the particle number concentration, while keeping stable particle size distribution patterns. At all times and heights, nano-sized particulate matter was overwhelmingly dominant in terms of the total number of particles, while micron-size agglomerates were still the main contributors to the total mass observed in the studied volume. The understanding of nanopowder fluidization has been brought forward by elucidating the transient behavior of fluidized nanopowder, and showing the presence of nanostructures as independent fluidized bodies.

#### REFERENCES

- [1] *Wide Range Aerosol Spectromete*, GRIMM.
- [2] W. J. Stark, P. R. Stoessel, W. Wohlleben, and A. Hafner, *Industrial applications of nanoparticles*, Chem. Soc. Rev. **44**, 5793 (2015).
- [3] A. Chen and S. Chatterjee, *Nanomaterials based electrochemical sensors for biomedical applications*, Chemical Society Reviews **42**, 5425 (2013).
- [4] C. Y. Tay, M. I. Setyawati, J. Xie, W. J. Parak, and D. T. Leong, *Back to basics: Exploiting the innate physico-chemical characteristics of nanomaterials for biomedical applications*, Advanced Functional Materials **24**, 5936 (2014).
- [5] A. Kamyshny and S. Magdassi, *Conductive nanomaterials for printed electronics*, Small **10**, 3515 (2014).
- [6] G. A. Sotiriou, C. Watson, K. M. Murdaugh, T. H. Darrah, G. Pyrgiotakis, A. Elder, J. D.

- Brain, and P. Demokritou, *Engineering safer-by-design silica-coated zno nanorods with reduced dna damage potential*, Environ. Sci.: Nano **1**, 144 (2014).
- [7] A. D. Franklin, *Nanomaterials in transistors: From high-performance to thin-film applications*, Science **349**, 6249 (2015).
- [8] Q. Zhang, E. Uchaker, S. L. Candelaria, and G. Cao, *Nanomaterials for energy conversion and storage*, Chemical Society Reviews **42**, 3127 (2013).
- [9] F. Perreault, A. Fonseca de Faria, and M. Elimelech, *Environmental applications of graphene-based nanomaterials*, Chem. Soc. Rev. **44**, 5861 (2015).
- [10] S. M. Louie and J. M. Pettibone, *Research highlights: engineering nanomaterial-based technologies for environmental applications*, Environ. Sci.: Nano **3**, 11 (2016).
- [11] L. Research, *State of the market report, nanotechnology update: corporations up their spending as revenues for nanoenabled products increase*, (2014).
- [12] F. Balas, M. Arruebo, J. Urrutia, and J. Santamaria, *Reported nanosafety practices in research laboratories worldwide*, Nature Nanotechnology **5**, 93 (2010).
- [13] B. Nowack, N. C. Mueller, H. F. Krug, and P. Wick, *How to consider engineered nanomaterials in major accident regulations?* Environmental Sciences Europe **26**, 1 (2014).
- [14] P. T. O'Shaughnessy, *Occupational health risk to nanoparticulate exposure*, Environmental Science: Processes & Impacts **15**, 49 (2013).
- [15] V. Sebastian, M. Arruebo, and J. Santamaria, *Reaction engineering strategies for the production of inorganic nanomaterials*, Small **10**, 835 (2013).
- [16] C. A. Charitidis, P. Georgiou, M. A. Koklioti, A.-F. Trompeta, and V. Markakis, *Manufacturing nanomaterials: from research to industry*, Manufacturing Rev. **1**, 11 (2014).
- [17] J. Feng, G. Biskos, and A. Schmidt-Ott, *Toward industrial scale synthesis of ultra-pure singlet nanoparticles with controllable sizes in a continuous gas-phase process*, Scientific Reports **5**, 15788 (2015).
- [18] R. Koirala, S. E. Pratsinis, and A. Baiker, *Synthesis of catalytic materials in flames: opportunities and challenges*, Chem. Soc. Rev. **45**, 3053 (2016).
- [19] M. Heurlin, M. H. Magnusson, D. Lindgren, M. Ek, L. R. Wallenberg, K. Deppert, and L. Samuelson, *Continuous gas-phase synthesis of nanowires with tunable properties*, Nature **492**, 90 (2012).
- [20] C. Carotenuto, F. D. Natale, and A. Lancia, *Wet electrostatic scrubbers for the abatement of submicronic particulate*, Chemical Engineering Journal **165**, 35 (2010).
- [21] N. Jennerjohn, A. Eiguren-Fernandez, S. Prikhodko, D. C. Fung, K. S. Hirakawa, J. D. Zavala-Mendez, W. Hinds, and N. J. Kennedy, *Design, demonstration and performance of a versatile electrospray aerosol generator for nanomaterial research and applications*, Nanotechnology **21**, 255603 (2010).

- [22] A. L. Holder, E. P. Vejerano, X. Zhou, and L. C. Marr, *Nanomaterial disposal by incineration*, Environ. Sci.: Processes Impacts **15**, 1652 (2013).
- [23] V. Gomez, S. Irusta, F. Balas, N. Navascues, and J. Santamaria, *Unintended emission of nanoparticle aerosols during common laboratory handling operations*, Journal of Hazardous Materials **279**, 75 (2014).
- [24] V. Gomez, A. Clemente, S. Irusta, F. Balas, and J. Santamaria, *Identification of TiO<sub>2</sub> nanoparticles using la and ce as labels: application to the evaluation of surface contamination during the handling of nanosized matter*, Environ. Sci.: Nano **1**, 496 (2014).
- [25] T. A. Kuhlbusch, C. Asbach, H. Fissan, D. Göhler, and M. Stintz, *Nanoparticle exposure at nanotechnology workplaces: A review*, Particle and Fibre Toxicology **8**, 1 (2011).
- [26] C.-J. Tsai, C.-Y. Huang, S.-C. Chen, C.-E. Ho, C.-H. Huang, C.-W. Chen, C.-P. Chang, S.-J. Tsai, and M. J. Ellenbecker, *Exposure assessment of nano-sized and respirable particles at different workplaces*, Journal of Nanoparticle Research **13**, 4161 (2011).
- [27] M. R. Wiesner, G. V. Lowry, P. Alvarez, D. Dionysiou, and P. Biswas, *Assessing the risks of manufactured nanomaterials*, Environmental Science & Technology **40**, 4336 (2006).
- [28] S. Wagner, A. Gondikas, E. Neubauer, T. Hofmann, and F. von der Kammer, *Spot the difference: Engineered and natural nanoparticles in the environment-release, behavior, and fate*, Angewandte Chemie International Edition **53**, 12398 (2014).
- [29] J. R. van Ommen, D. Kooijman, M. d. Niet, M. Talebi, and A. Goulas, *Continuous production of nanostructured particles using spatial atomic layer deposition*, Journal of Vacuum Science & Technology A **33**, 021513 (2015).
- [30] A. Goulas and J. Ruud van Ommen, *Atomic layer deposition of platinum clusters on titania nanoparticles at atmospheric pressure*, J. Mater. Chem. A **1**, 4647 (2013).
- [31] X. Liang, K. S. Barrett, Y.-B. Jiang, and A. W. Weimer, *Rapid silica atomic layer deposition on large quantities of cohesive nanoparticles*, ACS Applied Materials & Interfaces **2**, 2248 (2010).
- [32] D. C. Vennerberg, R. L. Quirino, Y. Jang, and M. R. Kessler, *Oxidation behavior of multiwalled carbon nanotubes fluidized with ozone*, ACS Applied Materials & Interfaces **6**, 1835 (2014).
- [33] M. Tahmasebpour, L. de Martín, M. Talebi, N. Mostoufi, and J. R. van Ommen, *The role of the hydrogen bond in dense nanoparticle-gas suspensions*, Phys Chem Chem Phys **15**, 5788 (2013).
- [34] L. de Martin and J. van Ommen, *A model to estimate the size of nanoparticle agglomerates in gas-solid fluidized beds*, Journal of Nanoparticle Research **15**, 2055 (2013).

- [35] D. Geldart, *Types of gas fluidization*, Powder Technology **7**, 285 (1973).
- [36] J. R. van Ommen, J. M. Valverde, and R. Pfeffer, *Fluidization of nanopowders: a review*, J Nanopart Res **14**, 737 (2012).
- [37] J. M. Valverde, M. A. S. Quintanilla, A. Castellanos, D. Lepek, J. Quevedo, R. N. Dave, and R. Pfeffer, *Fluidization of fine and ultrafine particles using nitrogen and neon as fluidizing gases*, AIChE J **54**, 86 (2008).
- [38] J. Scicolone, D. Lepek, L. Louie, and R. N. Dave, *Fluidization and mixing of nanoparticle agglomerates assisted via magnetic impaction*, Journal of Nanoparticle Research **15**, 1 (2013).
- [39] S. Matsuda, H. Hatano, T. Muramoto, and A. Tsutsumi, *Modeling for size reduction of agglomerates in nanoparticle fluidization*, Aiche Journal **50**, 2763 (2004).
- [40] C. Zhu, Q. Yu, R. N. Dave, and R. Pfeffer, *Gas fluidization characteristics of nanoparticle agglomerates*, AIChE Journal **51**, 426 (2005).
- [41] C. H. Nam, R. Pfeffer, R. N. Dave, and S. Sundaresan, *Aerated vibrofluidization of silica nanoparticles*, AIChE Journal **50**, 1776 (2004).
- [42] X. S. Wang, V. Palero, J. Soria, and M. J. Rhodes, *Laser-based planar imaging of nanoparticle fluidization: Part I: determination of aggregate size and shape*, Chem Eng Sci **61**, 5476 (2006).
- [43] J. A. Quevedo, A. Omosebi, and R. Pfeffer, *Fluidization enhancement of agglomerates of metal oxide nanopowders by microjets*, AIChE Journal **56**, 1456 (2010).
- [44] L. de Martin, J. Sanchez-Prieto, F. Hernandez-Jimenez, and J. van Ommen, *A settling tube to determine the terminal velocity and size distribution of fluidized nanoparticle agglomerates*, Journal of Nanoparticle Research **16**, 2183 (2013).
- [45] L. de Martin, A. Fabre, and J. R. van Ommen, *The fractal scaling of fluidized nanoparticle agglomerates*, Chemical Engineering Science **112**, 79 (2014).
- [46] L. de Martin, W. G. Bouwman, and J. R. van Ommen, *Multidimensional nature of fluidized nanoparticle agglomerates*, Langmuir **30**, 12696 (2014).
- [47] A. Clemente, F. Balas, M. P. Lobera, S. Irusta, and J. Santamaria, *Fluidized bed generation of stable silica nanoparticle aerosols*, Aerosol Science and Technology **47**, 867 (2013).
- [48] W. Wohlleben, S. Brill, M. W. Meier, M. Mertler, G. Cox, S. Hirth, B. von Vacano, V. Strauss, S. Treumann, K. Wiench, L. Ma-Hock, and R. Landsiedel, *On the lifecycle of nanocomposites: Comparing released fragments and their in-vivo hazards from three release mechanisms and four nanocomposites*, Small **7**, 2384 (2011).
- [49] P. O. Andersson, C. Lejon, B. Ekstrand-Hammarström, C. Akfur, L. Ahlinder, A. Bucht, and L. Österlund, *Polymorph- and size-dependent uptake and toxicity of TiO<sub>2</sub> nanoparticles in living lung epithelial cells*, Small **7**, 514 (2011).

## APPENDIX 4.A

## MATERIAL SPECIFICATIONS

Table 4.2: Properties of the nanoparticles as provided by the manufacturer.

Powder	$\rho_p$ (kg m <sup>-3</sup> )	$d_p$ (nm)
TiO <sub>2</sub> P25	4000	21
Al <sub>2</sub> O <sub>3</sub> AluC	3600	13
SiO <sub>2</sub> A130	2200	16

The size distribution of all powders was determined from TEM images analyzed with the open source software ImageJ. The mean primary particle sizes measured were  $22 \pm 7$  nm,  $8 \pm 2$  nm, and  $16 \pm 7$  nm for P25, AluC, and A130, respectively (Figure 4.8). The discrepancy in the size of AluC particles with respect to nominal values given by the supplier could be attributed to the particle overlap or partial sintering seen on the TEM images. Additionally, industry use the gas absorption-desorption method for particle sizing, which most likely results in different values than image analysis.

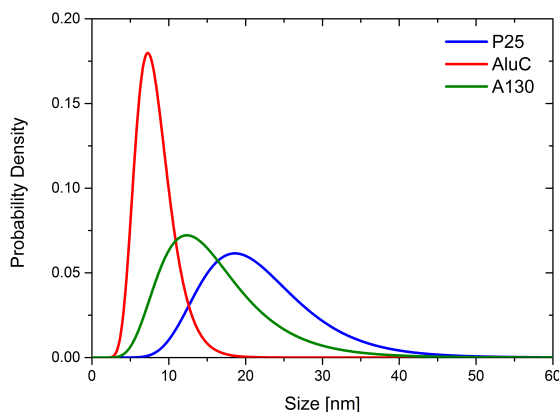


Figure 4.8: Primary particle size distribution of titania (P25), alumina (AluC), and silica (A130) nanopowders. Values were obtained from TEM images analyzed by the open source software ImageJ.

## AEROSOL MEASURING DEVICES

The NPS (Nano-ID<sup>TM</sup>NPS500, Particle Measuring Systems) is a high resolution condensation particle counter with 64 channels/decade, has a sensitivity of 10 nm with a sample flow rate of  $0.2 \text{ L min}^{-1}$  and the lowest zero-count specification in the industry. The OPC (OPC, model #1.108 Grimm Technik) has 15 channels for particle count in a sample flow of  $1.2 \text{ L min}^{-1}$ , able to measure up to 2 million particles per liter with a sensitivity of 2%.



## MICROSCOPE ANALYSIS SAMPLING METHOD

Three different methods were used to capture samples from the fluidized bed for TEM and SEM imaging.

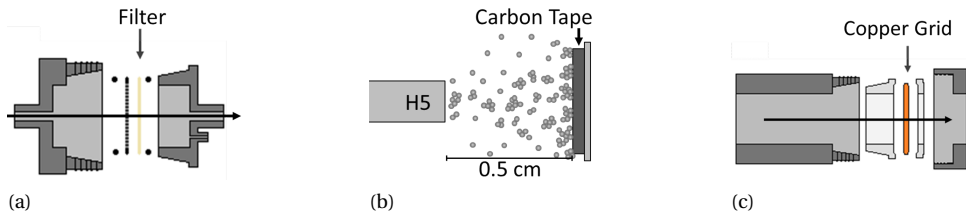


Figure 4.9: a) 50 nm mesh filter, b) Double sided carbon tape, and c) copper grid holders for airborne particles capture. The filter and carbon tape are used for SEM analysis, and the copper grid for TEM imaging. The arrows show the flow direction from the fluidized bed sampling port.

# 5

## CHARACTERIZATION OF THE STRATIFIED MORPHOLOGY OF NANOPARTICLE AGGLOMERATES

Nanoparticles surrounded by gas agglomerate in a hierarchical fashion. From production until powder processing in the gas phase, nanoparticles go from individual particles to aggregates, simple agglomerates, and complex agglomerates. Even though the structures at each level have unique properties, they are commonly assessed as a whole. Additionally, the effect of external factors on the morphology of these structures during gas processing is not well understood, and challenging to study due to the limited techniques for *in situ* analysis of the dynamic phenomenon. Here, we study three materials in their hydrophobic and hydrophilic version. We describe the structural characteristics of each hierarchical level of complex agglomerate formation obtained from two *in situ* techniques. The first scale, namely aggregates, are open structures with a fractal dimension of about 1.5, which then form simple agglomerates with a fractal dimension close to 3, that later cluster into complex agglomerates that present a fractal dimension of about 2. Furthermore, gas dynamics were found to densify the simple agglomerates increasing their fractal dimension by more than 0.1.

## 5.1. INTRODUCTION

Nanoparticle agglomeration is of tremendous importance in medicine, energy storage, catalysis, consumer products, etc [2]. This process develops in a stepwise fashion, where the structures formed at each step have unique properties and thus, react differently to the mechanical interactions they are exposed to [3–5]. This paper presents underlying morphological differences among the nanoparticle clusters generated throughout the agglomeration process, and the effect of external factors during powder processing; more specifically, during nanopowder suspension in an upward gas flow (i.e. fluidization).

Nanoparticles are of great interest in academia and industry due to their unique properties which make them suitable for applications such as in textiles, electronics, medicine, and renewable energy [4, 6–12]. Some of these applications require the adaptation of the nanoparticles to the desired function [13]. Due to its potential scalability and large gas-solid contact area, fluidization is commonly used for nanoparticle processing [3, 9, 14–18]. Nonetheless, particles at this scale fluidize as clusters due to the relatively strong adhesion forces [4, 19–26], a behavior that could hamper characteristics of the individual particles.

Nanoparticle agglomeration is a hierarchical process [3, 4]. During particle production at high temperatures, nanoparticles come into contact and form chain-like structures of a few hundreds of nanometers called aggregates, connected by solid necks and assumed to be very hard, if not impossible to break [5, 27, 28]. While stored, these aggregates form highly porous clusters named simple aggregates, which can reach tens of micrometers in size. The stored nanopowder is then processed in a fluidized bed, where it creates complex agglomerates from the simple agglomerates already present. As a stepwise growth, each of the three structures have unique properties.

The nanoparticle cluster is commonly characterized by its fractal-like structure [4, 19, 29–34]. The  $N_p$  number of monodisperse particles with size  $d_p$  forming a mass fractal cluster of size  $d_a$  scales to the power of the ratio  $d_a/d_p$  according to

$$N_p = k_n \left( \frac{d_a}{d_p} \right)^{D_f} \quad (5.1)$$

which in terms of density translates to

$$\rho_a = \rho_p k_n \left( \frac{d_a}{d_p} \right)^{D_f-3} \quad (5.2)$$

where  $\rho_a$  is the cluster density,  $\rho_p$  is the particle density,  $k_n$  is a prefactor, and  $D_f$  is the mass fractal dimension [35]. The prefactor is used to give physical meaning to the expression at the limits of the single nanoparticle and extremely large clusters. The mass fractal dimension gives information on the nanoparticle distribution within the structure, which is a key feature to consider when studying cluster morphology.

The agglomerate morphology can be affected by external factors such as the fluidizing gas or collisions with other solids [8, 19, 36]. Studying the structure of the fluidized agglomerates *in situ* is quite challenging. Visualization of fluidized agglomerates has been achieved before [8, 9, 14, 37, 38]. Nonetheless, it should be noted that visual analysis is always difficult since the data consists of 2D images of 3D objects. Moreover, all

camera-based techniques are limited by the maximum resolution of the image. Other techniques such as  $\gamma$ -rays adsorption densitometry have been used to study the fluidized bed [15]; however, the detailed morphology of the fluidized structures could not be determined from this method.

Previously, de Martin et al. [31] described the morphology of the multiple agglomerate scales of static  $\text{SiO}_2$  (R812) and  $\text{TiO}_2$  (P25), and fluidized  $\text{TiO}_2$  (P25). Titania P25 consists of hydrophilic 21 nm primary particles that fluidize with channels and bubbles. Since only one nanopowder was analyzed in the fluidized state, the applicability of the results to a wider range of powders was open to debate. Since the inherent morphology of the agglomerate depends on the properties of the primary particles, which include material and surface characteristics such as the presence of hydroxide groups [4, 26], data analysis of a single powder sample suggested interpretations that required further research.

Here, an *in situ* study of the morphology of the structures at the different agglomeration levels of six metal oxide nanopowders is presented. We compare the static and fluidized states to find the scale at which the fluidization dynamics modify the morphology of the agglomerates, which presumably should not reach the strong aggregates. Moreover, a preliminary comparison between hydrophobic and hydrophilic powders is made since the presence of hydroxide groups can strengthen the clusters via hydrogen bonds; hence, enhancing their resistance to morphological changes. This study determines the static and dynamic fractal dimension of nanoparticle aggregates, simple agglomerates, and complex agglomerates using the spin-echo small-angle neutron scattering (SESANS) [31, 39, 40] technique for the first two scales, and the settling tube technique [35, 41] for the third one.

## 5.2. METHODS

### 5.2.1. MATERIALS

Hydrophilic (P) and hydrophobic (A) versions of  $\text{TiO}_2$ ,  $\text{Al}_2\text{O}_3$ ,  $\text{SiO}_2$  commercial nanopowders from Evonik are used in this work; the same set as in previous studies [26, 42]. The specifications given by the provider are shown in Table 6.1. All six powders were fluidized and studied with the settling tube technique. However, only titania and alumina were studied with SESANS since experiments on silica were limited by the fluidization dynamics of the powder making it adhere to the walls giving erroneous measurements.

Table 5.1: Properties of the fluidized nanopowders. The particle density and size are provided by the manufacturer.

Powder	Commercial name	Surface	$\rho_p$ (kg/m <sup>3</sup> )	$d_p$ (nm)
$\text{TiO}_2$ -P	P25	hydrophilic	4000	21
$\text{TiO}_2$ -A	T805	hydrophobic	4000	21
$\text{Al}_2\text{O}_3$ -P	AluC	hydrophilic	3600	13
$\text{Al}_2\text{O}_3$ -A	AluC805	hydrophobic	3600	13
$\text{SiO}_2$ -P	A130	hydrophilic	2200	16
$\text{SiO}_2$ -A	R972	hydrophobic	2200	16

Previous to fluidization, all powders were sieved to remove agglomerates larger than  $400\ \mu\text{m}$  in size to improve fluidization [9]. The powders were fluidized within the next 24 hours after sieving to prevent further formation of large clusters. The measurements with SESANS and the settling tube were made once the fluidized bed had reached a pseudo-steady state with minimal height fluctuations.

### 5.2.2. SESANS

The properties of the nanoparticle aggregates and simple agglomerates were studied *in situ* by the spin-echo small-angle neutron scattering (SESANS) technique which covers the size range from  $5\text{nm}$  to  $20\ \mu\text{m}$  [39]. The time required for each experiment varied between 1 and 5 hours. The measurements are obtained from the polarization of a neutron beam which passes through a precession device with tilted interface before crossing the sample, and through a second precession device with opposite magnetic field direction after the sample, before reaching the detector [31, 39].

The setup for SESANS consists of a fluidization column made by a single piece of quartz with a  $30 \times 25\ \text{mm}$  rectangular cross-section. The rectangular area was chosen to ensure that the whole neutron beam would travel through the sample exactly the same distance (Fig.5.1). The area of the beam is  $16 \times 10\ \text{mm}$  with a wavelength of  $0.203 \pm 0.001\ \text{nm}$ . The size of the column was determined from preliminary measurements on neutron depolarization of the different nanopowders using cuvettes. The distance traveled by the beam through the sample affects the level of neutron depolarization, and the optimum sample depth depends on the material properties; thus, varies among the powders used. From the cuvette experiments it was determined that all powders required a sample thickness of  $30\ \text{mm}$ , with the exception of hydrophobic  $\text{TiO}_2\text{-A}$ , which needed  $25\ \text{mm}$ .

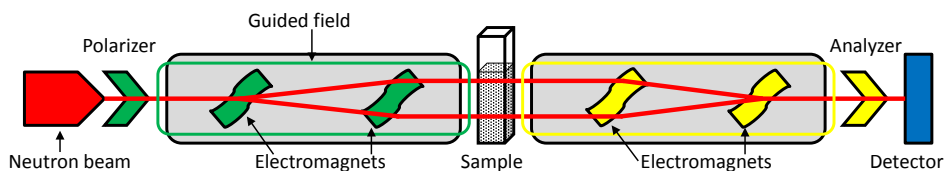


Figure 5.1: Schematic of the SESANS setup. Main parts are labeled with the neutron beam going from left to right, passing through the sample placed at the middle of the beam trajectory.

The column had distributor plates at the top and bottom; the bottom one to spread the fluidizing gas, and the top one to prevent particle loss. After sieving, the powders were placed inside the column to a height of  $6 \pm 1\ \text{cm}$ , enough to guarantee full sample coverage of the neutron beam. The powders were fluidized at  $4.5\ \text{cm/s}$ – $8.3\ \text{cm/s}$  with  $\text{N}_2$  gas for about 5 hours. Measurements were taken before, during, and in some cases, after fluidization for  $\text{TiO}_2\text{-P}$ ,  $\text{TiO}_2\text{-A}$ ,  $\text{Al}_2\text{O}_3\text{-P}$ , and  $\text{Al}_2\text{O}_3\text{-A}$  powders.

### 5.2.3. SETTLING TUBE

The settling tube setup comprises a 45×45 mm cross-sectional area quartz column, 15 cm high, with a distributor plate at the bottom, and a bubbler and HEPA filter attached to the top to trap any entrained nanopowder. One of the column's side walls has two openings for the connections of the settling tube. This settling tube is a black box with dimensions 10×6×30 mm, an opening at the top to catch the falling agglomerates, and two side openings for the borescope-high-speed camera system and the flushing gas that empties the box before each experiment (Fig.5.2). A rigid Olympus (R040-021-000-60 S5) borescope and a high-speed Phantom v9.1 camera are used for *in situ* fluidized agglomerate visualization [35, 41] in the range of 30  $\mu\text{m}$  to 1 mm.

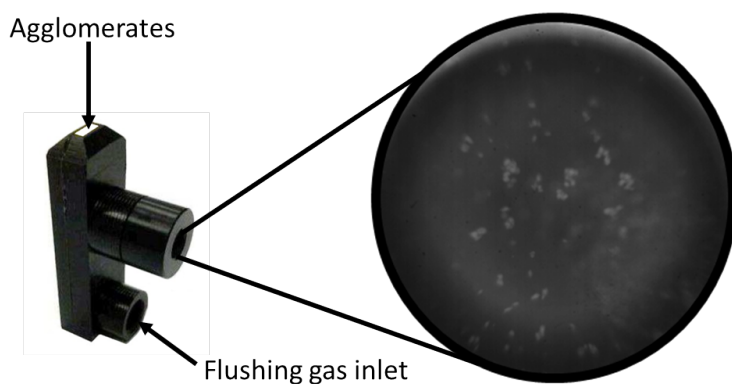


Figure 5.2: Settling tube with the agglomerate inlet at the top, and the borescope and flushing gas inlet on the side. A sample image of the recorded fluidized agglomerates is shown.

All six nanopowders were analyzed with the settling tube technique. The nanopowders were fluidized with  $\text{N}_2$  at 0.13 m/s after being sieved to remove structures larger than 400  $\mu\text{m}$ . The recordings were taken 15 minutes after fluidization, once the bed height was steady.

## 5.3. DATA ANALYSIS

The data obtained from SESANS is the polarization ( $P$ ) as a function of the spin-echo length ( $z$ ) (Fig.5.3). The spin-echo length covers the range of 5 nm-20  $\mu\text{m}$ . The relation between polarization and spin-echo length is characterized by the correlation function, which describes the density of the sample.

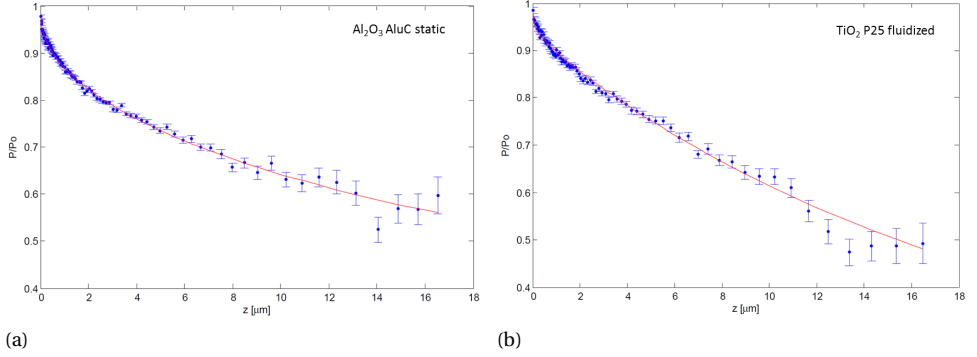


Figure 5.3: Sample plots of static  $\text{Al}_2\text{O}_3\text{-P}$  (a) and fluidized  $\text{TiO}_2\text{-P}$  (b) obtained from SESANS. Polarization is normalized by that of an empty container ( $P_0$ ). The best fit from equation 5.8 is shown as a red line. The first and second fractal dimensions ( $D_{f1}$  and  $D_{f2}$ , respectively), and transition size ( $r_{c1}$ ) obtained from each plot are presented.

Since SESANS does not give straight forward information about the sample properties, thorough data processing and qualitative understanding of the sample morphology are necessary. The solid fraction of the fluidized samples was determined from the voidage of the static powder, and transmission values from the empty column and fluidized bed from the following equation:

$$T = Ae^{B(1-\phi_f)} \quad (5.3)$$

where  $T$  is the SESANS transmission of the sample,  $A$  is the transmission of the empty column,  $B$  is the voidage of the static samples estimated as  $B = 1 - \rho_b/\rho_p$ , and  $\phi_f$  is the solid fraction of the fluidized powder.

To relate the experimental data to the sample properties, a theoretical polarization based on known fluidization conditions and powder properties is evaluated, compared, and reiterated until agreeing with the experimental polarization. The estimation of the theoretical polarization requires knowledge on the density-density correlation function for the sample, the projection of the density-density correlation function in the form of an Abel transform, and the solid fraction of the sample. A detailed description of the SESANS data analysis can be found in the publications by de Martin et al.[31, 43] and Andersson et al.[40, 44].

The density-density correlation function for a bifractal system is described as:

$$\gamma \propto \left(\frac{r}{r_p} + 1\right)^{D_{f,1}-3} \quad r < r_{c1} \quad (5.4)$$

$$\gamma \propto \left(\frac{r}{a} + 1\right)^{D_{f,2}-3} e^{-\frac{r}{\xi}} \quad r > r_{c1} \quad (5.5)$$

Where  $r_{c1}$  is a characteristic length scale indicating the transition from one density-density correlation function to the other, and not a radius. The correlation length of the density distribution  $\xi$  is equal to the width of the distribution, which means that:

$$\xi = 2 \int_z^\infty \gamma(r) dr \quad (5.6)$$

By an Abel transform, the projection of the density-density correlation function reads as follows:

$$G(z) = \frac{2}{\xi} \int_z^\infty \frac{\gamma(r)r}{\sqrt{r^2 - z^2}} dr \quad (5.7)$$

To analyze the data extracted from SESANS, a theoretical polarization of the neutrons is estimated and compared to the experimental values for optimization of the initial parameters ( $D_{f1}$ ,  $D_{f2}$ , and  $r_{c1}$ ). The expression for the theoretical polarization is:

$$P(z) = e^{\Sigma_t(G(z)-1)} \quad (5.8)$$

where  $\Sigma_t$  depends on the sample thickness  $t$ , neutron wavelength  $\lambda$ , neutron scattering length density difference in the sample  $\Delta\rho_0$ , correlation length of the density distribution  $\xi$ , solid fraction  $\phi_1$ , and void fraction  $\phi_2$  as shown below:

$$\Sigma_t = t\lambda^2 \Delta\rho_0^2 \phi_1 \phi_2 \xi \quad (5.9)$$

Once all the values are calculated, the error between the theoretical and experimental polarizations is evaluated. If the error does not meet the threshold, the loop of calculation is restarted with new values. In this manner, the fractal dimension and transition size for the first and second scales can be obtained from the SESANS measurements.

Video analysis of the settling tube experiments is done using in-house MATLAB scripts [41]. The video have a resolution of  $5.6\mu\text{m}$  per pixel, giving a minimum recognizable size of  $\approx 12\mu\text{m}$ . A background frame per video is created after MATLAB evaluates all the recorded frames, and then subtracts it to remove the noise. The group of backgroundless frames are looped to recognize all the agglomerates, track them, and filter the ones that attach to the window or get out of focus.

Once a list of labeled agglomerates is made with their respective frame location, size, and sphericity, the settling velocity  $U_t$  and gyration diameter  $d_a$  are estimated assuming that the agglomerates follow Stokes Law [35, 41]. As fractal aggregates in the Stokes regime, the gyration diameter is estimated as 2/3 the outer diameter measured from the videos [45]. Since the average sphericity  $\delta$  of the agglomerates is about 0.9, they are assumed to be spheres, thus, the gyration diameter  $d_a$ , area  $A_a$ , and volume  $V_a$  are directly obtained from the videos. With this data, the Reynold's number  $Re$  is evaluated, which then is used to calculate the drag coefficient  $C_D$ , completing all the parameters needed to determine the agglomerate density  $\rho_a$  as follows:

$$\rho_a = \frac{U_t^2 A_a C_D \rho_f}{g 2 V_a} + \rho_f \quad (5.10)$$

The logarithmic form of Eq. 5.2 gives a line which depends on the size and density of the nanoparticle and agglomerate. The agglomerate size and density are obtained from the videos, while those of the primary particles are given by the provider. Then, the prefactor  $\hat{k}_{n3}$  and fractal dimension  $D_{f3}$  of the recorded fluidized agglomerates is calculated.



## 5.4. RESULTS AND DISCUSSION

### 5.4.1. SESANS

SESANS was used to study the structure of the first two formation levels of complex fluidized agglomerates, which we call aggregates and simple agglomerates. The varying parameters were the material, hydrophobicity, and dynamic state of the powder. Aggregates are known to be connected by solid necks that can withstand any external forces [3], which means that the  $r_{c1}$  obtained for the static powder is fixed for the fluidized samples. The stable aggregates are characterized by  $D_{f1}$  (Fig.5.4(a)), which should then be the same for the static and fluidized samples. Hence,  $D_{f1}$  was left as a fitting parameter for the fluidized system to confirm the value obtained for the static sample; indeed, we found the same  $D_{f1}$  with experimental accuracy for the static and fluidized systems. To verify the experimental reproducibility, in addition to  $D_{f1}$ ,  $r_{c1}$  was also kept as a fitting parameter and compared for the static and fluidized samples (Appendix 5.A). It was found that  $r_{c1}$  and  $D_{f1}$  were consistent between the static and fluidized samples, resulting in a first fractal dimension below 2 and an aggregate size below 500 nm for all the materials, hydrophobicity, and dynamic state. Hence, fluidization dynamics have no effect at the aggregate scale.

On the other hand, the values obtained for  $D_{f2}$  allow for the comparison among materials, properties, and dynamic state (Fig.5.4(b)). There is no significant difference among the materials; however, as seen in Figure 5.4(b), the hydrophobic version of the nanopowders has a higher fractal dimension than the hydrophilic one, showing a difference slightly higher than the confidence interval. The divergence between the hydrophobic and hydrophilic materials can be attributed to the influence of the OH groups on the interactions among the particles [26, 42]. The presence of OH affect the presence of H-bonds, which increase the force required to rearrange the particles within the agglomerate, thus making it harder to modify.

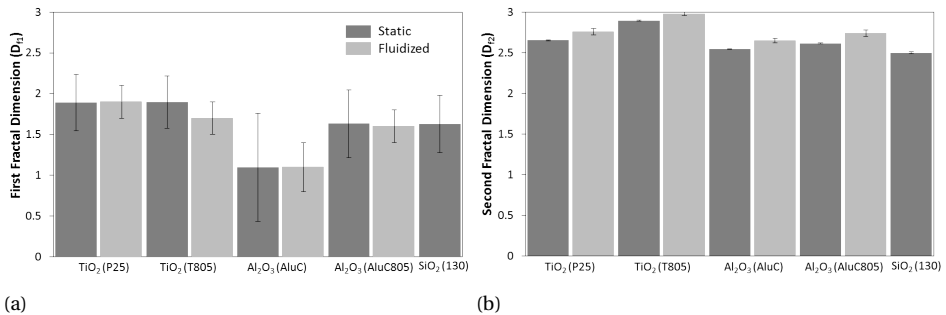


Figure 5.4: First (a) and second (b) fractal dimensions of static (solid) and fluidized (light patterned) nanopowders. Values for TiO<sub>2</sub>-P, TiO<sub>2</sub>-A, Al<sub>2</sub>O<sub>3</sub>-P, Al<sub>2</sub>O<sub>3</sub>-A, and SiO<sub>2</sub>-P are presented. The error bars are the best fit confidence interval of Eq.5.8

It is also shown that, in contrast with the TiO<sub>2</sub>-P results of de Martin et al.[31], the fluidized nanopowders (light bars) have a higher value for  $D_{f2}$  than the static sample (solid bars) (Fig.5.4(b)). During fluidization, agglomerates collide, break, coalesce, and

deform; a dynamic that has been confirmed by fluidizing nanopowders of three different colors (red, green, and white) and finding agglomerates with a combination of all the colors [14]. The impact of this unsteadiness on the morphology of the agglomerate was unknown until now. The evident divergence on the second fractal dimension of the static and fluidized samples suggests that fluidization densifies the structures in the 1-20  $\mu\text{m}$  size range. As the simple agglomerates collide in the fluidized bed, numerous outcomes are possible depending on the relative collision velocity and angle, and the properties of the colliding structures. Some collisions have enough energy to compress the agglomerates by rearranging the aggregates within them, and leading to a bounce or coalesce of the colliding clusters. Collisions with less energy most likely result in the coalescence of the simple agglomerates, loosely joined by interparticle forces among protruding aggregates, thus creating the complex agglomerates with very low density known to be in the fluidized bed and observed with the settling tube.

#### 5.4.2. SETTLING TUBE

From the recordings, the size and settling velocity of the agglomerates can be extracted, and used to estimate the fractal dimension and prefactor when combined with the primary particle properties (Appendix D). The size range of the recorded agglomerates is 50-980  $\mu\text{m}$ , which agrees with the size found in literature of 70-900  $\mu\text{m}$  [8, 9, 14, 33, 37]. The prefactor and fractal dimension are estimated from a linear fit using the logarithm of Eq. 5.2 to the experimental data. In all cases, except for  $\text{SiO}_2\text{-P}$ , the coefficient of determination was above 0.8, which indicates a considerably good fit to the experimental data. For  $\text{SiO}_2\text{-P}$ , the coefficient was 0.53 (Fig. 5.5 (c)). The sparse cloud of data points below the denser cloud of  $\text{SiO}_2\text{-P}$  could be the agglomerates falling close to the window with an inclined trajectory, at a seemingly lower velocity than their corresponding settling velocity. The prefactor and fractal dimension calculated from the best fit line are shown in Table 5.2. The error on the prefactor can be quite large since it is obtained from the line intercept on the  $\log(\rho_a/\rho_p)$  axis and the error propagation from the uncertainty on the agglomerate density results in the given values.

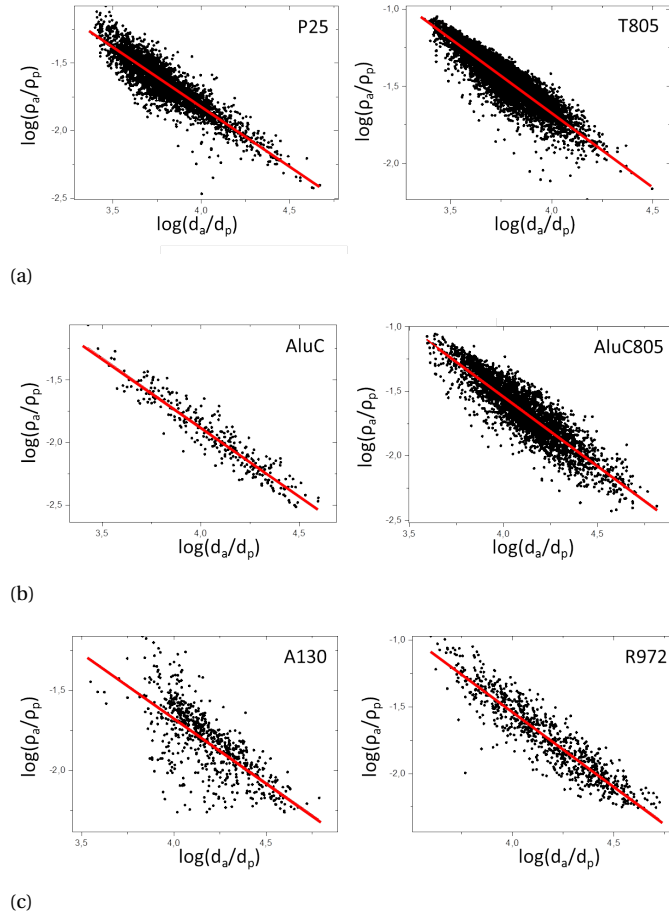


Figure 5.5: The plots show the data points of the complex agglomerates as recorded by the settling tube, with the best fit line from which the prefactor and fractal dimension were extracted. Data from  $\text{TiO}_2$ -P (left) and  $\text{TiO}_2$ -A (right) (a);  $\text{Al}_2\text{O}_3$ -P (left) and  $\text{Al}_2\text{O}_3$ -A (right) (b), and  $\text{SiO}_2$ -P (left) and  $\text{SiO}_2$ -A (right) (c).

Table 5.2: Prefactor and fractal dimension of complex nanoparticle agglomerates estimated from the number of data points indicated on the last column.

Powder	$\hat{k}_n$ (-)	$D_f$ (-)	Data Points
$\text{TiO}_2$ -P	$51 \pm 3$	$2.12 \pm 0.01$	3276
$\text{TiO}_2$ -A	$150 \pm 6$	$2.04 \pm 0.01$	8880
$\text{Al}_2\text{O}_3$ -P	$367 \pm 76$	$1.89 \pm 0.02$	295
$\text{Al}_2\text{O}_3$ -A	$584 \pm 51$	$1.92 \pm 0.01$	3483
$\text{SiO}_2$ -P	$38 \pm 11$	$2.19 \pm 0.03$	683
$\text{SiO}_2$ -A	$747 \pm 117$	$1.90 \pm 0.02$	819

There is no trend among the hydrophobicity and material of the different powders.

TiO<sub>2</sub>-P and SiO<sub>2</sub>-P have a higher fractal dimension than TiO<sub>2</sub>-A and SiO<sub>2</sub>-A; whereas for Al<sub>2</sub>O<sub>3</sub>, the opposite seems to be true. Additionally, the pattern on the values according to the material is not clear given the large discrepancy between the SiO<sub>2</sub> powders. Nevertheless, it is clear that the structure of the agglomerates is rather dilute at this scale.

### 5.4.3. COMBINING ALL THREE SCALES

The results from both techniques, SESANS and settling tube, were merged to give an overall picture of the fluidized agglomerate structure (Fig.5.6). An estimate of the second scale prefactor was obtained by equating Eq. 5.2 for the first and second scales with the fractal dimensions and transition size determined from SESANS. Likewise, the size at the intersection between the second and third scales was estimated from Eq. 5.2 using the previously determined fractal dimensions and prefactors (Appendix). A compilation of all three fractal dimensions for each powder is shown in Table 6.2.

Table 5.3: Fractal dimension of all three hierarchical levels of the agglomeration process during fluidization.

Powder	$D_{f1}$ (-)	$D_{f2}$ (-)	$D_{f3}$ (-)
TiO <sub>2</sub> -P	1.9 ± 0.2	2.76 ± 0.04	2.12 ± 0.01
TiO <sub>2</sub> -A	1.7 ± 0.2	2.98 ± 0.02	2.04 ± 0.01
Al <sub>2</sub> O <sub>3</sub> -P	1.1 ± 0.3	2.65 ± 0.03	1.89 ± 0.02
Al <sub>2</sub> O <sub>3</sub> -A	1.6 ± 0.2	2.74 ± 0.04	1.92 ± 0.01
SiO <sub>2</sub> -P	1.6 ± 0.2	2.64 ± 0.09	2.19 ± 0.03
SiO <sub>2</sub> -A			1.90 ± 0.02

The superposition of the data points from the settling tube to the continuous line estimated from the values mentioned before shows an extension of the settling tube data points over the predicted line for the simple agglomerates (Fig.5.6(a)(c)(d)). This misfit could arise from the large uncertainty of the first fractal dimension and the transition size obtained from SESANS (Appendix). A smoother continuous prediction of the size to density correlation could be made with a smaller transition size, or a higher first fractal dimension. Therefore, further studies on the first scale will confirm the adequate adjustment for the precise values to predict the full agglomeration range.

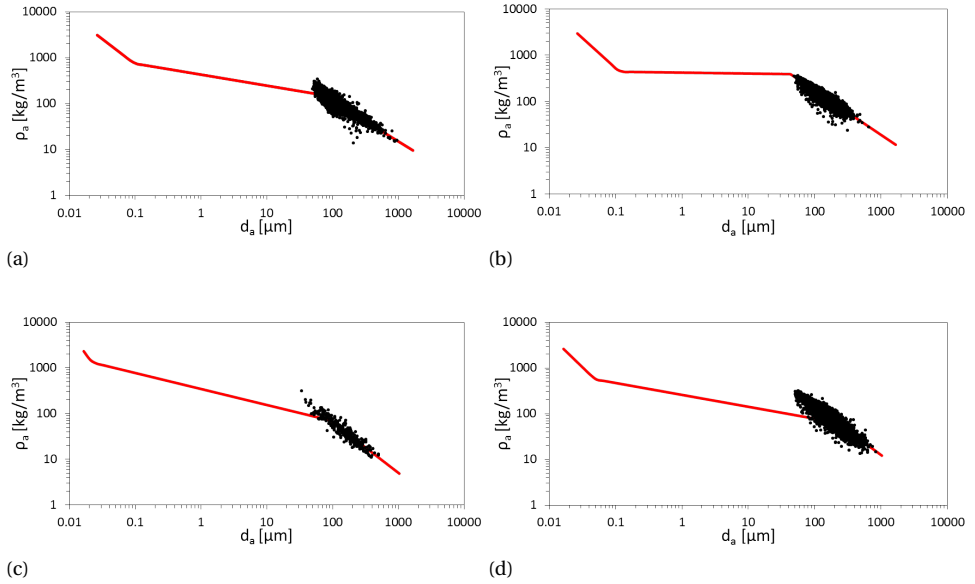


Figure 5.6: a)  $\text{TiO}_2\text{-P}$ , b)  $\text{TiO}_2\text{-A}$ , c)  $\text{Al}_2\text{O}_3\text{-P}$ , d)  $\text{Al}_2\text{O}_3\text{-A}$

As mentioned before,  $D_{f1}$  and  $r_{c1}$  should be the same for static and fluidized powders since aggregates are connected by solid necks, resistant to any external force. On the other hand, the increase of  $D_{f2}$  on the fluidized samples fits the results from the settling tube. If the second scale was kept the same for the static and fluidized powders, the connection between the simple and complex fluidized agglomerates would not be possible (Fig.5.7, dotted blue line). The static powder does not make individual complex agglomerates since the whole batch of powder is a network without a third agglomeration scale and an overall powder density. The tapped density of  $\text{TiO}_2\text{-P}$  given by the supplier is  $100\text{-}180 \text{ kg/m}^3$  corresponding to the size range  $8\text{-}30 \mu\text{m}$ . Therefore, this is the size expected for nanoparticle agglomerates formed during storage.

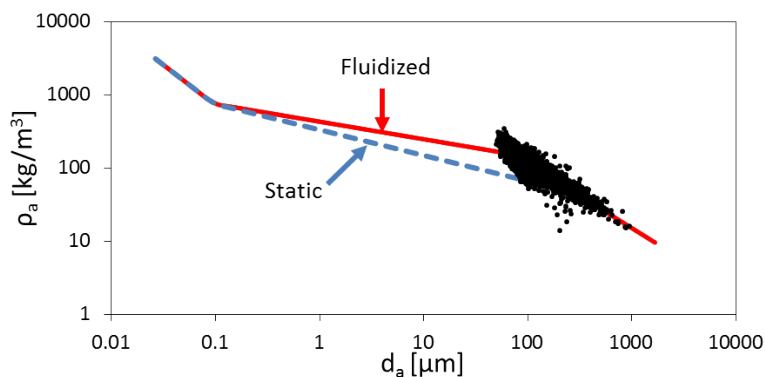


Figure 5.7: Plot of hydrophilic  $\text{TiO}_2\text{-P}$  comparing the static (dotted blue line) and fluidized (continuous red line) predicted size-to-density correlation.

## 5.5. CONCLUSIONS

In this paper, we employ *in situ* techniques to analyze the morphology of the three structural levels, namely aggregates, simple agglomerates, and complex agglomerates, for commercial metal-oxide nanopowders. The first two scales are studied by spin-echo small-angle neutron scattering (SESANS), while the third one involves a settling tube with a borescope-high-speed camera system.

The results show that the first fractal dimension for the aggregate structure is less than 2 for all the powders. The second fractal dimension lays above 2.6 with a maximum at 3, and the third one decreases back to values between 1.8 and 2.2. The data obtained from both methods was combined to understand the correlation between size and density throughout the nanopowder agglomeration size scales in a fluidized bed. Hence, the conclusions on the fractal dimension of the specific samples studied by de Martin et al. [31] are rather general to fluidization of commercial nanopowder.

It was found that fluidization affects the second scale by densifying the structure. The fractal dimension calculated from SESANS gave higher values for the fluidized samples, which according to Eq. 5.2, results in a denser structure. This outcome was supported by the experiments done with the settling tube, which required an increase on the second fractal dimension to have a continuous correlation among all three scales in the fluidized state. Therefore, it can be concluded that fluidization dynamics affect the second scale, creating denser structures that later form large complex agglomerates.

## REFERENCES

- [1] *Wide Range Aerosol Spectromete*, GRIMM.
- [2] S. V. Sokolov, E. Kästelhön, and R. G. Compton, *A thermodynamic view of agglomeration*, *The Journal of Physical Chemistry C* **119**, 25093 (2015).
- [3] W. Yao, G. Guangsheng, W. Fei, and W. Jun, *Fluidization and agglomerate structure of  $\text{SiO}_2$  nanoparticles*, *Powder Technol* **124**, 152 (2002).

- [4] J. R. van Ommen, *Manufacturing core-shell nanoparticles by atomic layer deposition in a fluidized bed*, in *International Symposium on Chemical Reaction Engineering* (2012).
- [5] A. Teleki, R. Wengeler, L. Wengeler, H. Nirschl, and S. Pratsinis, *Distinguishing between aggregates and agglomerates of flame-made TiO<sub>2</sub> by high-pressure dispersion*, *Powder Technology* **181**, 292 (2008).
- [6] M. Heggen, M. Oezaslan, L. Houben, and P. Strasser, *Formation and analysis of core-shell fine structures in Pt bimetallic nanoparticle fuel cell electrocatalysts*, *The Journal of Physical Chemistry C* **116**, 19073 (2012).
- [7] N. Biswas, R. Bhattacharya, A. Saha, N. R. Jana, and J. K. Basu, *Interplay of electrostatics and lipid packing determines the binding of charged polymer coated nanoparticles to model membranes*, *Phys. Chem. Chem. Phys.* **17**, 24238 (2015).
- [8] J. M. Valverde, M. A. S. Quintanilla, A. Castellanos, D. Lepek, J. Quevedo, R. N. Dave, and R. Pfeffer, *Fluidization of fine and ultrafine particles using nitrogen and neon as fluidizing gases*, *AIChE J* **54**, 86 (2008).
- [9] C. Zhu, Q. Yu, R. N. Dave, and R. Pfeffer, *Gas fluidization characteristics of nanoparticle agglomerates*, *AIChE Journal* **51**, 426 (2005).
- [10] E. Heikkilä, H. Martinez-Seara, A. A. Gurtovenko, M. Javanainen, H. Häkkinen, I. Vattulainen, and J. Akola, *Cationic Au nanoparticle binding with plasma membrane-like lipid bilayers: Potential mechanism for spontaneous permeation to cells revealed by atomistic simulations*, *The Journal of Physical Chemistry C* **118**, 11131 (2014).
- [11] T. S. Vaidya, *Fluidization behavior of alumina nano-particles*, *Applied Mechanics and Materials* **110-116**, 1833 (2011).
- [12] P. Hu, X. Zhang, C. Zhang, and Z. Chen, *Molecular interactions between gold nanoparticles and model cell membranes*, *Phys. Chem. Chem. Phys.* **17**, 9873 (2015).
- [13] A. Suhendi, A. B. D. Nandiyanto, T. Ogi, and K. Okuyama, *Agglomeration-free core-shell polystyrene/silica particles preparation using an electrospray method and additive-free cationic polystyrene core*, *Materials Letters* **91**, 161 (2013).
- [14] L. F. Hakim, J. L. Portman, M. D. Casper, and A. W. Weimer, *Aggregation behavior of nanoparticles in fluidized beds*, *Powder Technology* **160**, 149 (2005).
- [15] J. Jung and D. Gidaspow, *Fluidization of nano-size particles*, *Journal of Nanoparticle Research* **4**, 483 (2002).
- [16] M. Dadkhah, M. Peglow, and E. Tsotsas, *Characterization of the internal morphology of agglomerates produced in a spray fluidized bed by x-ray tomography*, *Powder Technology* **228**, 349 (2012).

- [17] J. M. Valverde, F. Pontiga, C. Soria-Hoyo, M. A. S. Quintanilla, H. Moreno, F. J. Duran, and M. J. Espin, *Improving the gas-solids contact efficiency in a fluidized bed of CO<sub>2</sub> adsorbent fine particles*, Phys. Chem. Chem. Phys. **13**, 14906 (2011).
- [18] J. A. Quevedo, A. Omosebi, and R. Pfeffer, *Fluidization enhancement of agglomerates of metal oxide nanopowders by microjets*, AIChE Journal **56**, 1456 (2010).
- [19] J. Shabaniyan, R. Jafari, and J. Chaouki, *Fluidization of ultrafine powders*, Int Rev Chem Eng **4**, 16 (2012).
- [20] F. Parveen, F. Berruti, C. Briens, and J. McMillan, *Effect of fluidized bed particle properties and agglomerate shape on the stability of agglomerates in a fluidized bed*, Powder Technology **237**, 46 (2013).
- [21] H. L. Tao Zhou, *Estimation of agglomerate size for cohesive particles during fluidization*, Powder Technology **101**, 57 (1999).
- [22] A. Khadilkar, P. L. Rozelle, and S. V. Pisupati, *Models of agglomerate growth in fluidized bed reactors: Critical review, status and applications*, Powder Technology **264**, 216 (2014).
- [23] Y. Liang, M. Ozawa, and A. Krueger, *A general procedure to functionalize agglomerating nanoparticles demonstrated on nanodiamond*, ACS Nano **3**, 2288 (2009).
- [24] S. Salameh, J. Schneider, and J. e. a. Laube, *Adhesion mechanisms of the contact interface of TiO<sub>2</sub> nanoparticles in films and aggregates*, Langmuir **28**, 11457 (2012).
- [25] J. Laube, S. Salameh, M. Kappl, L. Mädler, and L. C. Ciacchi, *Contact forces between TiO<sub>2</sub> nanoparticles governed by an interplay of adsorbed water layers and roughness*, Langmuir **31**, 11288 (2015).
- [26] M. Tahmasebpour, L. de Martín, M. Talebi, N. Mostoufi, and J. R. van Ommen, *The role of the hydrogen bond in dense nanoparticle-gas suspensions*, Phys Chem Chem Phys **15**, 5788 (2013).
- [27] M. Seipenbusch, S. Rothenbacher, M. Kirchhoff, H. J. Schmid, G. Kasper, and A. P. Weber, *Interparticle forces in silica nanoparticle agglomerates*, Journal of Nanoparticle Research **12**, 2037 (2010).
- [28] W. Yan, S. Li, Y. Zhang, Q. Yao, and S. D. Tse, *Effects of dipole moment and temperature on the interaction dynamics of titania nanoparticles during agglomeration*, The Journal of Physical Chemistry C **114**, 10755 (2010).
- [29] T. Vicsek, *Fractal Growth Phenomena*, edited by T. Vicsek (World Scientific Pub Co Inc, 1992).
- [30] S. K. Friedlander, *Smoke, Dust, and Haze: Fundamentals of Aerosol Dynamics* (Oxford University Press, 2000).
- [31] L. de Martín, W. G. Bouwman, and J. R. van Ommen, *Multidimensional nature of fluidized nanoparticle agglomerates*, Langmuir **30**, 12696 (2014).



- [32] D. Hu, J. Zhuang, and M. Ding, *A review of studies on the granular agglomeration mechanisms and anti-agglomeration methods*, Key Engineering Materials **501**, 515 (2012).
- [33] C. H. Nam, R. Pfeffer, R. N. Dave, and S. Sundaresan, *Aerated vibrofluidization of silica nanoparticles*, AIChE Journal **50**, 1776 (2004).
- [34] J. M. Valverde and A. Castellanos, *Fluidization, bubbling and jamming of nanoparticle agglomerates*, Chem Eng Sci **62**, 6947 (2007).
- [35] L. de Martin, A. Fabre, and J. R. van Ommen, *The fractal scaling of fluidized nanoparticle agglomerates*, Chemical Engineering Science **112**, 79 (2014).
- [36] S. Morooka, K. Kusakabe, A. Kobata, and Y. Kato, *Fluidization state of ultrafine powders*, Journal of Chemical Engineering of Japan **21**, 41 (1988).
- [37] X. S. Wang, V. Palero, J. Soria, and M. J. Rhodes, *Laser-based planar imaging of nanoparticle fluidization: Part i: determination of aggregate size and shape*, Chem Eng Sci **61**, 5476 (2006).
- [38] M. A. S. Quintanilla, J. M. Valverde, M. J. Espin, and A. Castellanos, *Electrofluidization of silica nanoparticle agglomerates*, Ind Eng Chem Res **51**, 531 (2012).
- [39] M. T. Rekveldt, J. Plomp, W. G. Bouwman, W. H. Kraan, S. Grigoriev, and M. Blaauw, *Spin-echo small angle neutron scattering in delft*, Review of Scientific Instruments **76** (2005).
- [40] R. Andersson, W. G. Bouwman, S. Luding, and I. M. Schepper, *Structure in cohesive powders studied with spin-echo small angle neutron scattering*, Granular Matter **10**, 407 (2008).
- [41] L. de Martin, J. Sanchez-Prieto, F. Hernandez-Jimenez, and J. van Ommen, *A settling tube to determine the terminal velocity and size distribution of fluidized nanoparticle agglomerates*, Journal of Nanoparticle Research **16**, 2183 (2013).
- [42] E. Xanthakis, J. R. van Ommen, and L. Ahrné, *Flowability characterization of nanopowders*, Powder Technology **286**, 156 (2015).
- [43] L. de Martín, W. G. Bouwman, and J. R. van Ommen, *Multidimensionality in fluidized nanopowder agglomerates*, in *Powders and Grains, AIP Conf. Proc.* (2013).
- [44] R. Andersson, W. Bouwman, J. Plomp, F. Mulder, H. Schimmel, and I. D. Schepper, *Structure, anisotropy and fractals in compressed cohesive powders*, Powder Technol **189**, 6 (2009).
- [45] G. Bushell, Y. Yan, D. Woodfield, J. Raper, and R. Amal, *On techniques for the measurement of the mass fractal dimension of aggregates*, Advances in Colloid and Interface Science **95**, 1 (2002).

## APPENDIX 5.A

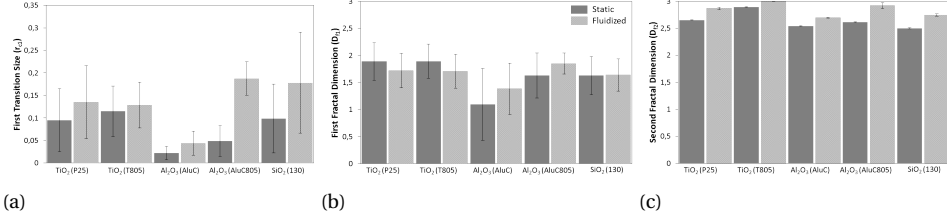


Figure 5.8: Values calculated from SESANS measurements for static (solid dark) and fluidized (light patterned) samples keeping  $r_{c1}$ ,  $D_{f1}$ , and  $D_{f2}$  as fitting parameters. The plots are the transition size between the first and second scales (a), the first fractal dimension (b), and the second fractal dimension (c).

Evaluation of the second prefactor and transition size between simple and complex agglomerates. At the intersection points, the size and density of both scales are the same. Also, in order to meet the boundary condition of a single nanoparticle,  $\hat{k}_{n1}$  must be equal to 1. To estimate the second prefactor we used:

$$\hat{k}_{n1} \left( \frac{d_{a1}}{d_p} \right)^{D_{f1}-3} = \hat{k}_{n2} \left( \frac{d_{a2}}{d_p} \right)^{D_{f2}-3} \quad (5.11)$$

$$d_{a1} = d_{a2} = r_{c1} \quad (5.12)$$

$$\hat{k}_{n1} = 1 \quad (5.13)$$

$$\hat{k}_{n2} = \left( \frac{r_{c1}}{d_p} \right)^{D_{f1}-D_{f2}} \quad (5.14)$$

For the transition size between the simple and complex agglomerates we got:

$$d_{a2} = d_{a3} \rightarrow d_{c2} \quad (5.15)$$

$$\hat{k}_{n2} \left( \frac{d_{c2}}{d_p} \right)^{D_{f2}-3} = \hat{k}_{n3} \left( \frac{d_{c2}}{d_p} \right)^{D_{f3}-3} \quad (5.16)$$

$$d_{c2} = d_p \left( \frac{\hat{k}_{n2}}{\hat{k}_{n3}} \right)^{\frac{1}{D_{f3}-D_{f2}}} \quad (5.17)$$



# 6

## MODELING THE SIZE DISTRIBUTION IN A FLUIDIZED BED OF NANOPOWDER

Fluidization is a technique used to process large quantities of nanopowder with no solvent waste and a large gas-solid contact area. Nonetheless, nanoparticles in the gas phase form clusters, called agglomerates, due to the relatively large adhesion forces. The dynamics within the fluidized bed influence the mechanism of formation, and thus, the morphology of the agglomerates. There are many theoretical models to predict the average size of fluidized agglomerates; however, these estimates of the average lack information on the whole size range. Here, we predict the agglomerate size distribution within the fluidized bed by estimating the mode and width using a force balance model. The model was tested for titania ( $\text{TiO}_2$ ), alumina ( $\text{Al}_2\text{O}_3$ ), and silica ( $\text{SiO}_2$ ) nanopowders, which were studied experimentally. An *in-situ* method was used to record the fluidized agglomerates for size analysis and model validation.

## 6.1. INTRODUCTION

A balance between adhesion and separation forces (or energies) is a settled theoretic framework to predict the average agglomerate size of fluidized nanopowders [2–9]. The average agglomerate size is usually assumed to be that at which the adhesion and separation forces balance each other; however, predictions of agglomerate size distributions are absent. It is well known that cohesive powders form agglomerates with a very wide, typically log-normal, size distribution [10–13]. The purpose of the present paper is to explore a conceptual model to predict the width of the distribution using a force balance approach.

Fluidization is a common method to process nanoparticles [12, 14–16], which fluidize as agglomerates due to the relatively strong attractive interactions, particularly van der Waals and capillary forces [14, 17–20]. As the stable structures of the fluidized powder, the properties of the agglomerates are directly linked to the fluidization dynamics [14]. Nanopowder fluidization depends on the agglomerate properties and can be classified as agglomerate particulate fluidization (APF) or agglomerate bubbling fluidization (ABF) [21]. APF is characterized by uniform, non-bubbly behavior, high solid-gas contact, and homogeneous distribution of powder throughout the bed. On the other hand, ABF shows a small bed expansion with channels, bubbles, and non-uniform powder distribution [10, 16]. The fluidization type and agglomerate properties are co-dependent. As a key property distinguishing the two forms of fluidization, various studies have focused on the theoretical and experimental estimation of the fluidized agglomerate size.

Visualization techniques for the fluidized nano and micron size scales include the *ex situ* Transmission and Scanning Electron Microscopes (TEM and SEM, respectively), and multiple camera systems for *in situ* measurements. Sample extraction and preparation of the fragile fluidized agglomerates for SEM and TEM have led to images of agglomerate sizes smaller than those expected inside the fluidized bed [22]. This indicates the need of *in situ* techniques for more accurate results [22, 23]. A common *in situ* method used to measure the fluidized agglomerate size involves laser illumination and a digital CCD camera [16]. Average agglomerate sizes between 70  $\mu\text{m}$  and 900  $\mu\text{m}$  have been measured with this technique for Aerosil R974, Aeroxide  $\text{TiO}_2$ , fumed silica, zirconia, and iron oxide nanopowders [11, 12, 14, 22–25]. Furthermore, the laser / CCD camera system was also used for size distribution measurements at the splash zone of the Aerosil R974 fluidized bed with mode at approximately 140  $\mu\text{m}$  [11] or 200  $\mu\text{m}$  [12], or a positive skewed distribution in the size range 40–600  $\mu\text{m}$  [23]. Another visualization technique, the Lasentec Focused Beam Reflectance Method / Particle Vision Measurement system, showed a log-normal size distributions of Aerosil R974 and Aerosil 90 [10, 26]. More recently, de Martin et al. [5] developed a settling tube technique for the analysis of agglomerate size distribution, among other properties, at the splash zone of the fluidized bed.

Knowledge of the fluidized agglomerate size distribution is crucial for proper understanding of the dynamic process within the fluidized bed, which are of great importance in nanopowder processing and applications such as in medicine, optics, and solar cells [27, 28]. Even though the tools to experimentally determine the agglomerate size distribution are available, most of the studies only focus on the average size values. These measured sizes are mainly used for qualitative analysis or comparison based on different fluidization conditions or powder properties, with no further description of the size dis-

tribution. This includes the limited use of force (energy) balances to estimate the mean agglomerate size only.

In this work we predict the mode and width of the log-normal fluidized agglomerate size distribution from a simple force balance. The attractive and repulsive forces were calculated theoretically to identify the dominating interactions. This model is simple, and provides a good prediction of the size distribution based on a novel interpretation of the conventional force balance concept. Simplification of the final expression obtained from the balance shows that the size distribution of fluidized nanoparticle agglomerates is self-similar. The calculated size distribution is validated by *in situ* experiments using oxide nanopowders showing either APF or ABF behavior.

## 6.2. MATERIAL AND METHODS

The nanopowders used in this study were bought from Evonik. The characteristics given by the supplier are shown in Table 6.1. All nanopowders are sieved using a 450  $\mu\text{m}$  mesh to remove large agglomerates that would prevent proper fluidization. The powders are fluidized in a 15 cm high quartz column with a square cross-section of 4.5 $\times$ 4.5 cm using pure nitrogen gas at 0.13 m/s, which enters the column through a distributor plate. The gas leaving the setup is sent to a water bubbler and HEPA filter to remove any entrained particles.

Table 6.1: Properties of the fluidized nanopowders as provided by the manufacturer.

Powder	Surface	$d_p$ (nm)	$\rho_p$ (kg/m <sup>3</sup> )	$\rho_{Tamped}$ (kg/m <sup>3</sup> )
TiO <sub>2</sub> P25	hydrophilic	21	4000	100-180
Al <sub>2</sub> O <sub>3</sub> AluC	hydrophilic	13	3800	50
SiO <sub>2</sub> A130	hydrophilic	16	2200	50

The fluidized agglomerates are recorded while falling through a settling tube placed in the splash zone. The settling tube is a black box with an opening at the top to catch falling agglomerates, and two openings on the side for agglomerate recording and tube cleaning purposes (Fig.6.1). A rigid borescope (Olympus R040-021-000-60 S5) and high speed camera (Phantom v9.1) system are used for the recordings, enabling a visible size range from 30  $\mu\text{m}$  to 4 mm [29].

The videos are taken 10 minutes after starting fluidization to reach an observable steady state. The movies are analyzed using a MATLAB script by dividing them into frames, and later processing each frame for light correction, and agglomerate recognition, tracking, filtering, and measurements. More details on the technique can be found in the papers by de Martin et al.[29, 30].

An important feature of nanoparticle agglomerates is the solid fraction, which can be estimated from their density. The agglomerate density can be calculated from the settling velocity and size obtained from the videos. The size distribution is taken directly from the images, assuming the agglomerates to be spherical [30]. The settling velocity is also directly calculated from the images since the frame rate is known, and agglomerate displacement between frames is obtained from the agglomerate recognition step. Settling velocity and agglomerate size are used to calculate the Reynolds number, which is

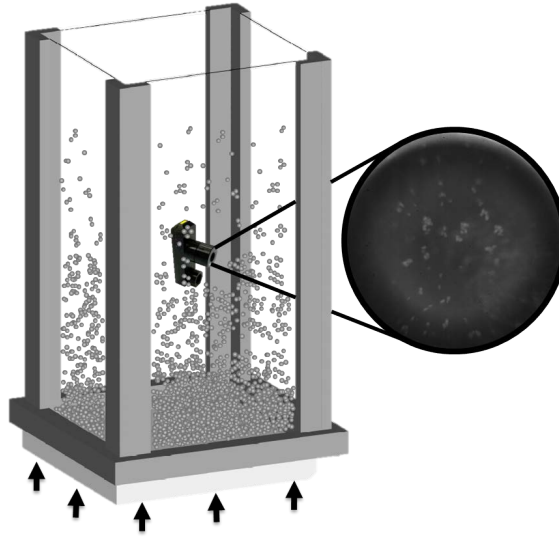


Figure 6.1: *In-situ* analysis of fluidized agglomerates. Nanopowder is fluidized in a square column with the settling tube placed at the splash zone. A sample frame from a recorded video is shown.

used to estimate the drag coefficient, thus completing the list of parameters needed to determine the agglomerate density.

### 6.3. THEORY

The forces acting on a fluidized agglomerate are divided into two categories: adhesion (those keeping ensembles of particles together) and separation (those breaking particle ensembles). The forces to be considered, and their classification into the two groups varies in literature. Van der Waals, capillary, and electrostatic are regularly in the adhesion group, while gravity-buoyancy sometimes is classified as cohesive [3, 4] and sometimes as a separation force [8]. Here, gravity-buoyancy is classified as a separation force. Bed expansion, drag, and collision forces belong to the group of separation forces. The gravity-buoyancy force is evaluated with the effective density of the agglomerate. The bed expansion force is that exerted on nanoparticles by the bubbles inside the bed, which depends on bubble size, agglomerate pressure around a spherical bubble, gravity, agglomerate size and density, and coordination number [2]. The drag force calculation includes a shape factor of 0.9 in the denominator, representing the agglomerate sphericity. Finally, capillary force is estimated as the maximum force assuming the formation of a liquid bridge between two highly porous spherical agglomerates. Figure 6.2 presents a comparison of the forces as a function of the agglomerate size, showing that the dominant forces acting on the fluidized agglomerate are van der Waals ( $F_{vdW}$ ), capillary ( $F_c$ ), and collision ( $F_{coll}$ ).

In a dry system, the main forces acting on a fluidized agglomerate are van der Waals and collision (Fig.6.3). Hence, a simple but representative force balance equating the effective forces (Eq.6.1) can give valuable approximations to the size distribution within

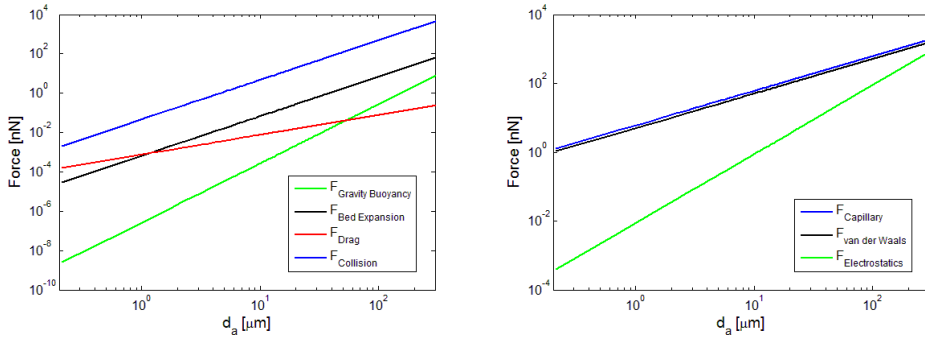


Figure 6.2: Contribution from each force to the overall force balance of agglomerates in a fluidized bed. Left plot corresponds to separation forces; right plot are the adhesion forces. Values were estimated for P25

the fluidized bed.

$$F_{vdW} = F_{coll} \tag{6.1}$$

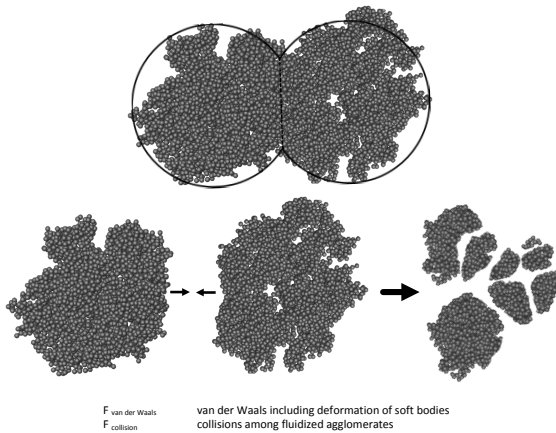


Figure 6.3: Schematic of the force balance on fluidized agglomerates. Van der Waals is the main force holding the agglomerates together, counteracted by the dominant separation force of collisions.

Comparing the forces leads to two important values, the size at which the difference between the adhesion and separation forces is maximum, and that at which it is zero (Fig.6.4). A crucial concept of this model is that agglomeration is fastest when the difference between adhesion and separation forces is largest. The agglomerate size where this occurs has the steepest slope in the log-normal size distribution (i.e. inflection point). A force difference of zero indicates that the average separation and adhesion forces have the same magnitude, so that a force unbalance leads to a probability density fall onto smaller or larger sizes. Hence, the size at zero difference is the mode, denoting a threshold on the distribution.



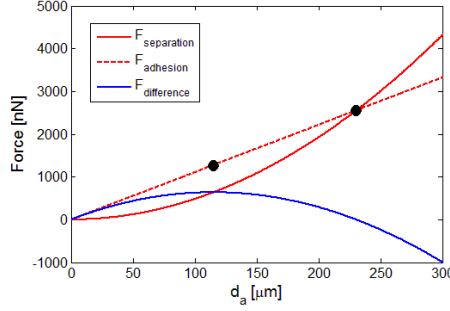


Figure 6.4: Estimation of values used to describe the size distribution inside a fluidized bed of nanopowder. The separation and adhesion forces, together with the force difference versus agglomerate size, are plotted. The circles show the two key values at maximum and zero force difference used by the model to predict the size distribution.

### 6.3.1. VAN DER WAALS FORCE

When two soft bodies are pulled together by attractive forces, there is a flattening at the location of contact [31]. Therefore, the force between two soft bodies includes the interaction between the deformed adhesive areas, and that between the volumes within the van der Waal's range. Using the assumptions of small non-elastic deformation, absence of electrostatic components, and smooth surfaces, the contact force can be expressed as [32]:

$$F_{vdW} = \frac{h_w \phi R_a}{16\pi\delta^2} \left( 1 + \frac{h_w \phi}{8\pi^2 \delta^3 H_r} \right) \quad (6.2)$$

where  $h_w$  is the Lifshitz-van der Waals constant ( $h_w = \pi H_a 4/3$ ),  $R_a$  is the agglomerate radius,  $\phi$  is the solid fraction of the agglomerate,  $\delta$  is the contact distance commonly taken as  $0.4nm$  [32], and  $H_r$  is the agglomerate Young's modulus calculated using [33]:

$$H_r = 17.1\phi^4 \left[ \frac{E_p^2 \Gamma}{d_p} \right]^{1/3} \quad (6.3)$$

which depends on the nanoparticle's Young's modulus ( $E_p$ ), work of adhesion ( $\Gamma$ ), and diameter ( $d_p$ ) [34]. The Hamaker coefficient ( $H_a$ ) [35] used to calculate  $h_w$  is an average of those considering water or vacuum as the medium, given that water molecules cannot be completely removed from the nanoparticle surface [36]. Since the Hamaker coefficient is estimated by integrating the van der Waals' attractive potential over the volume and number of molecules, for porous structures, the attraction depends on the solid fraction. Therefore, the Lifshitz-van der Waals constant is multiplied by the solid fraction ( $\phi$ ) to account for the void of the agglomerate when calculating the contribution of the interaction. This results in the final expression of the van der Waals force between two soft porous agglomerates (Eq.6.2).

### 6.3.2. COLLISION FORCE

Due to the dynamics within a fluidized bed, agglomerates are constantly colliding with each other. The collision force is derived from the theory of elasticity [37] for agglomerates colliding vertically. The collision force depends on the degree of compression, which is a function of the density ( $\rho_a$ ), Young's modulus ( $H_r$ ), Poisson's ratio ( $\nu$ ), size ( $d_a$ ), and relative collision velocity ( $V_x$ ) of the agglomerates. The following expression assumes the agglomerates to be identical spheres colliding in a fluid with viscosity  $\mu$  and density  $\rho_f$ , represented as [3, 4, 6, 8]:

$$F_{coll} = 0.166 \left( \frac{\pi V_x^6 \rho_a^3}{k^2} \right)^{1/5} d_a^2 \quad (6.4)$$

where

$$k = \frac{1 - \nu^2}{\pi H_r} \quad (6.5)$$

The estimated relative velocity of the agglomerate depends on the fluidization behavior. That for ABF powders is [8, 38]:

$$V_b = (1.5 \bar{P}_{s,n} D_b g \epsilon_b)^{0.5} \quad (6.6)$$

where  $\bar{P}_{s,n}$  is the dimensionless average particle pressure of a non-sticky system taken as 0.077 [19, 39],  $g$  is the acceleration due to gravity,  $\epsilon_b$  is the void fraction of the fluidized bed, and  $D_b$  is the bubble diameter estimated by [38]:

$$D_b = 0.652 (A_t (u_0 - u_{mf}))^{2/5} \quad (6.7)$$

from the bed cross-sectional area ( $A_t$ ), superficial gas velocity ( $u_0$ ), and minimum fluidization velocity ( $u_{mf}$ ), which can be calculated from [38, 40]:

$$u_{mf} = \frac{0.00923 d_a^{1.82} (\rho_a - \rho_f)^{0.94}}{\mu^{0.88} \rho_f^{0.06}} \quad (6.8)$$

In the case of non-bubbling fluidization (APF), the relative velocity is expected to range between  $\approx 0$  and the agglomerate settling velocity (Stokes regime) plus the superficial gas velocity. The lower limit is for two suspended agglomerates that barely come into contact in a close-to-parallel trajectory. The upper limit is for an agglomerate moving downwards at its settling velocity colliding with an upward moving agglomerate at the velocity of the fluidizing gas. Considering the relative velocity for non-bubbling fluidization to have a symmetric distribution, it comes down to:

$$V_{nb} \approx \frac{1}{2} \left[ u_0 + \frac{(\rho_a - \rho_f) d_a^2 g}{18\mu} \right] \quad (6.9)$$

### 6.3.3. SIZE DISTRIBUTION PREDICTION

To simplify the complexity of fluidized nanoparticle agglomerates, the model includes some basic assumptions. Only collision and van der Waals, the two dominating forces acting on a dry fluidized agglomerate, are considered. Agglomerates are assumed to be spherical with an homogeneous distribution of nanoparticles. The two interacting agglomerates described throughout the model are assumed to be identical. For the model, all collisions are assumed to be head-to-head at an angle of  $180^\circ$ . The assumptions that have the greatest impact on the accuracy of the model prediction are those affecting the elasticity of the agglomerates, which has a strong dependence on the agglomerate's density, or agglomerate solid fraction, as seen in Eq.6.3. From the given assumptions, the final overall force difference for our model becomes:

$$\Delta F = \frac{h_w \phi}{32\pi\delta^2} \left( 1 + \frac{h_w \phi}{8\pi^2\delta^3 H_r} \right) d_a - 0.166 \left( \frac{\pi V_x^6 \rho_a^3}{k^2} \right)^{1/5} d_a^2 \quad (6.10)$$

From Equations 6.2-6.9 it is clear that  $h_w$ ,  $\delta$ ,  $k$ ,  $H_r$ , and  $\rho_a$  are constant, and  $V_x$  hardly changes with size. Therefore, the force balance has the form:

$$\Delta F = a d_a - b d_a^n \quad (6.11)$$

where  $b$  and  $n$  depend on the fluidization behavior. Given that the 1 inside the first parenthesis of Eq.6.10 (van der Waals) was found to have minimal contribution, the second term became the coefficient  $a$ :

$$\frac{h_w^2 \phi^2}{256\pi^3 \delta^5 H_r} = a \quad (6.12)$$

In the case of bubbling fluidization (ABF), minimum fluidization velocity ( $u_{mf}$ ) depends on agglomerate size ( $d_a$ ) to the power of 1.82 (Eq.6.8). Once  $u_{mf}$  is evaluated and compared to the superficial gas velocity ( $u_0$ ), it is found to be 2 orders of magnitude smaller, and thus, neglected. The coefficient  $b$  is then evaluated from:

$$D_b \approx 0.652(A_t(u_0))^{2/5} \quad (6.13)$$

$$V_b \approx (1.5\bar{P}_{s,n} D_b g \epsilon_b)^{0.5} \quad (6.14)$$

$$0.166 \left( \frac{\pi V_b^6 \rho_a^3}{k^2} \right)^{1/5} = b \quad (6.15)$$

giving a simplified model to predict the size distribution by estimating the agglomerate size at maximum and zero force difference ( $\Delta F$ ) corresponding to the size at the inflection point ( $d_{a(MaxG)}$ ) and mode ( $d_{a(Mode)}$ ), respectively:

$$\Delta F = 0 = a d_a - b d_a^2 \quad \longrightarrow \quad d_{a(Mode)} = (a/b) \quad (6.16)$$

$$\frac{d\Delta F}{d d_a} = 0 = a - 2b d_a \quad \longrightarrow \quad d_{a(MaxG)} = (a/2b) \quad (6.17)$$

In the case of non-bubbling fluidization (APF), the velocity expression was fully substituted in the force balance equation, leading to:

$$0.166 \left( \frac{\pi \left( \frac{1}{2} \left[ u_0 + \frac{(\rho_a - \rho_f)g}{18\mu} \right] \right)^6 \rho_a^3}{k^2} \right)^{1/5} = b \quad (6.18)$$

which results in the following set of expressions:

$$\Delta F = 0 = ad_a - bd_a^{22/5} \quad \longrightarrow \quad d_{a(Mode)} = (a/b)^{5/17} \quad (6.19)$$

$$\frac{d\Delta F}{dd_a} = 0 = a - (22/5)bd_a^{17/5} \quad \longrightarrow \quad d_{a(MaxG)} = (a/b)^{5/17} (5/22)^{5/17} \quad (6.20)$$

The mode size depends on constant parameters from material properties and fluidization conditions represented by  $a$  and  $b$ . The size at the inflection point is half the mode in ABF powders, and close to 0.65 for APF systems. This characteristic holds if the average relative particle velocity in ABF is independent from agglomerate size. The self-similarity in the size distribution of fluidized agglomerates is expected since experimental data of micron size particulate systems shows the same trend [41, 42]. Furthermore, the mathematical feature of the collision kernels in the Smoluchowski differential equation for fractal-like agglomerates are such that self-similar size distributions are possible [43–45].

The  $a/b$  ratio includes the Hamaker coefficient, Young's modulus, relative particle velocity, and solid fraction. This ratio indicates that increasing the Hamaker coefficient will increase the mode size, which is expected as the adhesion force is increased. Additionally, increasing the Young's modulus, relative particle velocity, or solid fraction will decrease the mode and distribution width. This is also foreseen since harder agglomerates present less deformation during collision, creating a small area of contact, thus dissipating little energy on deformation and using most of it on breakage. Moreover, the model indicates that fluidization gas velocity has minor effect on the agglomerate size, which is experimentally observed in Quevedo et al. [26], where adding a microjet had very little impact on the fluidized agglomerate size.

## 6.4. RESULTS AND DISCUSSION

### 6.4.1. SIZE DISTRIBUTION

The size distribution of the fluidized agglomerates was experimentally determined from the images taken by the settling tube technique [29]. For all the powders, the agglomerate size varies between 76  $\mu\text{m}$  and 462  $\mu\text{m}$ , which is in good agreement with values found in literature using a high speed camera [11, 12, 14, 22, 23]. The density distribution can be calculated once the size and agglomerate settling velocity are known. The average size and density values for all powders are presented in Table 6.2.

Experimental studies of nanoparticle agglomerates from literature have reported a log-normal size distribution [10, 26, 46]. This is expected, because for granulation, which is similar to nanoparticle agglomeration [41, 44, 47, 48], the coalescence principle also

Table 6.2: Average experimental density and size of fluidized agglomerates obtained using the settling tube. Confidence intervals are one standard deviation.

Powder	$\rho_a$ ( $kg/m^3$ )	$d_a$ ( $\mu m$ )
TiO <sub>2</sub> P25	101 ± 46	142 ± 66
Al <sub>2</sub> O <sub>3</sub> AluC	55 ± 40	289 ± 173
SiO <sub>2</sub> A130	47 ± 26	265 ± 129

predicts a log-normal size distribution. Indeed, we found experimentally that a log-normal distribution best described the size distribution for all nanopowders.

#### 6.4.2. MODEL PREDICTIONS

Now, the agreement between the size distribution based on the model presented above and the experimental data is analyzed. There are two interesting aspects to consider. First, the model predicts that bubbling fluidization leads to a size distribution with a mode to inflection point ratio  $\delta$  of 0.5, whereas homogeneous fluidization gives a ratio of  $\delta = 0.65$ . The second prediction is the absolute values of agglomerate sizes. It should be noted that the model predicts these features of the agglomerate size distribution without any fitted parameters, and that it uses independently determined material properties for the different powders.

Table 6.3 shows key parameters describing the log-normal distribution for our own data and for powders from other studies. Considering first the bubbling fluidization, the average value of  $\delta$  is found to be 0.51, close to the theoretical prediction of 0.5. Similarly, the data obtained for homogeneous fluidization has  $\langle \delta \rangle = 0.58$ , comparable to the model value of 0.65. The agreement is not perfect, and there is still significant variation among the systems within each group. Nonetheless, the data strongly suggests that the type of fluidization is an important factor in determining this important characteristics of the distribution.

Table 6.3: Experimental parameters, including representative literature data:  $\mu$  and  $\sigma$  are the mean and the standard deviation of the log of the distribution, respectively, and  $\delta$  is the ratio of the mode and the inflection point for the log-normal probability density function. Values for titania (P25), alumina (AluC), and silica (A130, R974) are shown.

Powder	$\mu$	$\sigma$	$\delta$	Fluidization
TiO <sub>2</sub> P25	4.86	0.4414	0.58	ABF
Al <sub>2</sub> O <sub>3</sub> AluC	5.51	0.5531	0.48	ABF
SiO <sub>2</sub> A130	5.41	0.4584	0.56	APF
TiO <sub>2</sub> P25 [11]	4.59	0.5574	0.48	ABF
SiO <sub>2</sub> R974[11]	4.95	0.3698	0.64	APF
SiO <sub>2</sub> R974[23]	4.66	0.4858	0.54	APF

Since it has been established that the dimensionless features of the distribution agree with the model, the absolute size predictions are now evaluated. Note that this is essentially based on a single number for each powder, i.e. the ratio of  $a$  and  $b$  in Eq 6.11. Fig. 6.5 shows the experimental histograms, together with the model predictions. The

experimental values of  $\mu$ ,  $\sigma$  and  $\delta$  are presented in Table 6.3, while the model values are  $(\mu, \sigma, \delta) = (4.88, 0.387, 0.50)$  for  $\text{TiO}_2$ ,  $(5.61, 0.387, 0.51)$  for  $\text{Al}_2\text{O}_3$ , and  $(5.47, 0.312, 0.60)$  for  $\text{SiO}_2$ . Taking into consideration that there are no fitted parameters, the agreement is notably good. An important caveat, however, is the use of the experimentally determined density, of which the uncertainty propagates strongly into the uncertainty of the predicted size. The distributions obtained from the model by keeping density as a fitting parameter are included in the Appendix. Still, Fig. 6.5 is the more impressive demonstration of the importance of the model.

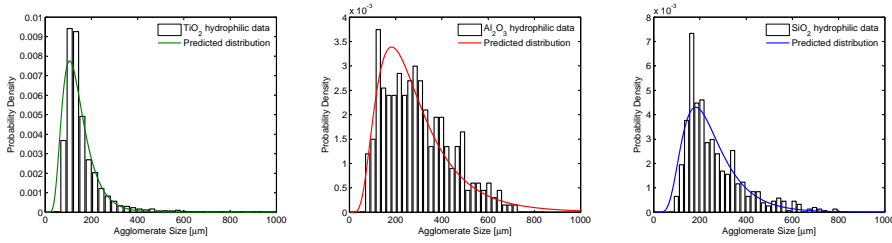


Figure 6.5: Log-normal prediction of the size distribution for titania (P25), alumina (AluC), and silica (A130). Histogram of raw data and model prediction for each material are plotted.

## 6.5. CONCLUSIONS

A simple model based on a separation versus adhesion force balance was developed to estimate the size distribution in a fluidized bed of nanopowder. The model predicts two key values from which the fluidized agglomerate log-normal size distribution can be evaluated. One value is the size at the inflection point, determined as that at which the difference between the adhesion and separation forces is maximum. And the second being the mode size, that at which separation and adhesion forces balance each other. The two sizes are related by a factor of 0.5 and 0.65, for ABF and APF, respectively. The model was validated with experiments using three commercial metal oxide nanopowders and data from literature showing both, bubbling (ABF) and uniform (APF), fluidization behaviors. The prediction of the size distribution is quite close to the experimental data. Nonetheless, further refinement is required for applicability to hydrophobic materials and inclusion of clusters smaller than  $10 \mu\text{m}$ .

## NOMENCLATURE

$a$	Force balance coefficient
$A_t$	Bed cross-sectional area [ $m^2$ ]
$b$	Force balance coefficient
$c$	Force balance exponent
$d_a$	Agglomerate size [ $m$ ]
$d_{a(MaxG)}$	Fluidized agglomerate diameter at the distribution's inflection point [ $m$ ]
$d_{a(Mode)}$	Fluidized agglomerate mode diameter [ $m$ ]
$D_b$	Bubble size [ $m$ ]

$D_f$	Agglomerate fractal dimension
$d_p$	Nanoparticle diameter [ $m$ ]
$E_p$	Nanoparticle Young's modulus [Pa]
$g$	Gravitational acceleration [ $m_s^2$ ]
$H_a$	Hamaker coefficient [ $J$ ]
$H_r$	Agglomerate Young's modulus [ $Pa$ ]
$h_w$	Lifshitz-van der Waals constant [ $J$ ]
$K$	Function of Poisson's ratio and Young's modulus
$k_n$	Agglomerate prefactor
$N_p$	Number of particles in an agglomerate
$\bar{P}_{s,n}$	Dimensionless particle pressure
$R_a$	Agglomerate radius [ $m$ ]
$R_{tip}$	Colloid radius [ $m$ ]
$s$	Indentation depth [ $m$ ]
$s_0$	Point of zero indentation [ $m$ ]
$u_{mf}$	Minimum fluidization velocity [ $m/s$ ]
$u_o$	Superficial gas velocity [ $m/s$ ]
$V_x$	Collision relative velocity [ $m/s$ ]
$F_{Hertz}$	Hertz force [ $N$ ]
$F_{vdW}$	Van der Waals force [ $N$ ]
$F_{coll}$	Collision force [ $N$ ]
$\epsilon_a$	Agglomerate void fraction
$\epsilon_b$	Fluidized bed void fraction
$\delta$	Separation at contact [ $m$ ]
$\Delta F$	Adhesion and separation force difference [ $N$ ]
$\gamma$	Water surface tension [ $N/m$ ]
$\Gamma$	Work of adhesion [ $J/m^2$ ]
$\mu$	Fluid viscosity [ $N$ ]
$\nu$	Agglomerate Poisson's ratio
$\rho_a$	Agglomerate density [ $kg/m_3$ ]
$\rho_f$	Fluid density [ $kg/m^3$ ]
$\rho_p$	Nanoparticle density [ $kg/m^3$ ]
$\rho_{Tamped}$	Nanopowder bulk density [ $kg/m^3$ ]
$\phi$	Agglomerate shape factor

## REFERENCES

- [1] *Wide Range Aerosol Spectromete*, GRIMM.
- [2] M. H. Yuki Iwadate, *Prediction of agglomerate sizes in bubbling fluidized beds of group C powders*, Powder Technology **100**, 223 (1998).
- [3] T. Zhou and H. Z. Li, *Force balance modelling for agglomerating fluidization of cohesive particles*, Powder Technology **111**, 60 (2000).

- [4] D. Turki and N. Fatah, *Behavior and fluidization of the cohesive powders: Agglomerates sizes approach*, Brazilian Journal of Chemical Engineering **25**, 697 (2008).
- [5] L. de Martin, W. G. Bouwman, and J. R. van Ommen, *Multidimensional nature of fluidized nanoparticle agglomerates*, Langmuir **30**, 12696 (2014).
- [6] H. L. Tao Zhou, *Estimation of agglomerate size for cohesive particles during fluidization*, Powder Technology **101**, 57 (1999).
- [7] M. R. Tamadondar, R. Zarghami, K. Boutou, M. Tahmasebpour, and N. Mostoufi, *Size of nanoparticle agglomerates in fluidization*, The Canadian Journal of Chemical Engineering **94**, 476 (2016).
- [8] S. Matsuda, H. Hatano, T. Muramoto, and A. Tsutsumi, *Modeling for size reduction of agglomerates in nanoparticle fluidization*, Aiche Journal **50**, 2763 (2004).
- [9] J. Chaouki, C. Chavarie, and D. Klvana, *Effect of interparticle forces on the hydrodynamic behavior of fluidized aerogels*, Powder Technology **43**, 117 (1985).
- [10] J. A. Quevedo, A. Omosebi, and R. Pfeffer, *Fluidization enhancement of agglomerates of metal oxide nanopowders by microjets*, AIChE Journal **56**, 1456 (2010).
- [11] J. M. Valverde, M. A. S. Quintanilla, A. Castellanos, D. Lepek, J. Quevedo, R. N. Dave, and R. Pfeffer, *Fluidization of fine and ultrafine particles using nitrogen and neon as fluidizing gases*, AIChE J **54**, 86 (2008).
- [12] C. Zhu, Q. Yu, R. N. Dave, and R. Pfeffer, *Gas fluidization characteristics of nanoparticle agglomerates*, AIChE Journal **51**, 426 (2005).
- [13] S. V. Sokolov, E. Kästelhön, and R. G. Compton, *A thermodynamic view of agglomeration*, The Journal of Physical Chemistry C **119**, 25093 (2015).
- [14] L. F. Hakim, J. L. Portman, M. D. Casper, and A. W. Weimer, *Aggregation behavior of nanoparticles in fluidized beds*, Powder Technology **160**, 149 (2005).
- [15] A. Goulas and J. Ruud van Ommen, *Atomic layer deposition of platinum clusters on titania nanoparticles at atmospheric pressure*, J. Mater. Chem. A **1**, 4647 (2013).
- [16] J. R. van Ommen, J. M. Valverde, and R. Pfeffer, *Fluidization of nanopowders: a review*, J Nanopart Res **14**, 737 (2012).
- [17] J. Israelachvili, *Intermolecular and surface forces* (Academic Press, 1991).
- [18] J. R. van Ommen, *Manufacturing core-shell nanoparticles by atomic layer deposition in a fluidized bed*, in *International Symposium on Chemical Reaction Engineering* (2012).
- [19] J. Shabanian, R. Jafari, and J. Chaouki, *Fluidization of ultrafine powders*, Int Rev Chem Eng **4**, 16 (2012).



- [20] M. J. Espin, J. M. Valverde, M. A. S. Quintanilla, and A. Castellanos, *Electromechanics of fluidized beds of nanoparticles*, Physical Review E **79** (2009).
- [21] W. Yao, G. Guangsheng, W. Fei, and W. Jun, *Fluidization and agglomerate structure of SiO<sub>2</sub> nanoparticles*, Powder Technol **124**, 152 (2002).
- [22] C. H. Nam, R. Pfeffer, R. N. Dave, and S. Sundaresan, *Aerated vibrofluidization of silica nanoparticles*, AIChE Journal **50**, 1776 (2004).
- [23] X. S. Wang, V. Palero, J. Soria, and M. J. Rhodes, *Laser-based planar imaging of nanoparticle fluidization: Part I: determination of aggregate size and shape*, Chem Eng Sci **61**, 5476 (2006).
- [24] H. Liu, L. Zhang, T. Chen, S. Wang, Z. Han, and S. Wu, *Experimental study on the fluidization behaviors of the superfine particles*, Chemical Engineering Journal **262**, 579 (2015).
- [25] X. S. Wang, F. Rahman, and M. J. Rhodes, *Nanoparticle fluidization and geldart's classification*, Chemical Engineering Science **62**, 3455 (2007).
- [26] J. A. Quevedo and R. Pfeffer, *In situ measurements of gas fluidized nanoagglomerates*, Industrial and Engineering Chemistry Research **49**, 5263 (2010).
- [27] J. M. Zook, V. Rastogi, R. I. MacCuspie, A. M. Keene, and J. Fagan, *Measuring agglomerate size distribution and dependence of localized surface plasmon resonance absorbance on gold nanoparticle agglomerate size using analytical ultracentrifugation*, ACS Nano **5**, 8070 (2011).
- [28] N. Mandzy, E. Grulke, and T. Druffel, *Breakage of TiO<sub>2</sub> agglomerates in electrostatically stabilized aqueous dispersions*, Powder Technology **160**, 121 (2005).
- [29] L. de Martin, J. Sanchez-Prieto, F. Hernandez-Jimenez, and J. van Ommen, *A settling tube to determine the terminal velocity and size distribution of fluidized nanoparticle agglomerates*, Journal of Nanoparticle Research **16**, 2183 (2013).
- [30] L. de Martin, A. Fabre, and J. R. van Ommen, *The fractal scaling of fluidized nanoparticle agglomerates*, Chemical Engineering Science **112**, 79 (2014).
- [31] B. Dahneke, *The influence of flattening on the adhesion of particles*, Journal of Colloid and Interface Science **40**, 1 (1972).
- [32] H. Krupp, *Particle adhesion theory and experiment*, Advances in Colloid and Interface Science **1**, 111 (1967).
- [33] K. Kendall, N. M. Alford, and J. D. Birchall, *Elasticity of particle assemblies as a measure of the surface energy of solids*, Proceedings of the Royal Society of London A: Mathematical, Physical and Engineering Sciences **412**, 269 (1987).
- [34] A. Fabre, S. Salameh, L. C. Ciacchi, M. T. Kreutzer, and J. R. van Ommen, *Contact mechanics of highly porous oxide nanoparticle agglomerates*, Journal of Nanoparticle Research **18**, 1 (2016).

- [35] H. J. Butt and M. Kappl, *Surface and Interfacial Forces* (Wiley, 2010).
- [36] S. Salameh, J. Schneider, and J. e. a. Laube, *Adhesion mechanisms of the contact interface of TiO<sub>2</sub> nanoparticles in films and aggregates*, *Langmuir* **28**, 11457 (2012).
- [37] J. G. S.P. Timoshenko, *Theory of Elasticity* (McGraw-Hill, 1970).
- [38] Q. Guo, X. Yang, W. Shen, and H. Liu, *Agglomerate size in an acoustic fluidized bed with sound assistance*, *Chemical Engineering and Processing: Process Intensification* **46**, 307 (2007).
- [39] M. Horio and Y. Iwodate, *The prediction of sizes of agglomerates formed in fluidized beds*, *Proceedings of the 5th World Congress of Chemical Engineering, 2nd Intl. Particle Technology Forum* **V**, 571 (1996).
- [40] M. Leva, *Fluidization* (McGraw-Hill, New York, 1959).
- [41] K. V. Sastry, *Similarity size distribution of agglomerates during their growth by coalescence in granulation or green pelletization*, *International Journal of Mineral Processing* **2**, 187 (1975).
- [42] H. Hatzantonis, A. Goulas, and C. Kiparissides, *A comprehensive model for the prediction of particle-size distribution in catalyzed olefin polymerization fluidized-bed reactors*, *Chemical Engineering Science* **53**, 3251 (1998).
- [43] D. Khang and H. H. Lee, *Particle size distribution in fluidized beds for catalytic polymerization*, *Chemical Engineering Science* **52**, 421 (1997).
- [44] S. K. Friedlander, *Smoke, Dust, and Haze: Fundamentals of Aerosol Dynamics* (Oxford University Press, 2000).
- [45] S. Vemury and S. E. Pratsinis, *Self-preserving size distributions of agglomerates*, *Journal of Aerosol Science* **26**, 175 (1995).
- [46] E. Limpert, W. A. Stahel, and M. Abbt, *Log-normal distributions across the sciences: Keys and clues*, *BioScience* **51**, 341 (2001).
- [47] L. Liu, *Kinetic theory of aggregation in granular flow*, *AIChE J* **57**, 3331 (2011).
- [48] L. Liu, *Effects of aggregation on the kinetic properties of particles in fluidised bed granulation*, *Powder Technology* **271**, 278 (2015).

## APPENDIX 6.A

### LOGNORMAL DISTRIBUTION FROM PREDICTED VALUES

A log-normal distribution profile was found to be the best standardized fit for all the nanopowders. The relevant equations are shown in this section. The so called "Inflection Point" value corresponds to the size at which adhesion and separation forces have the largest difference. Thus, this is expected to be the size where growth rate is maximum ( $\frac{d^2 \text{LogNormalPDF}}{dx^2}$ ). The "Mode" agglomerate size calculated by the model is that at which separation and adhesion forces balance each other. The set of equations is:

$$\text{LogNormalPDF} = \frac{1}{x\sigma\sqrt{2\pi}} e^{-\frac{(\ln x - \mu)^2}{2\sigma^2}} \quad \text{Mode} = e^{\mu - \sigma^2} \quad (6.21)$$

$$\text{MaxGrowthRate} = e^{\frac{1}{4}(\pm\sqrt{4\sigma^4 + 16\sigma^2} - 6\sigma^2 + 4\mu)} \quad \text{Variance} = (e^{\sigma^2} - 1)e^{2\mu - \sigma^2} \quad (6.22)$$

$$\text{Mean} = e^{\mu + \frac{\sigma^2}{2}} \quad \text{Median} = e^{\mu} \quad (6.23)$$

### MODEL PREDICTION WITH DENSITY FIT

Density is kept as a fitting parameter to model the size distribution of the data (Fig.6.6). Even though the difference on the fitted and experimental density values is small, the prediction is noticeably better for the fitted case due to the strong dependence of the model on the density.

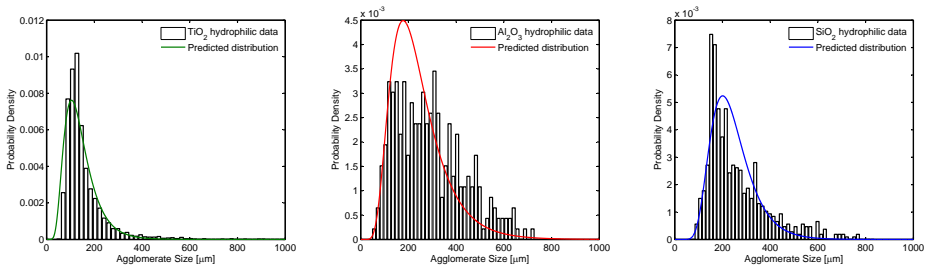


Figure 6.6: Log-normal prediction of the size distribution for titania (P25), alumina (AluC), and silica (A130). Histogram of raw data and model prediction for each material, with density as a fitting parameter.

The fitted values fall within the range of the experimental density within one standard deviation (Fig.6.7). The fitted density is slightly higher than the experimental mean for all the powders. Hence, a precise method to measure the density of the fluidized agglomerates is required to adjust the model, and further improve its prediction accuracy.

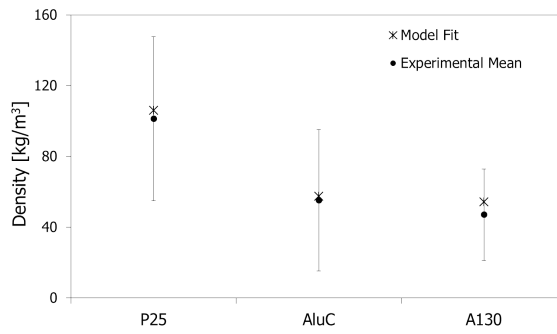


Figure 6.7: Fitted agglomerate density (stars) compared to the density distribution obtained from experimental data (solid dots).



# 7

## CONCLUSIONS AND OUTLOOK

### 7.1. CONCLUSIONS

This thesis presents new insights on nanoparticle fluidization by analyzing the agglomeration process, agglomerate properties, and fluidization dynamics. The materials used in this study are the commercial metal oxide nanopowders titania ( $\text{TiO}_2$ ), alumina ( $\text{Al}_2\text{O}_3$ ), and silica ( $\text{SiO}_2$ ) in their hydrophobic and hydrophilic versions. Since nanoparticles are widely used in industry, consumer products, and medical treatments, it is crucial to fully understand their properties and behavior, which include their interactions and dynamics during processing.

Nanoparticles tend to agglomerate in the gas-phase due to their relatively strong attractive interactions. The agglomeration process has three main steps starting during production (forming aggregates from nanoparticles), followed by storage (forming simple agglomerates from aggregates), and finalizing with fluidization (forming complex agglomerates from simple agglomerates). Nanoparticle agglomerates are known to be very fragile, with porosity above 95%, making them extremely challenging to study, thus forcing the development of subtle *in situ* techniques such as aerosol spectrometry techniques, SESANS, and the settling tube described in this thesis.

Morphological properties of the nanoparticle clusters were studied experimentally. These clusters are described by their mass fractal dimension. Aggregates were found to withstand the effect of fluidization showing a fractal dimension around  $1.5 \pm 0.5$  at all times. On the other hand, simple agglomerates were densified by fluidization, with overall fractal dimensions of 2.6-3. Finally, complex agglomerates which form in the fluidized bed, showed a fractal dimension between 1.8 and 2.2. Even though complex agglomerates are extremely porous, they have a mass dominance in the fluidized bed (Chapter 4); hence, these fragile structures were further analyzed. Their elasticity described by the Young's modulus was measured by AFM. It was found that  $\text{Al}_2\text{O}_3$ ,  $\text{SiO}_2$ , and  $\text{TiO}_2$  nanoparticle agglomerates have an elasticity comparable to that of cells, soft gels, or light foams with Young's moduli in the 10-200 kPa range.

Even though nanoparticles agglomerate in the gas phase, a large amount of nanostructures is still present during nanopowder fluidization, presenting potential hazards in

case of leakage (Chapter 4). Therefore, nanoparticle fluidization can be worrisome since the long-term toxicity of such nanostructures is not known, thus making predictions of fundamental agglomeration features exceedingly valuable. The elasticity found with the AFM was estimated theoretically using a model from literature developed by Kendall et al. [1] resulting in values in the same order of magnitude. Also, a model based on a separation versus adhesion force balance was developed to predict the size distribution in a fluidized bed of nanopowder. The main forces acting on the fluidized agglomerates were found to be collision and van der Waals. The agglomerate size distribution can be predicted by comparing the two forces in the agglomerate size range from 10  $\mu\text{m}$  to 1 mm. Two key values, those at maximum and zero force difference, are the parameters used for the prediction. The model was found to be remarkably good at predicting the size distribution of fluidized hydrophilic  $\text{Al}_2\text{O}_3$ ,  $\text{SiO}_2$ , and  $\text{TiO}_2$ , and data from literature for different  $\text{SiO}_2$  and  $\text{TiO}_2$  powders.

## 7.2. OPPORTUNITIES FOR FUTURE RESEARCH

As this research advanced the field of nanoparticle fluidization, it also raised some questions and thus, opportunities for further research. The fragility of fluidized agglomerates makes them highly susceptible to alteration due to external forces. Powder manipulation is expected to have a significant impact on agglomerate morphology, mainly processes meant to change the composition of the primary particles such as coating. Additionally, the outstanding fragility makes the agglomerates extremely challenging to be studied in detail without altering the original structure. In Chapter 6, it was shown that the effect of collision on the agglomerate size distribution is pivotal. Furthermore, collision outcome depends on the properties of the agglomerates such as the force holding them together, which is related to the number of contacts and force at the contact, and the plasticity of the fluidized agglomerates. Therefore, an in-depth characterization of nanoparticle agglomerates and thorough study on collision dynamics is important to elucidate even more the agglomerate dynamics and formation inside the fluidized bed, as explained in the following sections.

### 7.2.1. AGGLOMERATE PLASTICITY

Some of the curves obtained from Atomic Force Microscopy (AFM) (Chapter 3) showed non-elastic behavior of the nanoparticle agglomerates (Fig.7.1, plot). Further analysis with AFM and the combined technique of AFM and an electron microscope (TEM or SEM) would help understand the nature of the agglomerate's plasticity. Statistics on AFM measurements are extremely important due to the heterogeneity of the agglomerates, requiring more than 200 curves per sample for proper analysis.

Each detectable peak of the force curve corresponds to a specific modification of the agglomerate morphology (Fig.7.1). The height of the peak gives the force required for the rearrangement, disconnection, or rotation of the particles, providing information for precise simulation of nanoparticle agglomerates, their morphology, and interactions. For example, the energy threshold for agglomerate breakup during collisions could be estimated, considering the energy required for deformation as estimated from AFM force curves. From the shown curve (Fig.7.1), about 1  $\mu\text{m}$  of indentation is needed

to achieve the 150 nN compression force; assuming a chain of nanoparticles, the length corresponds to 50 NP particles. Since the plot shows the approach part (compression), one can expect NP rearrangement going from a straight chain into a flat layer. A very rough estimate gives 3 nN per particle-particle rearrangement. However, knowing that there are multiple branched chains involving more than 50 NP in the compressed volume, gives a smaller force, which agrees with the estimated particle-particle contact force of 2.5 nN measured by Salameh et al.[2].

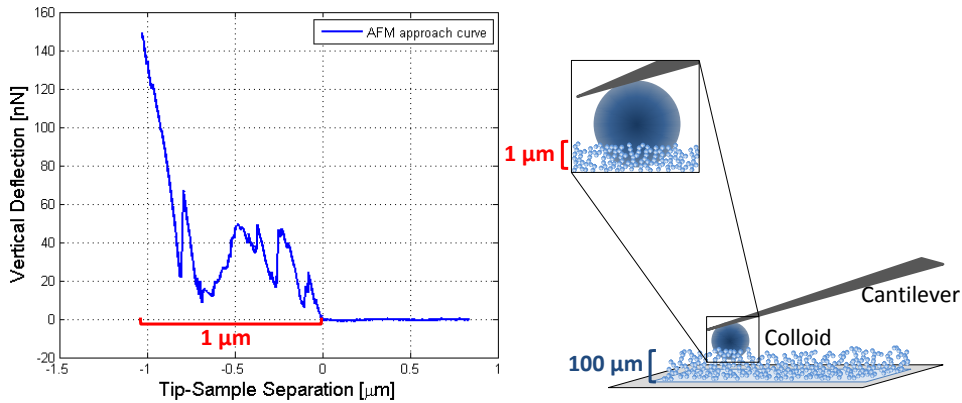


Figure 7.1: Schematic of AFM cantilever with a  $3.5 \mu\text{m}$  glass colloid pressing on an agglomerate sample. On the left is the force curve obtained from the sketched system showing peaks representing particle rearrangement. The measured indentation to attain the preset 150 nN is  $1 \mu\text{m}$ , corresponding to a chain of 50 nanoparticles, and approximately 1% of the agglomerate sample thickness.

The plasticity study was not carried out since the initial objective of the AFM measurements was to measure the Young's modulus of the agglomerate to compare the hard and soft sphere assumptions, and to choose among the different expressions available to describe agglomerate interactions based on their elasticity. Given that a majority of the curves showed the Hertz elastic behavior, these were used for the original objective, leaving the non-elastic curves aside for future analysis.

### 7.2.2. ADJUSTED FORCE BALANCE MODEL

The force balance model discussed in Chapter 6 uses van der Waals and collision as the dominating forces, with average values as parameters for the prediction of the size distribution inside the fluidized bed. The model is extremely dependent on density, which is assumed to be constant for all agglomerate sizes. However, Chapter 5 shows that this is not the case; the density of the fractal nanoparticle agglomerates depends on the size raised to the power of the fractal dimension. Implementing this relation will widen the model's range of relevance to other scales and powders. This was not done since the equations used for the van der Waals and collision forces already assume the agglomerates to be spherical with an homogeneous distribution of nanoparticles, and the fractal density concept did not fit in the model. Also, to make the model applicable



to hydrophobic powders, more research should be done on the nanoparticle properties. Given the complexity of the study and time limitation of the PhD, this could not be added to the current work.

Some of the assumptions taken during the development of the model should be verified experimentally and adjusted to cover a wider range of powders. For example, once the plasticity of the nanoparticle agglomerates is known from AFM measurements, the model should be modified to include the findings. Additionally, the equation used for the collision force should be validated with collision experiments of nanoparticle agglomerates.

### 7.2.3. COLLISION DYNAMICS

Preliminary analysis and experiments were done to study the collision dynamics between two fluidized agglomerates. The steps to achieve the final one-to-one agglomerate collision start with proper fluidization of the nanopowder in two identical beds. Then, a stream of fluidized nanoparticle agglomerates from each column is ejected, with the shooting channels facing each other. These channels are designed to focus the agglomerates to the middle with a micrometer precision to ensure collision. Additionally, the sample stream coming from each column should be synchronized so that there is enough distance between the flowing agglomerates for a clear visualization of each collision pair, but not too much as to ensure frequent collisions with minimum agglomerate waste. Finally, the collision should be at the focus plane of the recording system, which includes a borescope and high-speed camera, with enough resolution for video analysis and particle recognition of a few microns (Fig. 7.2).

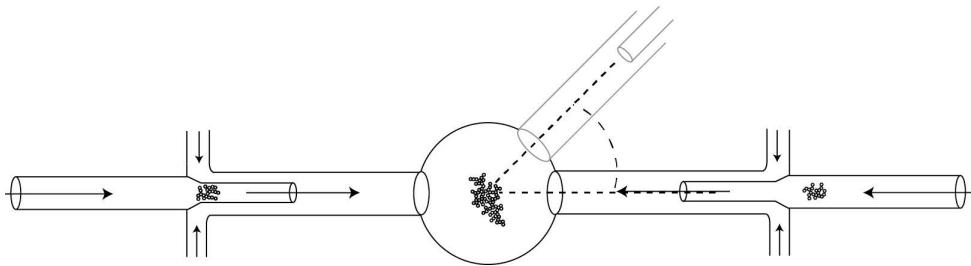


Figure 7.2: General schematic of the experimental design for studying collision dynamics. Two focusing channels with a sampled agglomerate coming from the fluidized bed are placed at opposite ends of the collision chamber, defined by a circle. The fluidized bed and attached channel can be moved around for study of collision angle as shown in the figure.

Preliminary results showed the effect of the focusing-to-focused streams flow ratio on the focusing efficiency, the data conversion from micron-sized particles to nanoparticles agglomerates, and the feasibility of agglomerate location at the focus plane [3]. For the current setup with a 3 mm shooting tube and 20 cm/s sample flow, a 300  $\mu\text{m}$  agglomerate with 50  $\text{kg}/\text{m}^3$  density has a Stokes number of 0.936, for which the agglomerate behavior in the gas flow is not straightforward.

Multiple modifications are required to achieve the main analysis goal. Currently, the setup requires the creation of a dilute cloud from static powder since direct ejection of

the fluidized powder results in an extremely dense sample-stream. Hence, the setup should be adjusted to extract dilute samples directly from the fluidized bed, and to synchronize two identical shooting jets for one-on-one collision at the focus plane. One way would be to have the ejection channel high on the column wall and with a small amount of nanopowder being fluidized. The risk would be the lack of complex agglomerates in the sample stream. In that case, more powder should be loaded, with a branched ejection port to decrease the amount of sampled structures. Also, the sample flow acquired from a bed with gas at minimum fluidization velocity creates an extremely high shooting flow, which is not representative of the agglomerate relative velocity inside the fluidized bed. The branching of the ejection channel might solve this problem too. Agglomerate synchronization is a more complex issue since sampling is random. Nonetheless, it is more critical to have enough distance between the shooting agglomerates in a focusing channel to prevent accumulated collisions, even if that decreases the probability of having one-to-one collisions often. This is because agglomerate supply is abundant.

#### 7.2.4. NUMBER OF CONTACTS BETWEEN AGGLOMERATES

To better understand the collision phenomena and stress/stain measurements, it is important to know the contact characteristics between the agglomerates. Agglomerates are quite complex, and the arrangement of individual nanoparticles is hard to define. For example, the number of contact points between two agglomerates can be calculated by making a 3D reproduction of the structure by TEM tomography. 3D tomography has been used for 3D reconstruction of nanofiller networks [4], soot particles [5], nanoparticles [6], and catalysts [7] among other systems, becoming a key tool for structural studies of micron and nano-size objects. The number of nanoparticles connecting two agglomerates can be obtained from 3D reconstructions sliced into 2D images that show the nanoparticles at each plane. The plane with the least number of nanoparticles will be defined as the plane of agglomerate-agglomerate contact, where the number of nanoparticles corresponds to the number of contact points holding the agglomerates together.

For this, only a few tomographies were made, showing insufficient resolution of the 3D reconstruction with indistinguishable individual nanoparticles. Due to this and time limitations, the study was set aside. In addition to the 3D tomography, force curves obtained from the AFM showing multiple peaks on the approach and retraction parts provide valuable information about nanoparticle rearrangement during compression and pulling of the structure. The number and height of the peaks can be correlated to the 2D images generated from the 3D reconstructions to understand the morphology of these agglomerates. A good quantitative approximation of the number of contacts between agglomerates would improve the accuracy of the force balance model discussed in Chapter 6, for the size distribution prediction inside the fluidized bed. Knowledge about the number of contact will create a strong link with the community working on primary particle-particle contact forces.

#### 7.2.5. DIFFERENT PRODUCTION METHODS

Mass production of nanopowder is limited by the method used. As a result, flame production is commonly employed. The high temperatures lead to sintering of the nanopar-

ticles, creating strong chain-like structures, called aggregates, that impede manipulation of individual nanoparticles; thus, the smaller structures attainable from these powders are the hard aggregates as seen in Chapter 5.

As explained in this work, nanoparticles arrange into highly porous, fragile agglomerates in a step-wise fashion. Powders coming from different production methods might have different starting points; chain-like aggregates, spherical nanoparticles, or irregularly-shaped nanostructures that might form clusters with different morphologies. In order to assess the effect of production method and/or starting building-block on the agglomeration process, the research presented in this thesis should be performed for powders from various production techniques.

### 7.2.6. PROCESSED NANOPARTICLES

As explained before, powder manipulation is expected to affect the agglomerate morphology. Processes that change the composition, shape, or size of the primary particles such as coating, most likely have a significant effect on nanoparticle agglomeration and dynamics. For example, Atomic Layer Deposition (ALD) is a technique used to coat nanoparticles in a fluidized bed [8–11] for multiple purposes, of which the effect on agglomeration is not well known. Hence, repeating the studies on the formation and dynamics of fluidized nanoparticle agglomerates coated by ALD will be of great interest for academic and industrial applications requiring NP coating.

## REFERENCES

- [1] K. Kendall, N. M. Alford, and J. D. Birchall, *Elasticity of particle assemblies as a measure of the surface energy of solids*, Proceedings of the Royal Society of London A: Mathematical, Physical and Engineering Sciences **412**, 269 (1987).
- [2] S. Salameh, J. Schneider, and J. e. a. Laube, *Adhesion mechanisms of the contact interface of TiO<sub>2</sub> nanoparticles in films and aggregates*, Langmuir **28**, 11457 (2012).
- [3] R. Arends, *Collision Behaviour of Nanoparticle Agglomerate*, Master's thesis, Delft University of Technology (2015).
- [4] S. Kohjiya, A. Katoh, T. Suda, J. Shimanuki, and Y. Ikeda, *Visualisation of carbon black networks in rubbery matrix by skeletonisation of 3D-TEM image*, Polymer **47**, 3298 (2006).
- [5] M. U. S. Y. Jun Adachi, Ken Kurosaki, *Porosity influence on the mechanical properties of polycrystalline zirconium nitride ceramics*, Journal of Nuclear Materials **358**, 106 (2006).
- [6] X. Xu, Z. Saghi, R. Gay, and G. Mobus, *Reconstruction of 3D morphology of polyhedral nanoparticles*, Nanotechnology **18**, 225501 (2007).
- [7] M. Weyland, *Electron tomography of catalysts*, Topics in Catalysis **21**, 175 (2002).
- [8] S. M. George, *Atomic layer deposition: An overview*, Chemical Reviews **110**, 111 (2009).

- [9] A. Goulas and J. Ruud van Ommen, *Atomic layer deposition of platinum clusters on titania nanoparticles at atmospheric pressure*, *J. Mater. Chem. A* **1**, 4647 (2013).
- [10] D. M. King, X. Liang, C. S. Carney, L. F. Hakim, P. Li, and A. W. Weimer, *Atomic Layer Deposition of UV-Absorbing ZnO films on SiO<sub>2</sub> and TiO<sub>2</sub> nanoparticles using a fluidized bed reactor*, *Advanced Functional Materials* **18**, 607 (2008).
- [11] D. Valdesueiro, P. Garcia-Trinanes, G. Meesters, M. Kreutzer, J. Gargiuli, T. Leadbeater, D. Parker, J. Seville, and J. van Ommen, *Enhancing the activation of silicon carbide tracer particles for (PEPT) applications using gas-phase deposition of alumina at room temperature and atmospheric pressure*, *Nuclear Instruments and Methods in Physics Research Section A: Accelerators, Spectrometers, Detectors and Associated Equipment* **807**, 108 (2016).



# ACKNOWLEDGEMENTS

This thesis is the outcome of four years of work, which includes MSc classes, independent and collaborative research, teaching assistance given, meetings, and discussions in the Product and Process Engineering group from the Chemical Engineering Department in the faculty of Applied Science at Delft University of Technology.

The work was financially supported by the European Research Council, without which this thesis could not have been accomplished. The grant was awarded to J. Ruud van Ommen, who provided me with guidance and valuable discussions throughout the four years, for which I am very thankful. Similarly, I would like to thank Michiel T. Kreutzer for the constructive discussions and pertinent feedback during the PhD journey. I would like to thank all the people who attended the Journal Club and Group Meetings, which helped me develop my critical thinking and keep my research going in the most efficient way. People who were part of it include Volkert van Steijn, Pouyan Boukany, Peter Hamersma, Henk Nugteren, Mahsa Motegh, Duong Hoang, Nasim Hooshyar, Lilian de Martin Monton, Yogesh Harshe, Venkatesan Dhanasekaran, Barbara Kampa, Michiel Musterd, Rajat Bhardwaj, Piotr Glazer, Alberto Clemente, Jesus Gomez Hernandez, Javier Sanchez Prieto, Mikel Leturia, Juho Yliniemi, Hao Bui, Samir Salameh, David Valdesueiro Gonzalez, Wenjie Jin, Floris van Kempen, Hrushikesh Pimpalgaonkar, Durgesh Kawale, Dayinta Perrier, Fabio Grillo, Maulik Shah, Shaurya Sachdev, Lea Rems, Jing Guo, Liang-Jun Yin, Melvin ten Kate, Kartik Totlani, Josette Moret, and Dominik Benz. Also, I want to thank Elly Hilkhuijsen and Caroline Monna for keeping things organized in the group, and introducing me to the delicious bakkers makronen (kokos) and roomboter gevulde koeken we used to get for the group meetings; and Els Arkesteijn, Astrid Barrow, Marian de Bruijn, and Karin Wilhelm for scheduling the progress meetings and making the work environment run smoothly.

For the practical side of this research, I would like to thank Mojgan Talebi, Stefan ten Hagen, Wim van Oordt, and the ChemE workshop for helping build the setups needed to perform the experiments. Also, special thanks to Wendel de Haan, Fabian Pille, Rick Arends, Roel Kooijman, and Teun Steur for choosing a thesis topic related to mine, and giving me the opportunity to guide them throughout their projects. To the younger students, Peter Triep, Huub Rombouts, Stijn Reichert, and Michiel Hickey, together with whom I learned about sound-assisted fluidization using national anthems. Since multiple techniques were used during this four years, I would like to thank Marcel Bus and Duco Bosma for the AFM and SEM trainings, and support they provided me. Also, I want to thank George Biskos, Andreas Schmidt-Ott, and Klaas Besseling for external discussions that helped me shape the PhD project. Internal and external collaborations became crucial at strengthening the research described in the thesis; for that, I would like to thank Samir Salameh, Alberto Clemente, Wim G. Bouwman, Lucio Colombi Ciacchi, Francisco Balas, and Jesus Santamaria who are coauthors in at least one of the presented chapters.

Of course, there was an essential social component in these past four years that encouraged me to keep going every time things seemed to fall apart. Even though Delft gave me a really rough start (middle and end), I could not have finished the PhD without those fun times surrounded by wonderful people. It was motivating to have a great group of friends for paint ball, ice karting, normal karting, bowling, laser tag, BBQs, pizza nights, numerous kings games, Efteling, road trip (+ robbery), board games, Oreo milkshake nights, movie nights, beach evenings, King's/Queen's days, etc. To be more specific, David (alias Gummy Beer), thank you so much for improving my open mindedness in topics I was quite unfamiliar with; for organizing many dinners and game nights at your place; for joining me for beers after rough days at work; and for participating in most of the activities I organized. Fabio (alias Sugar Plum), thank you for all the amazing meals, trips, experiences, conversations, books, movies, etc. you shared with me; they truly changed my perspective and motivated me to look beyond what surrounds me. Samir (alias Mr. Cinderella), thanks for all the support and discussions on the material in this thesis, and for bringing sparkles, rainbows, and unicorns to the group. Aris (alias Honey Bee), thank you for showing me that the word "friendship" is highly ambiguous, and for the not-really-but-kind-of affection we almost had at the beginning. Lilian (alias Terroncito), thank you for the support and guidance when I was new here, and for warning me about your nigh-walking whenever we had to share a room. Jesús, thank you for listening to all my gloomy stories, for not getting scared by the negative aura that seems to chase me (only in The Netherlands), and for all the fun moments we shared; thank you for encouraging me to move forward in many ways, and for sticking around when things got complicated. Yogesh, Durgesh, Wenjie, Dayinta, Dominik, Julien, Jauffrey, and Floris, thank you for joining the social activities, for organizing your own, and for making my time in Delft enjoyable. Last but not least, thank you Ruijun Deng for all the shopping days, girls' nights, bubble teas, dinners, quick chats, etc.; you are a nice neighbor.

Most importantly, not just for the time of the PhD, but for my whole life, I want to thank my family for all the support, advice, time, energy, and effort they have devoted to me. A ti mami, te agradezco la dedicación, los consejos, el tiempo, el esfuerzo, el cariño, el trabajo, etc. que me haz entregado; gracias por alegrarme cada momento y siempre hacerme sentir que pase lo que pase, puedo contar contigo. De corazón te digo que todo lo que he logrado es gracias a tí. Dad, thank you for believing in me, and being such a committed personal teacher. Alejandra, Maria, and Lupita, thank you for being such amazing sources of motivation, for encouraging me to do what fulfills me, and for being a great support when things get harsh; I must say you all are the best sisters ever. To Leonardo Antonio, thank you for always being next to me and listening to my daily adventures; I knew I could relieve my frustrations by talking to you, and for that, you also deserve an apology.

# LIST OF PUBLICATIONS

## RELATED TO PHD THESIS

1. L. DE MARTIN, A. FABRE, J. R. VAN OMMEN, The fractal scaling of fluidized nanoparticle agglomerates, *Chemical Engineering Science* **112**, 79-86 (2014).
2. A. FABRE, S. SALAMEH, L. COLOMBI CIACCHI, M. T. KREUTZER, J. R. VAN OMMEN, Contact mechanics of highly porous oxide nanoparticle agglomerates, *Journal of Nanoparticle Research* **18**, 1-13 (2016).
3. A. FABRE, A. CLEMENTE, F. BALAS, M. P. LOBERA, J. SANTAMARIA, M. T. KREUTZER, J. R. VAN OMMEN, Entrainment of nanosized clusters from a nanopowder fluidized bed, *Environmental Science: Nano*, (under review) (2016).
4. A. FABRE, T. STEUR, W. G. BOUWMAN, M. T. KREUTZER, J. R. VAN OMMEN, Characterization of the stratified morphology of nanoparticle agglomerates, *Journal of Physical Chemistry C*, (2016).
5. A. FABRE, S. SALAMEH, M. T. KREUTZER, J. R. VAN OMMEN, Size distribution prediction of fluidized nanoparticle agglomerates, *Journal (under review)* (2016).

## OTHER PUBLICATIONS

6. Z. QIN, A. FABRE, M. J. BUEHLER, Structure and mechanism of maximum stability of isolated alpha-helical protein domains at a critical length scale, *The European Physical Journal E*, **36**, 53. (2013)
7. L.-J. YIN, W.-W. JI, S.-Y. LIU, W.-D. HE, L. ZHAO, X. XU, A. FABRE, B. DIERRE, M.-H. LEE, J. R. VAN OMMEN, H. T. HINTZEN, Intriguing luminescence properties of  $(\text{Ba}, \text{Sr})_3\text{Si}_6\text{O}_9\text{N}_4:\text{Eu}^{2+}$  phosphors via modifying synthesis method and cation substitution, *Journal of Alloys and Compounds*, **682**, 481-488. (2016)





# CURRICULUM VITAE

## **Andrea FABRE**

Andrea Fabre was born in January 1990 in Aguascalientes, Mexico. She finished high school in three years graduating Salutatorian in 2008 receiving the excellence award every year. In 2012 she earned a Bachelor's degree from the Massachusetts Institute of Technology in Biological and Chemical Engineering with minor in Political Science. Throughout her studies, Andrea was president, vice-president, student research chair, networking chair, resident associate advisor, and officer in more than seven organizations such as the Society of Women Engineers, Brain Trust, and Amnesty International. Her professional experience includes an internship at Gillette (Procter & Gamble) and research positions at the MA General Hospital Richard B. Simches Research center, Institut Quimic de Sarria, White laboratory (MIT), BCS/McGovern Institute for Brain Research (MIT), Laboratory of atomistic and molecular mechanics (MIT), and the Laboratory for theoretical soft materials (MIT). In August 2012, she joined the Product and Process Engineering group from the department of Chemical Engineering at the Delft University of Technology to pursue a Ph.D. on the formation, properties, and dynamics of fluidized nanoparticle agglomerates. This thesis is the outcome of four years of research, helping her earn the Ph.D. degree.



## Propositions

accompanying the thesis

### Fluidized Nanoparticles Agglomerates Formation, Characterization, and Dynamics

Andrea Fabre

1. Companies sell nanopowder composed of aggregates (>100nm) of sintered nanoparticles. Hence, the product cannot be classified as “nanopowder”.
2. Simple agglomerates densify during fluidization. The densification of simple agglomerates only happens at the center.  
*Chapter 5 of this thesis*
3. Due to the densified core, the shell of protruding NP chains at the agglomerate’s surface dictates the degree of exchange, rearrangement, and deformation of the structures during collisions in the fluidized bed.  
*Chapters 4 and 5 of this thesis*
4. The simplified equation for the van der Waals’ force [ $F_{va} = (A/12\delta^2) (d_{a1}d_{a2}/(d_{a1} + d_{a2}))$ ] is not applicable to NP agglomerates with their known properties of heterogeneous particle distribution and fractal structure. The assumptions taken for the development of the equation do not cover these features.  
*Zhou et al. (2000) Powder Tech. 111*  
*Seville et al. (2000) Powder Tech. 113*
5. Modelling nanoparticle interactions is useless since experiments cannot discriminate among theoretical interactions at the nanoscale.
6. “Agglomerates less than 133  $\mu\text{m}$  do not exist” is a false statement. Unless the statement: “Atoms, molecules, and cells did not exist until the microscope was invented” is assumed to be true.  
*Liu et al. (2015) Chem. Eng. J. 262*
7. Scientists are humans and thus, cannot be trusted.
8. It will take at least 60 years to understand the effect of human-made NPs in humans. Hence, humans should not be exposed until the long-term effect is known.
9. Given the current atmospheric conditions and pharmaceutical state of the art, it is healthier to stay away from the sun.
10. The 20cm increase in the last 200 years on the average height in the Netherlands is because of the large milk consumption.

*The propositions are considered opposable and defensible, and as such have been approved by the promoters, prof. dr. ir. M. T. Kreutzer and prof. dr. ir. J. R. van Ommen.*

## Propositions

accompanying the thesis

### Fluidized Nanoparticles Agglomerates Formation, Characterization, and Dynamics

Andrea Fabre

1. Bedrijven verkopen nanopoeier bestaande uit aggregaten (>100 nm) van gesinterde nanodeeltjes. Dus, het product kan niet geclassificeerd worden als een “nanopoeier”.
2. Eenvoudige agglomeraten verdichten tijdens de fluïdisatie. De verdichting van eenvoudige agglomeraten vindt alleen plaats in het centrum.  
*Hoofdstuk 5 van dit proefschrift*
3. Als gevolg van de verdichte kern, bepaalt de schil van uit-stekende ketens van nanodeeltjes aan het oppervlak van het agglomeraat de mate van uitwisseling, herschikking en vervorming van de structuren tijdens botsingen in het gefluïdiseerde bed.  
*Hoofdstukken 4 en 5 van dit proefschrift*
4. De vereenvoudigde vergelijking voor de vanderwaalskracht  $[F_{va} = (A/12\delta^2)(d_{a1}d_{a2}/(d_{a1} + d_{a2}))]$  is niet toepasbaar op agglomeraten van nanodeeltjes met hun bekende eigenschappen van heterogene deeltjesverdeling en fractale structuur. De aannames die gedaan zijn bij de totstandkoming van de vergelijking omvatten deze kenmerken niet.  
*Zhou et al. (2000) Powder Tech. 111*  
*Seville et al. (2000) Powder Tech. 113*
5. Het modelleren van interacties van nanodeeltjes is zinloos, omdat experimenten de theoretische interacties op de nanoschaal niet kunnen onderscheiden.
6. De stelling “Agglomeraten kleiner dan 133  $\mu\text{m}$  bestaan niet” is onjuist, tenzij men aanneemt dat de stelling “Atomen, moleculen en cellen bestonden niet tot aan de uitvinding van de microscoop” waar is.  
*Liu et al. (2015) Chem. Eng. J. 262*
7. Wetenschappers zijn mensen en dus kunnen zij niet vertrouwd worden.
8. Het zal op zijn minst 60 jaar duren om te begrijpen welk effect de door de mens gemaakte nanodeeltjes hebben op mensen. Daarom zouden mensen er niet aan blootgesteld moeten worden voordat het langetermijneffect bekend is.
9. Gegeven de huidige atmosferische condities en de huidige kennis op het gebied van farmaceutica, is het gezonder om weg te blijven uit de zon.
10. De toename van de gemiddelde lengte in Nederland met 20 cm in de afgelopen 200 jaar is het gevolg van de grote melkconsumptie.

*Deze stellingen worden oponeerbaar en verdedigbaar geacht, en zijn als zodanig goedgekeurd door de promotoren, prof. dr. ir. M. T. Kreutzer en prof. dr. ir. J. R. van Ommen.*